

WL-TR-93-4034

FATIGUE RESISTANT Ti_3Al COMPOSITES

AD-A270 305



D.B MARSHALL, M.C. SHAW, M.R. JAMES,
J. GRAVES, W.L. MORRIS, AND J.R. PORTER

ROCKWELL INTERNATIONAL
SCIENCE CENTER
1049 CAMINO DOS RIOS
THOUSAND OAKS, CA 91360

JAN 1993

FINAL REPORT FOR 09/28/90-09/27/92

APPROVED FOR PUBLIC RELEASE; DISTRIBUTION IS UNLIMITED.

DTIC
ELECTE
OCT 06 1993
S E D

MATERIALS DIRECTORATE
WRIGHT LABORATORY
AIR FORCE MATERIAL COMMAND
WRIGHT PATTERSON AFB, OH 45433-7734

93-23190



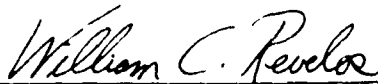
93 10 4 017

NOTICE

When Government drawings, specifications, or other data are used for any purpose other than in connection with a definitely Government-related procurement, the United States Government incurs no responsibility or any obligation whatsoever. The fact that the government may have formulated or in any way supplied the said drawings, specifications, or other data, is not to be regarded by implication, or otherwise in any manner construed, as licensing the holder, or any other person or corporation; or as conveying any rights or permission to manufacture, use, or sell any patented invention that may in any way be related thereto.

This report is releasable to the National Technical Information Service (NTIS). At NTIS, it will be available to the general public, including foreign nations.

This technical report has been reviewed and is approved for publication.



WILLIAM C. REVELO
Project Engineer
Materials Behavior Branch
Metals and Ceramics Division



KATHERINE A. WILLIAMS
Technical Area Manager
Materials Behavior Branch
Metals and Ceramics Division



NORMAN M. TALLAN
Chief
Metals and Ceramics Division

If your address has changed, if you wish to be removed from our mailing list, or if the addressee is no longer employed by your organization please notify WL/MLLN, WPAFB, OH 45433-7817 to help us maintain a current mailing list.

Copies of this report should not be returned unless return is required by security considerations, contractual obligations, or notice on a specific document.

REPORT DOCUMENTATION PAGE			Form Approved OMB No. 0704-0188	
Public reporting burden for this collection of information is estimated to average 1 hour per response, including the time for reviewing instructions, searching existing data sources, gathering and maintaining the data needed, and completing and reviewing the collection of information. Send comments regarding this burden estimate or any other aspect of this collection of information, including suggestions for reducing this burden, to Washington Headquarters Services, Directorate for Information Operations and Reports, 1215 Jefferson Davis Highway, Suite 1204, Arlington, VA. 22202-4302, and to the Office of Management and Budget, Paperwork Reduction Project (0704-0188), Washington, DC 20503				
1. AGENCY USE ONLY (Leave Blank)	2. REPORT DATE JAN 1993	3. REPORT TYPE AND DATES COVERED FINAL 09/28/90-09/27/92		
4. TITLE AND SUBTITLE FATIGUE RESISTANT Ti ₃ Al COMPOSITES		5. FUNDING NUMBERS C F33615-90-C-5928 PE 61102 PR 2306 TA P2 WU 02		
4. AUTHOR(S) D.B. MARSHALL, M.C. SHAW, M.R. JAMES, J. GRAVES, W.L. MORRIS, AND J.R. PORTER				
7. PERFORMING ORGANIZATION NAME(S) AND ADDRESS(ES) ROCKWELL INTERNATIONAL SCIENCE CENTER 1049 CAMINO DOS RIOS THOUSAND OAKS, CA 91360		7. PERFORMING ORGANIZATION REPORT NUMBER SC71034.FRD		
9. SPONSORING / MONITORING AGENCY NAME(S) AND ADDRESS(ES) MATERIALS DIRECTORATE WRIGHT LABORATORY AIR FORCE MATERIEL COMMAND WRIGHT PATTERSON AFB, OH 45433-7734		9. SPONSORING / MONITORING AGENCY REPORT NUMBER WL-TR-93-4034		
11. SUPPLEMENTARY NOTES				
12a. DISTRIBUTING/AVAILABILITY STATEMENT APPROVED FOR PUBLIC RELEASE; DISTRIBUTION IS UNLIMITED.		12b. DISTRIBUTION CODE		
13. ABSTRACT (Maximum 200 Words) Measurements of interfacial properties and residual stresses in Ti ₃ Al/SiC composites with and without ductile Ag/Ta layers are presented as the first step in determining the role of the ductile layers in the fatigue of these composites. In the composite without ductile layers, debonding and fiber sliding occurred along the interface between the outer surface of the fiber and the layer of reaction products. In the composite with Ag/Ta layers, debonding and sliding occurred within the SCS-6 layers that form the outer part of the fiber, with a higher frictional stress resisting sliding (100 MPa c.f. 66 MPa). Fatigue crack growth measurements indicated only minor differences in growth rates in the two composites in a given environment, but both composites exhibited much larger growth rates in air than in vacuum. High resolution crack opening displacement measurements are used to assess relative bridging effects. To avoid the limitation imposed by the presence of weak SCS-6 layers on the SiC fibers, a composite composed of sapphire fibers in matrix of Ti ₃ Al with an interfacial layer of Ta was fabricated. In situ observations during transverse loading indicated that the interfacial bonding was sufficiently strong that interfacial debonding or plasticity did not affect transverse properties.				
14. SUBJECT TERMS Titanium Aluminide Composites Interface Properties Transverse Failure			15. NUMBER OF PAGES 72	
			16. PRICE CODE	
17. SECURITY CLASSIFICATION OF REPORT UNCLASSIFIED	18. SECURITY CLASSIFICATION OF THIS PAGE UNCLASSIFIED	19. SECURITY CLASSIFICATION OF ABSTRACT UNCLASSIFIED	20. LIMITATION OF ABSTRACT UL	

CONTENTS

	Page
Figures.....	iv
1.0 SUMMARY OF PROGRAM AND RESULTS.....	1
2.0 INTRODUCTION	3
3.0 THE INFLUENCE OF Ag/Ta LAYERS ON RESIDUAL STRESSES AND INTERFACIAL PROPERTIES OF Ti₃Al/SCS-6 COMPOSITES.....	6
3.1 Materials	6
3.2 Residual Stresses	6
3.3 Interfacial Properties.....	7
3.4 Discussion	14
4.0 FATIGUE CRACK GROWTH IN Ti₃Al/SCS-6 COMPOSITES WITH AND WITHOUT Ag/Ta INTERFACIAL LAYERS.....	16
4.1 Experiments	16
4.2 Results	16
4.3 Discussion and Conclusions.....	23
5.0 INTERFACIAL PROPERTIES OF A SAPPHIRE/Ta/Ti₃Al COMPOSITE.....	25
5.1 Materials Fabrication	25
5.2 Microstructure.....	25
5.3 Transverse Property Measurements and Damage Observation	28
5.4 Discussion and Conclusion.....	31
6.0 REFERENCES	35
APPENDIX A MEASUREMENT OF INTERFACIAL DEBONDING AND SLIDING RESISTANCE IN FIBER REINFORCED INTERMETALLICS.....	37
APPENDIX B ANALYSIS OF FIBER DEBONDING AND SLIDING EXPERIMENTS IN BRITTLE MATRIX COMPOSITES	51

FIGURES

Figure	Page
1 Optical micrographs showing crack initiation during transverse loading: (a) super- α_2 /SCS-6 composite with Ag/Ta layers between fibers and matrix; (b) Ti-24-11 matrix with Ag/Ta layers; and (c) super- α_2 matrix without Ag/Ta layers.....	4
2 Force and displacement measurements from fiber pulling experiments on super- α_2 /SiC composite with Ag/Ta interfacial layers: (a) embedded length of fiber 660 μm , (b) initial loading data from (a) with expanded displacement scale, (c) embedded length of fiber 1.4 mm.....	8,9
3 Scanning electron micrographs of specimen used for data of Figures 2(a) and (b) after fiber was pulled entirely out of matrix. Very bright regions on fibers are remnants of the Ag/Ta layers not removed by etching	10
4 Comparisons of data from initial loading regions of Figures 2(b) and (c) with micromechanical models based on Coulomb friction and perfectly smooth fibers ("constant μ ") and a constant frictional stress ("constant τ "), using following parameters: elastic constant $A = 1.158$ calculated according to equations in Section 6 with elastic properties in Table 1, residual stress parameter $S_{R0} = 2$ for (a) and (b), $S_{R0} = 3.66$ for (c) and (d), calculated from equations of Section 6 with the measured residual axial stresses in fibers; and friction coefficients or frictional stresses listed in Table 2, obtained by best fit to the initial loading data.....	11,12
5 Average frictional stress during fiber pullout	14
6 Comparison of crack growth under cyclic loading in super- α_2 /SCS-6 composites with and without Ag/Ta layers between matrix and fibers.....	17
7 Scanning electron micrographs showing fatigue cracks at maximum and minimum (zero) load.....	18,19
8 Crack opening displacements at maximum load (u_{max}), minimum (zero) load (u_{min}) and the difference ($u_{\text{cyc}} = u_{\text{max}} - u_{\text{min}}$), for fatigue cracks of approximately the same length in both composites. (a) and (b) air environment; (c) and (d) vacuum environment. N is the number of load cycles applied to the crack.....	20,21
9 Comparison of cyclic crack opening displacements for cracks of approximately the same length in both composites, in air and vacuum.....	22
10 (a) Comparison of crack opening displacements (cyclic) near the tip of a fatigue crack at various stages of growth in air in the composite with Ag/Ta interfacial layers. (b) Variation of crack growth rate with crack opening	22,23
11 Optical micrograph of cross section of sapphire/Ta/super- α_2 composite. Reflected light with polarizer and analyzer at 89°	26

FIGURES

Figure		Page
12	Optical micrograph showing broken (bright) and intact (dark) fibers in sapphire/Ta/super- α_2 tensile test specimen of 2 mm thickness. Reflected light with polarizer and analyzer set at 89°	26
13	Scanning electron micrographs showing sapphire fiber in super- α_2 matrix. Bright line surrounding fiber is Ta coating. Bright regions of matrix are β phase; dark regions are α_2 phase.....	27
14	Scanning electron micrograph showing region of fiber-matrix interface in which Ta layer was missing.....	27
15	Stress-strain curve for transverse loading of sapphire/Ta/super- α_2 composite. The labels a, b and c indicate the loads at which the in situ micrographs of Figure 16(a,c) were obtained.....	28
16	Sequence of in situ optical micrographs taken from one area at loads of (a) 0.9, (b) 0.95, (c) 0.99 of the failure load, corresponding to the positions labeled (a) (b) and (c) in Figure 15. Failure occurred by linking of the cracks in (c). Applied load horizontal.....	29
17	Scanning electron micrograph showing crack path across the fiber-matrix interfacial region.....	30
18	Scanning electron micrograph showing fracture surface resulting from transverse tensile loading of sapphire/Ta/super- α_2 composite. Smooth region is axial split within the sapphire fiber; rough region is the super- α_2 matrix.....	31
19	Schematic diagram showing damage mechanisms observed in transverse loading.....	32
20	(a) Elastic stresses at interface of strongly bonded isolated fiber subject to transverse loading (ratio of elastic moduli of fiber and matrix = 5). (b) Stresses in matrix adjacent to fiber in (a)	33

Accession For	
NTIS	<input checked="" type="checkbox"/> CRA&I
DTIC	<input type="checkbox"/> TAB
Unannounced	<input type="checkbox"/>
Justification	
By	
Distribution /	
Availability Codes	
Dist	Avail and / or Special
A-1	

Foreword

This report describes research funded under U.S. Air Force Contract F33615-90-C-5928 and monitored by Capt. W.C. Revelos of the Materials Behavior Branch at Wright Patterson AFB, whose support and guidance are gratefully acknowledged. The authors also acknowledge the technical assistance from E.H. Wright and L.M. Holmes of Rockwell Science Center and the contribution of Dr. R. Everett from the Naval Research Laboratories who collaborated on fiber coating.

1.0 SUMMARY OF PROGRAM AND RESULTS

The goal of this research was to identify and optimize the characteristics of the fiber/matrix interface that inhibit fatigue crack initiation and growth in Ti_3Al matrix composites. Our approach was to modify the interfacial region by including layers of ductile material, and to determine the role of the ductile layers in changing interfacial properties and fatigue response. The ductile layers are expected to have several important effects. One is to prevent the formation of brittle reaction products, which provide initiation sites for fatigue cracks in the regions near the interface. Another is to modify interfacial debonding and sliding characteristics that control the bridging of long fatigue cracks. Included in this modification is fatigue of the interface itself, leading to changes in the bridging forces during cyclic loading.

The study involved correlation of observations and measurements of fatigue crack initiation and growth with rather detailed measurements of *local* mechanical properties of the fiber-matrix interface and residual stresses. These measurements were obtained using several unique techniques that we developed recently. Our initial work focussed on the measurement of interfacial properties and residual stresses in Ti_3Al composites with and without ductile Ag/Ta layers between the fibers and matrix and assessment of the fatigue crack growth characteristics of these two composites. The interfacial property and residual stress measurements are given in Section 3 and the fatigue experiments are summarized in Section 4. Appendix A contains a detailed description of the single fiber pulling technique used for measurement of interfacial properties, as well as results from direct measurements of degradation of interfacial sliding resistance during cyclic loading of fibers in the Ti_3Al composite without ductile layers. The initial development of the fiber pulling technique and the monotonic loading experiments described in Appendix A were done under other funding. The micromechanics analysis that is needed to extract interfacial properties from the fiber pulling experiments is described in Appendix B. This analysis was also initiated under other funding but was extended as part of this program, to allow analysis of the results of Sections 3 and 4 (specifically the sections dealing with the onset of complete sliding, relations between single and multiple fiber sliding and comparisons of constant friction and Coulomb friction models).

The measurements indicated that the Ag/Ta layers had no effect on residual stresses in the composite, as expected, but that the degree of bonding between the fibers and matrix was increased. However, because the SCS-6 fibers contained weak carbon layers within their outer coatings, the increase in fiber-matrix bonding had very little influence on longitudinal properties of the composite. The increased bonding simply caused the location of debonding to change from the outer surface of the fibers to the weak subsurface layers. (In the composite without Ag/Ta, debonding occurred between the outer surface of the fiber and the reaction products in the matrix. The reaction products were absent in the composite within Ag/Ta layers.) The frictional sliding resistance was higher by about 50 percent at these subsurface layers, but this did not have a significant influence on fatigue crack growth.

A much larger influence of the Ag/Ta layers in these composites was observed in a concurrent research program, which addresses transverse properties of composites. In the composite without Ag/Ta layers, the reaction product layer (approximately 1- μm thickness, consisting of carbides and silicides of the matrix elements) provided initiation sites for transverse matrix cracks, which joined with the interfacial debonds that had already formed and led to premature failure. In the composite with Ag/Ta layers, this reaction product layer was eliminated and large increases in transverse strength and failure strain were observed (a factor of 2 increase in strength and a factor of 3 increase in failure strain). Interfacial debonding occurred in this composite, but transverse matrix cracks did not form prior to failure. The debonding occurred at the subsurface carbon layer within the fibers rather than at the outer surface of the fibers, consistent with the longitudinal measurements described above. Therefore, the improved transverse properties resulted from elimination at the crack initiation sites associated with the reaction layers.

These results clearly indicate that the response of the Ag/Ta containing composite is limited by the weak carbon layers within the coatings of the SCS-6 fibers and that no further improvement in properties of the composite (either longitudinal or transverse) would be expected from further increases in strength of the interface between the matrix and outer surface of the fiber, or from changes in ductility of the interfacial layers. Further property improvements would require fibers without the weak subsurface layers. Therefore, we decided to fabricate a composite containing sapphire fibers, the same Ti_3Al (super- α_2) matrix, and an interfacial layer of Ta. The layer of Ag was not needed to protect the fibers in this case.

Fabrication of the $\text{Ti}_3\text{Al}/\text{Ta}/\text{sapphire}$ composite was done in collaboration with Dr. R. Everett at Naval Research Laboratories (NRL). The sapphire fibers were coated with Ta by physical vapor deposition (PVD) at NRL and were consolidated with matrix foils at Rockwell. Assessment of the role of the interface was done in transverse loading rather than in longitudinal loading, because of the relatively larger effect observed above. The results are given in Section 5. These tests showed that the Ta-sapphire bond was sufficiently strong to prevent debonding, either directly under the influence of the transverse load or when the interface was intersected by a crack. In fact, the transverse strengths of the test specimens were limited by transverse fracture of the fibers; cracks initiated in the fibers (crack plane normal to applied stress and parallel to fiber axes) and grew stably into the matrix at increasing load without causing any interfacial debonding. The actual strengths of the test specimens were most likely determined by damage introduced into the fibers during specimen preparation; much higher transverse strengths would seem possible in this composite system.

2.0 INTRODUCTION

The aim of the initial part of this program was to obtain detailed measurements of local mechanical properties of fiber matrix interfaces that were modified by the presence of layers of ductile material, and to determine the influence of these ductile layers on fatigue crack growth in the composite. Before beginning the detailed interfacial studies, several composites were evaluated to assess their suitability for the study. The composites were sectioned for microstructural evaluation and elemental mapping [using energy dispersive spectroscopy (EDS)], and mechanical testing in transverse tension (with in situ observation) to assess the roles of ductile and brittle interfacial layers on fracture. The transverse tension tests were done as part of another program funded by AFOSR.* Two of the composites were composed of super- α_2 (Ti-25Al-10Nb-3V-1Mo) matrices (atomic %) and SCS-6 SiC fibers, one with, and the other without layers of Ag and Ta between the fibers and the matrix. Both were fabricated by Textron: the composite without Ag/Ta layers was obtained from Rocketdyne and was used in several previous studies,¹⁻³ whereas the composite containing Ag/Ta layers, which had been deposited by PVD on the fibers before consolidation, was supplied by North American Aircraft. A similar composite from NAA containing a Ti-24Al-11Nb (at.%) matrix with PVD Ag/Ta layers was also evaluated, along with a composite fabricated at Rockwell Science Center under this program, using super- α_2 foil matrix, Ag/Ta foil interface layers and SCS-6 fibers.

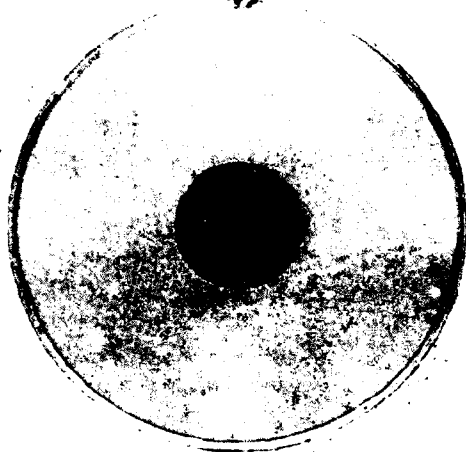
The highest transverse strengths were exhibited by the composite with the super- α_2 matrix- and PVD-coated fibers: extensive plasticity accompanied fracture and no obvious crack initiation sites were observed around the fibers prior to failure (Figure 1(a)). The microstructure was uniform, with Ag/Ta layers about 1- μ m thickness and no reaction layers observed around the fibers. On the other hand, the Ti-24Al-11Nb matrix composite with Ag-Ta layers also contained a layer ~ 5- to 10- μ m thickness of titanium carbide thought to be the result of contamination of the surfaces of the α_2 foils during fabrication of the composite (the layer also extended between the fibers within each row). The transverse strength of this composite was much lower because of these layers; failure initiated from extensive transverse microcracking that formed in the brittle layers well before the ultimate failure (Figure 1(b)). These microcracks would also be expected to be a source of fatigue cracks.

Initially a difficulty was encountered in the fabrication of the Ag/Ta foil composite, which had not been previously attempted using super- α_2 matrix foils (previous fabrication used powdered matrix). During processing, the Ta foil ruptured along lines between the fibers allowing the Ag to escape. Much of the Ag collected near the surface of the composite, forming a Ag-Ta or Ag-Ti intermetallic which led to early failure in transverse loading. There was also reaction with the fibers at these rupture locations. These initial tests again pointed to the detrimental role of brittle reaction products in providing crack initiation sites for premature failure in transverse loading. The problem was overcome by modifying the temperature-pressure cycle during fabrication and specimens were prepared for testing.

The super- α_2 composite without Ag/Ta layers had a layer of reaction products of ~ 1- μ m thickness (carbides and silicides of the matrix elements) between the fibers and matrix. Microcracking occurred in the regions around the fibers prior to failure (Figure 1(c)). The occurrence of cracking was dependent on the spacing of neighboring fibers and, as expected, was most frequent at small spacings. Interestingly, the most common microcrack orientation was *parallel* to the applied tension. A simple elastic analysis of the stresses around an isolated fiber indicates that this is indeed the location of maximum circumferential tensile stress at the fiber-matrix interface in a composite with elastic properties corresponding to SiC/Ti₃Al and in which

* AFOSR Contract No. AFOSR 90-0235, subcontract to Arizona State University.

(a)



(b)



(c)

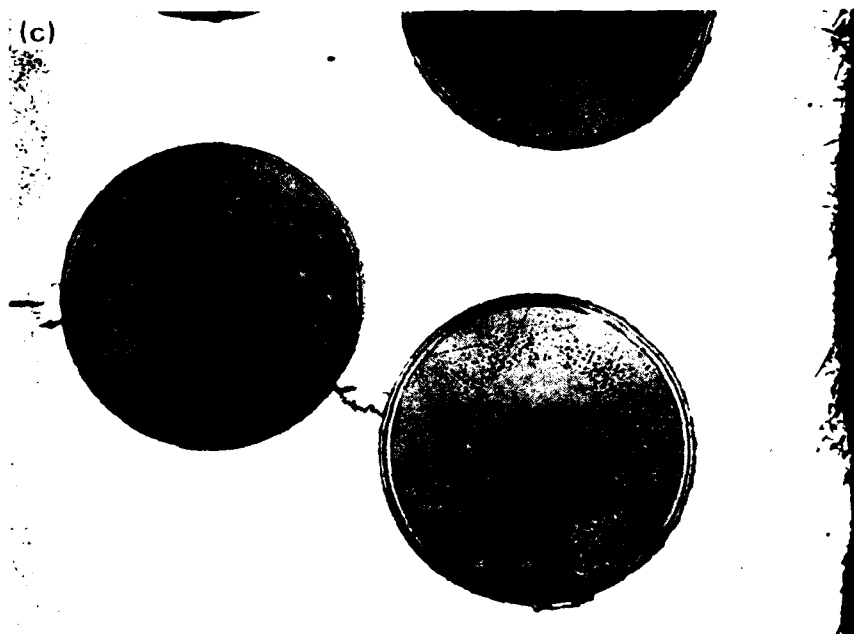


Figure 1 Optical micrographs showing crack initiation during transverse loading: (a) super- α_2 /SCS-6 composite with Ag/Ta layers between fibers and matrix; (b) Ti-24-11 matrix with Ag/Ta layers; and (c) super- α_2 matrix without Ag/Ta layers.

circumferential sliding does not occur. The same conclusion is obtained from an elastic analysis that accounts for overlapping stress fields of neighboring fibers. However, the variation in the circumferential stress around the fiber is not large, and the location of cracking may in general be dominated by other factors such as the onset of ductility in the matrix, the presence of microstructural variations in the regions surrounding the fibers (e.g., β -depleted regions, foil contamination), and the onset of interfacial debonding and circumferential sliding. The occurrence of debonding and circumferential sliding would tend to promote transverse cracking (i.e., enhance the circumferential tension at the location 90° to the applied load direction) whereas the fiber layup would tend to promote cracking parallel to the applied load (fiber spacings were generally smaller within the rows of fibers than between them).

The two super- α_2 matrix composites were thus chosen for more detailed initial study. Since the only nominal difference between these two composites is the presence of the Ag/Ta layers in one, the distinct difference in microcracking behavior can be correlated directly with the influence of the layers.

The results of measurements of interfacial properties, residual stresses and fatigue crack growth rates in these two composites were given in Sections 3 and 4 and Appendices A and B. The results indicated that the properties of the Ag-Ta containing composite were limited by the weak subsurface carbon layers of the SCS-6 fibers and that no further improvement in properties of the composite would be expected from further increases in strength of the interface between the matrix and the outer surface of the fiber. To test a system that did not possess this limiting weak layer, a composite containing sapphire fibers, Ti_3Al (super- α_2) matrix, and an interfacial layer of Ta was fabricated. Results of transverse property measurements on this composite are given in Section 5.

3.0 THE INFLUENCE OF Ag/Ta LAYERS ON RESIDUAL STRESSES AND INTERFACIAL PROPERTIES OF Ti₃Al/SCS-6 COMPOSITES

3.1 Materials

Residual stresses and interfacial properties have been measured in the two super- α_2 matrix composites described in the previous section (see also Figure 1), one fabricated with layers of Ag and Ta of $\sim 1\text{-}\mu\text{m}$ thickness and the other with bare fibers. Both were in the form of sheets. The composite without Ag/Ta layers was $\sim 0.7\text{ mm}$ thick and contained ~ 36 volume percent of uniaxially aligned fibers in three rows. The composite with the Ag/Ta layers contained four rows of uniaxially aligned fibers, with a volume fraction of 28 percent and sheet thickness 0.9 mm . Some reaction between the matrix and the outer layers of the fibers occurred during consolidation of the composite with bare fibers, forming a layer of fine-grained silicides and carbides $\sim 2\text{ }\mu\text{m}$ thick around each fiber.⁴ Reaction was not observed in the composite containing Ag/Ta layers.

The composite properties used for the analysis of results in the following sections are listed in Table 1. The elastic modulus of the matrix in the composite with bare fibers was measured previously.² The same value was assumed for the other composite, although this assumption may be questionable because different texturing was observed in the matrices of the two composites (see below).

Table 1
Properties of Super- α_2 /SCS-6 Composites

	Bare Fibers	With Ag/Ta Layers
Young's modulus of matrix	80 GPa	80 GPa
Young's modulus of fiber	414 GPa	414 GPa
Poisson's ratio of fiber	0.3	0.3
Poisson's ratio of matrix	0.3	0.3
Volume fraction of fibers	0.36	0.28
Fiber radius	70 μm	70 μm

3.2 Residual Stresses

The two techniques used to measure residual stresses were x-ray diffraction and selective etching of the matrix. The x-ray measurements of the composite without Ag/Ta layers were done previously, yielding a residual tensile axial stress in the matrix of $450 \pm 50\text{ MPa}$. However, in the composite containing the super- α_2 matrix and PVD layers of Ag-Ta, the matrix exhibited very strong texturing of both the α_2 and β phases, which prevented measurement of residual stresses. Mild texturing of the α_2 phase was also observed in the composite with the Ti-24Al-11Nb matrix with PVD Ag/Ta layers. However, in this case reasonable stress measurements were obtained using the (403) reflection with Co radiation; the longitudinal stress in the matrix was $\approx 420 \pm 70\text{ MPa}$, similar to the stress in the uncoated super- α_2 matrix.

The axial stresses in the fibers were found by measuring the relaxation of the fibers when the matrix was removed. This was done by masking the ends of a rectangular beam and etching away all of the matrix within a long midsection (50-mm length) to leave the two ends joined by bare fibers.² The change in length caused by relaxation of residual stress in the fibers was measured by taking optical micrographs of both ends against a fixed reference gage before and after the matrix was removed. The residual compressive strains thus measured were $(1.56 \pm 0.02) \times 10^{-3}$ for the super- α_2 composite without Ag/Ta layers and

($2.03 \pm 0.030 \times 10^{-3}$ for the super- α_2 composite with Ag/Ta layers. The corresponding axial fiber stresses calculated using a concentric cylinder analysis² (Appendix A) with the properties listed in Table 1 were 800 ± 20 MPa and 1020 ± 30 MPa. The higher stress in the composite with Ag/Ta layers is a direct result of the lower volume fraction of fibers; calculation of the elastic misfit strain yielded 6.11×10^{-3} in both cases. Therefore, as expected, these results indicate that the presence of the Ag/Ta layers has an insignificant effect on the longitudinal residual stress. The residual stress in the composite with bare fibers is also consistent with the above-mentioned x-ray measurement of longitudinal tensile stress in the matrix; with the measured volume fraction of fibers ($f = 0.36$) these two values satisfy the condition for force balance on a cross section of the composite.

3.3 Interfacial Properties

Results. Interfacial debonding and sliding of individual fibers were measured in the two composites using the single fiber pulling test described in detail in Section 5. The results from the composite with bare fibers are presented and analyzed in detail in Section 5. In this section the results from the composite with Ag/Ta layers are presented and compared with those from Appendix A.

Measurements of force and relative sliding displacement for the pullout of two fibers with different embedded lengths (0.66 mm and 1.4 mm) are shown in Figure 2. In both tests the initial loading phase was interrupted once before reaching the peak load, to allow an unload/reload cycle. The partial recovery during unloading and hysteresis during reloading are indicative of frictional sliding between the fibers and matrix.

The peak load for the fiber with the larger embedded length was determined by the failure of the fiber outside the matrix, within the central, etched region. Consequently, there were no data for complete sliding of the embedded length of fiber in this case. The failure load corresponds to a peak stress in the fiber of 3.2 GPa, which falls within the range of strengths typically measured for this type of fiber before consolidation into the composite.

The peak load for the fiber with the shorter embedded length occurred after the entire embedded section had begun sliding. The onset of complete sliding was not accompanied by a sudden load drop as it was for the composite with bare fibers (Figure 4 of Appendix A); instead, after an audible acoustic emission, the load continued to increase continuously (albeit at a slower rate) for the first 10 μm of complete sliding then decreased continuously for the next 5 μm of sliding. The fiber then broke at a position approximately halfway along the embedded length (345 μm from the surface of the matrix), whereupon the load dropped and the displacement increased discontinuously. An increased load was then needed to initiate continued pullout, which subsequently proceeded under decreasing load as the embedded length decreased.

Examination by scanning electron microscopy (SEM) and energy dispersive x-ray analysis of both the fiber after it was pulled completely out of the matrix and the remaining hole indicated that separation and sliding occurred between the two layers of the SCS-6 coating on the fiber, where turbostratic carbon is known to provide a weak layer⁵ (Figure 3). The layers that remained attached to the fiber and matrix were not cracked or otherwise damaged when viewed at low magnification (Figure 3(a) to (c)). However, grooves caused by sliding were evident in some areas at higher magnification (Figure 3(d)).

Analysis. The data from the initial loading regions of Figure 2, corresponding to partial sliding, were compared with the micromechanics analysis of Section 5 to deduce the parameters that characterize the interfacial properties. Two sliding models were considered; one based on the sliding being governed by a Coulomb friction law with friction coefficient μ (Eq. (1) of

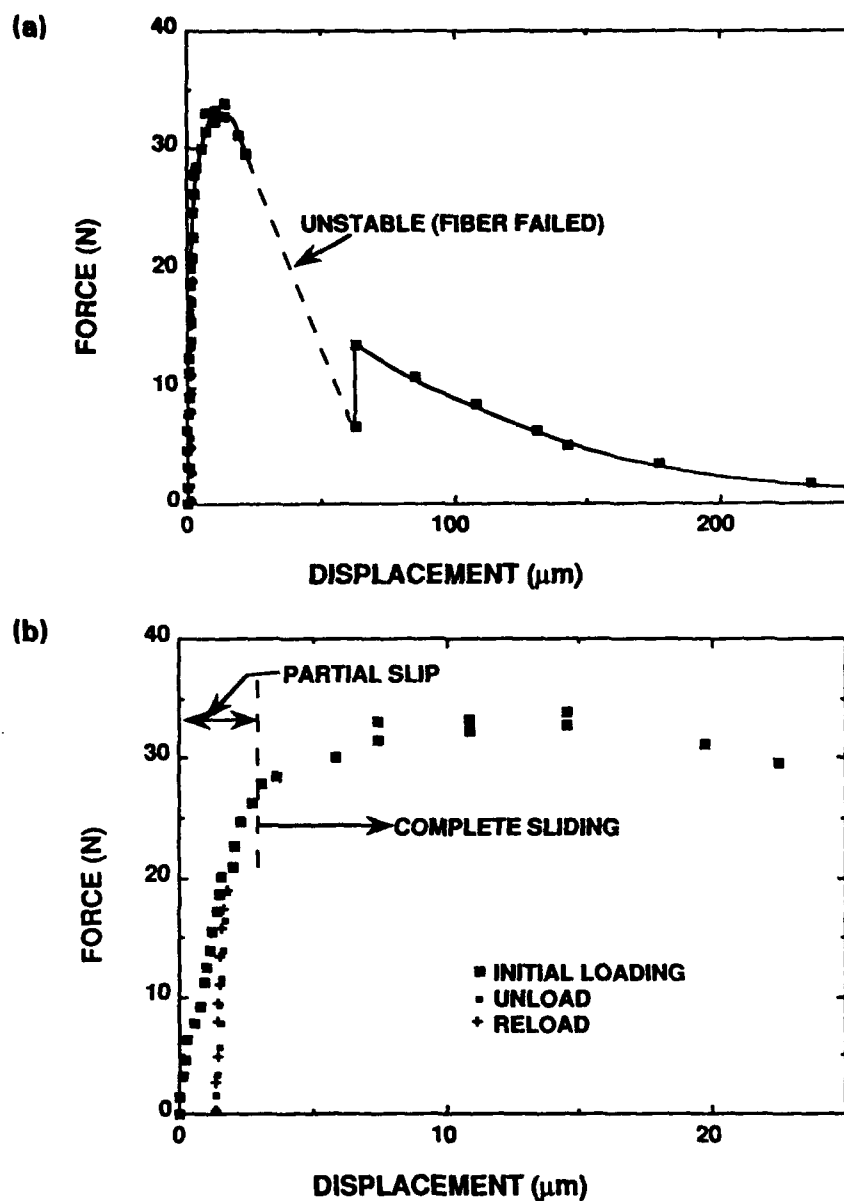


Figure 2 Force and displacement measurements from fiber pulling experiments on super- α_2 /SiC composite with Ag/Ta interfacial layers: (a) embedded length of fiber 660 μm , (b) initial loading data from (a) with expanded displacement scale, (c) embedded length of fiber 1.4 mm.

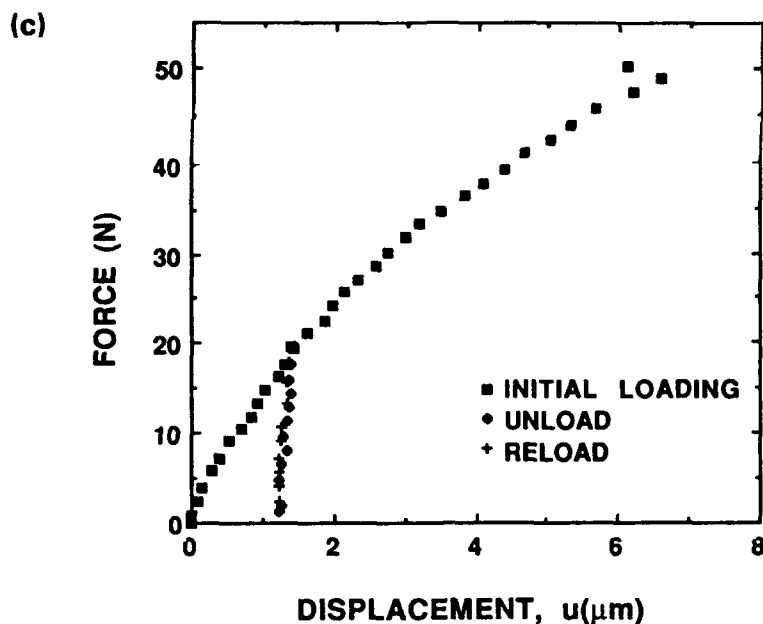


Figure 2 (Continued)

Appendix A) and the other with the sliding being resisted by constant frictional stress, τ_0 (Eq. (2) of Appendix A). The curve fitting procedure used to deduce the parameters differed slightly from that used for the data in Appendix A. In that analysis all of the parameters (τ_0 or μ , debond energy, and residual stress) were determined directly by curve fitting; whereas for the data of Figure 2 the residual stress was set equal to the value measured in the etching experiments described in the previous section, and the debond energy and either τ or μ were determined from a curve fit of the above-mentioned equations to the initial loading data. Then predicted curves for the unload/reload cycle were generated using the calibrated parameters and Eqs. (3) to (6) of Appendix A.

The results of the analysis are shown in Figure 4. For the fiber with the smaller embedded length, both models gave equally good fits to the initial loading data using the parameters listed in Table 2. This comparison was restricted to data at displacements $\leq 3 \mu\text{m}$, based on the assumption that the rapid decrease in slope at larger displacements after the acoustic emission (see Figure 2(b)) indicates the onset of complete sliding. The validity of this assumption was confirmed by calculating the length of fiber over which slip occurred at the largest displacement in Figure 4; for both models the calculated sliding distance was $630 \mu\text{m}$, almost equal to the embedded length of $660 \mu\text{m}$. For the fiber with a longer embedded section, all of the data were used for curve fitting, since there was no evidence of complete sliding before the fiber broke. In this case a significantly better fit to the data was found for the constant friction model than for the Coulomb friction law, although the range of parameters deduced from both models is consistent; the value of τ_0 from the constant friction model falls about midway between the maximum and minimum frictional stresses (τ_{max} and τ_{min}) calculated from the Coulomb friction model at either end of the slip region. Moreover, as expected, the maximum sliding distances calculated from the two models are almost the same (1060 and $1017 \mu\text{m}$) and smaller than the embedded length.

The predicted unload/reload curves in Figure 4 agree reasonably well with the data in all cases. The relative recovery during unloading, and hence the difference between the predictions of the two models for a given data set, are smaller than for the experiments reported in Appendix A (i.e., the composite with bare fibers), because the load at which the unload cycle began was

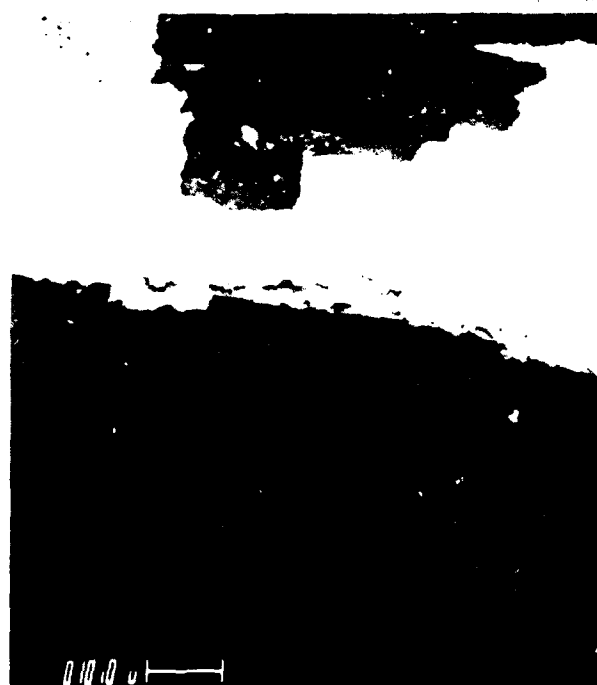


Figure 3 Scanning electron micrographs of specimen used for data of Figures 2(a) and (b) after fiber was pulled entirely out of matrix. Very bright regions on fibers are remnants of the Ag/Ta layers not removed by etching.

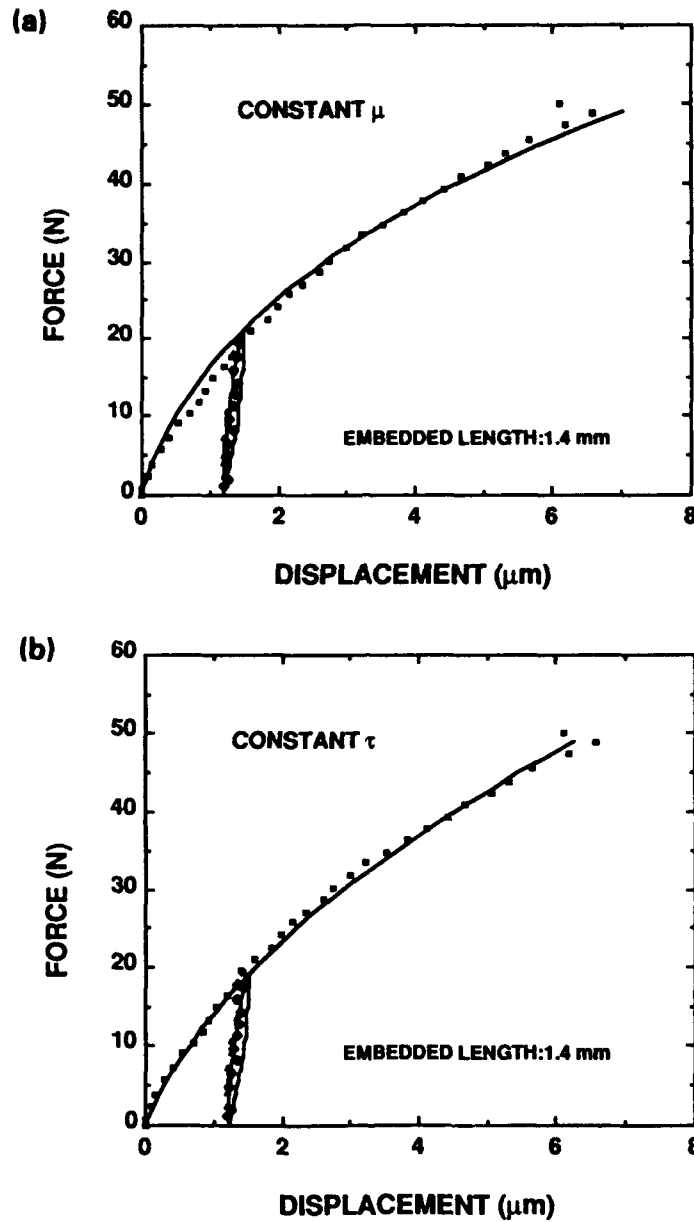


Figure 4 Comparisons of data from initial loading regions of Figures 2(b) and (c) with micromechanical models based on Coulomb friction and perfectly smooth fibers ("constant μ ") and a constant frictional stress ("constant τ "), using the following parameters: elastic constant $A = 1.158$ calculated according to equations in Appendix A with elastic properties in Table 1; residual stress parameter $S_{R0} = 2$ for (a) and (b), $S_{R0} = 3.66$ for (c) and (d), calculated from equations of Appendix A with the measured residual axial stresses in fibers; and friction coefficients or frictional stresses listed in Table 2, obtained by best fit to the initial loading data.

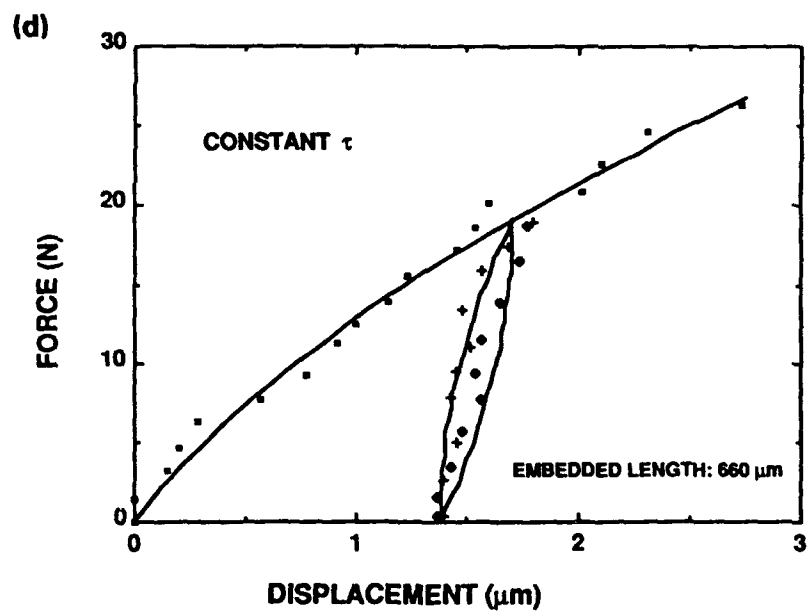
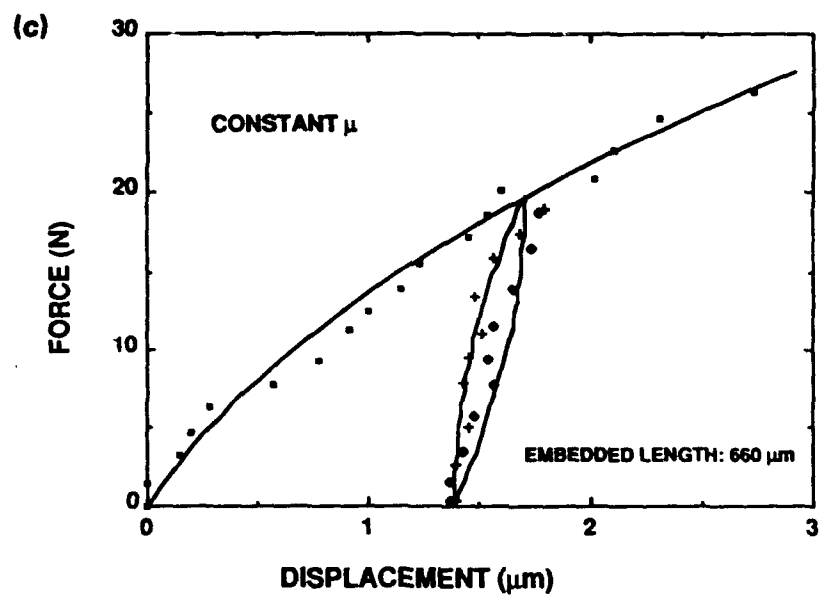


Figure 4 (Continued)

smaller (the *relative* recovery increases with increasing peak load of the unload/reload cycle (Appendix B)).

The curve fits for both models gave the debond parameter $\Gamma = 0$. With Eq. (7) of Appendix A and the parameters of Tables 1 and 2, this provides an upper bound for the intrinsic debond energy of the interface of $\sim 40 \text{ J/m}^2$. We are limited to an upper bound estimate here because *any* debond energy between zero and this upper bound would lead to an *identical* force-displacement relation (Appendix B).

Over the range of displacements in Figure 2 (b) for which the force decreases during pullout of the fiber, the force-displacement relation exhibits a curvature similar to that of the data from the composite with bare fibers in Appendix A. The curvature is opposite to the response expected for sliding dictated by Coulomb friction (with smooth fibers), for which the rate of decrease of the force would increase as the fiber is pulled out. The average sliding resistance $\langle \tau \rangle$ obtained by dividing the applied force by the surface area of fiber remaining embedded in the matrix is plotted in Figure 5; $\langle \tau \rangle$ decreased from an initial value of 103 MPa to $\sim 30 \text{ MPa}$ after $200 \mu\text{m}$ of fiber was pulled out. Similar data from several pullout tests in the composite with bare fibers are also plotted in Figure 5. In all cases $\langle \tau \rangle$ decreased as the fibers pulled out, although the decrease was smaller in the composite with bare fibers.

Table 2
Interfacial Parameters Determined from Curve Fit
to Initial Load Data

	Embedded Length	
	1.4 mm*	660 μ
<u>Coulomb Model</u>		
μ	0.56	0.44
τ_{\max} (MPa)	145	114
τ_{\min} (MPa)	72	83
l_{\max} (μm)	1060	630
<u>Constant Friction Model</u>		
τ_0 (MPa)	110	98
l_{\max} (μm)	1017	630

*A significantly better fit to the initial loading data was obtained from the constant friction model than from the Coulomb model.

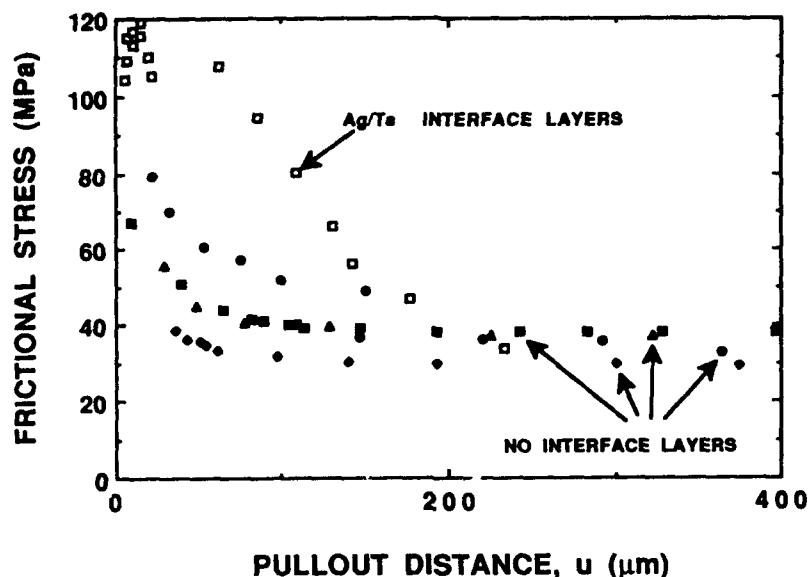


Figure 5 Average frictional stress during fiber pullout.

3.4 Discussion

Several differences in interfacial sliding behavior were observed in the super- α_2 matrix composites with and without Ag/Ta layers between the fibers and matrix. In the composite with bare fibers, the surface of separation and sliding was between the outer coating of the SCS-6 fibers and the layer of reaction products, the intrinsic debond energy was $< 26 \text{ J/m}^2$, and the frictional sliding over the debonded surface clearly exhibited a response characteristic of a constant frictional stress ($\tau_0 = 66 \text{ MPa}$) rather than a Coulomb friction law. The role of asperities on the surface of the fiber as a likely source of this response is discussed in Appendix A.

In the composite with the Ag/Ta layers, the surface of separation was *between* the coating layers that form the outer part of the SCS-6 fiber. Evidently the Ag/Ta either formed a stronger bond or had a larger frictional resistance with the fiber than did the reaction product layer in the other composite. The upper bound estimates for the debond energies are similar for the two composites. The frictional stress τ_0 was higher ($\approx 100 \text{ MPa}$) between the coating layers of the fibers in the composite containing Ag/Ta than between the outer surface of the fiber and the reaction products of the other composite, as it must be for the sliding to have taken place at the reaction/product interface. The frictional sliding data for the composite with Ag/Ta layers followed the predictions of a constant friction model slightly better than those of a Coulomb friction model, although the distinction was not as great as it was for the other composite.

The residual axial stress in the fibers is larger in the composite with Ag/Ta layers (1020 MPa c.f. 800 MPa). However, that difference can be attributed entirely to the different volume fraction of fibers in the two composites. The residual stress normal to the interface was not measured. If we assume that the misfit strains between the fibers and matrices are isotropic, the lower volume fraction of fibers in the composite with Ag/Ta layers would result also in a higher residual stress normal to the interface (300 MPa c.f. 260 MPa). However, this increase in residual normal stress is not sufficient to account for the observed larger sliding resistance in the composite with Ag/Ta layers (i.e., there is an increase in friction coefficient as well).

The presence of Ag-Ta layers has the potential of reducing the residual stress normal to the interface, in which case the elastic misfit strain defined in Appendix B would be anisotropic. The analysis of the fiber pullout data in terms of the Coulomb friction model assumed that the misfit strain was isotropic; similar analysis using an anisotropic misfit strain, which accounts for relaxation of residual normal stress by plastic flow, gives predictions that deviate further from the experimental data.

4.0 FATIGUE CRACK GROWTH IN Ti₃Al/SCS-6 COMPOSITES WITH AND WITHOUT Ag/Ta INTERFACIAL LAYERS

Fatigue crack growth rates and crack opening profiles have been measured in air and vacuum in the two composites described in Section 3.1. Both composites contained super- α_2 matrices and SCS-6 fibers, one being fabricated with uncoated fibers and the other with PVD Ag/Ta layers ($\sim 1 \mu\text{m}$ thickness) on the fibers.

4.1 Experiments

Notched beams fabricated from both composites with the fibers in the longitudinal direction were loaded in bending on the stage of an SEM. This mode of loading was chosen to allow high resolution in situ imaging, from which accurate measurements of crack opening displacements could be obtained using stereoscopy.⁶ Experiments were done in both air and vacuum (the vacuum being provided by the SEM). The experiments in air were done using the same loading stage, but removed from the microscope, with interruptions at various stages to allow imaging in the SEM.

The load was cycled between zero and a constant maximum load at a frequency of ~ 2 cycles/min. Although the applied loads and crack lengths were monitored, the results were not interpreted in terms of applied stress intensity factors because crack growth was not always coplanar; in this case accurate calibration of stress intensity factors would require finite element calculations. The maximum applied stresses were chosen as follows. First the experiments on the composite containing Ag/Ta layers were done using the same stress in both air and vacuum, the stress being chosen to give crack growth rates in the range 0.1 to 50 $\mu\text{m}/\text{cycle}$. Then for the composite with uncoated fibers, the peak loads in air and vacuum were chosen to give the same crack growth rates as in the corresponding experiments in the composite that contained Ag/Ta. This load was ~ 25 percent lower in air and 5 percent higher in vacuum.

4.2 Results

4.2.1 Crack Growth Rates

In the composite containing Ag/Ta layers, a single fatigue crack initiated from the base of each notch and grew stably in a coplanar manner (i.e., normal to the applied tensile stress). The initial growth rate in air was higher, by a factor of about 10, than in vacuum (Figure 6). However, in both environments the growth rate decreased rapidly as the cracks extended, even though the peak applied stress intensity factor increased (increasing crack length at constant stress amplitude). Such decreasing growth rates are characteristic of cracks that are affected by bridging forces due to reinforcing fibers. As the crack grows the bridging zone length increases, leading to an increase in the bridging stress intensity factor, which acts to reduce the crack opening and thus decrease the net crack tip stress intensity factor. Since the crack growth rate is dictated by events at the crack tip, a decrease in the crack tip stress intensity factor leads to a reduction of crack growth rate.

In the composite with uncoated fibers, the crack always initiated in a coplanar manner from the notch root, but after growing for about 20 μm the crack deflected to a plane oriented at $\sim 45^\circ$ from the applied loading direction. In this case the crack lengths and crack opening displacements are reported as projected values parallel and perpendicular to the original crack plane. The crack growth rates in both air and vacuum decreased as the cracks extended, as in the composite containing Ag/Ta.

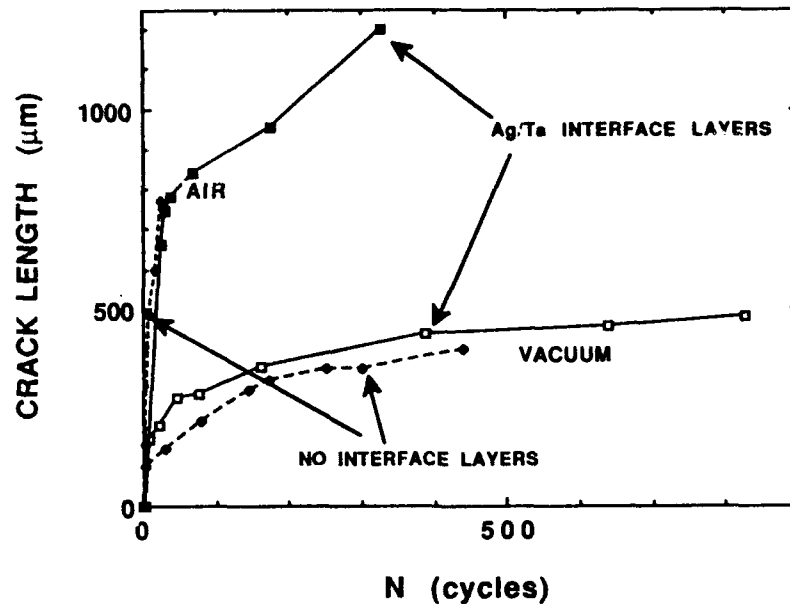


Figure 6 Comparison of crack growth under cyclic loading in super- α_2 /SCS-6 composites with and without Ag/Ta layers between matrix and fibers.

4.2.2 Crack Opening Displacements

Measurements of crack opening displacements as a function of position within the cracks were obtained from SEM micrographs such as Figure 7. The displacements were obtained by comparison of micrographs taken before and after passage of the crack, with stereoscopy used to measure relative displacements of image features either side of the crack. With this technique displacement sensitivity of $\sim 0.1 \mu\text{m}$ was readily attained from relatively low magnification micrographs such as those of Figure 7. Typical measurements of crack opening displacements at maximum load, u_{max} , minimum load, u_{min} , and the difference, u_{cyclic} , are shown in Figure 8.

A large difference was observed in the residual crack opening displacements after unloading in air and vacuum. For both composites, the crack opening after unloading, u_{min} , in vacuum, was small ($u_{\text{min}}/u_{\text{max}} \leq 0.1$); whereas in air u_{min} was substantially larger ($u_{\text{min}}/u_{\text{max}} \sim 0.3$). This difference is evident in the data of Figure 8 as well as in the micrographs of Figure 7, where, for the vacuum tests the unloaded crack is not easily discernible.

In both air and vacuum environments, the crack opening displacements (both u_{max} and u_{cyclic}) at positions more than $\sim 200 \mu\text{m}$ from the crack tip are smaller in the composite with Ag/Ta layers than in the one without. The difference is clearer in the air environment. Moreover, in this case the applied stress is 20 percent higher on the composite with the Ag/Ta layers. These two results suggest that the bridging effect of the fibers is larger in the composite with the Ag/Ta layers than in the composite without. However, the difference is not large.

The cyclic displacements for cracks of length $\sim 600 \mu\text{m}$ in all four combinations of environment and composite type are plotted together in Figure 9. Notwithstanding the small differences noted above, all of the crack profiles appear remarkably similar, especially close to the crack tip. Therefore, the crack tip stress intensity factors K_{tip} are similar in all cases. However, the growth rates for these cracks in air are larger by a factor of ~ 100 than those of the cracks in vacuum. These results indicate that the environmental effect that causes this difference in growth

rate must act by modifying the crack tip growth law (i.e., the relation between da/dN and ΔK_{tip} in the matrix) rather than by degrading the bridging tractions.

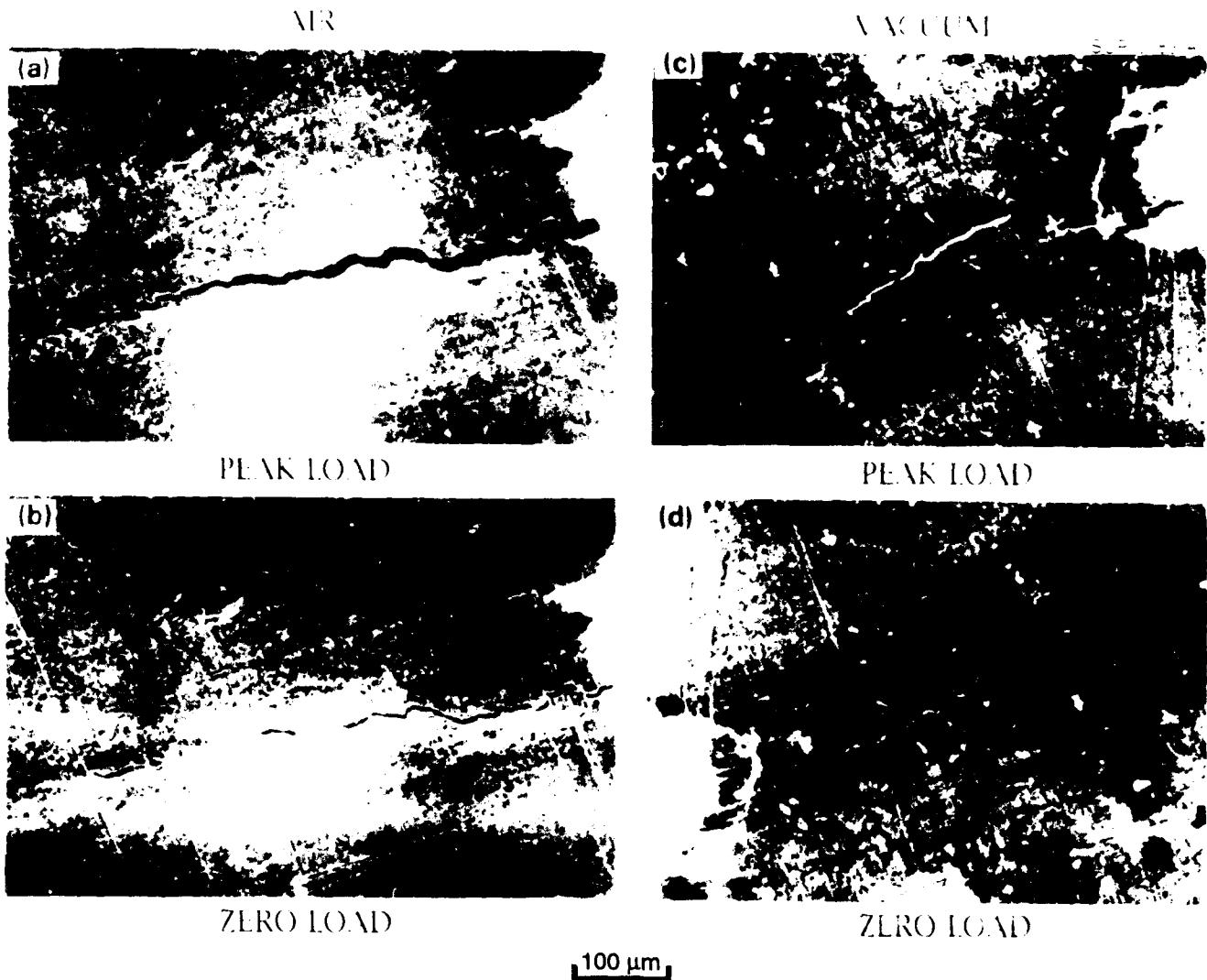
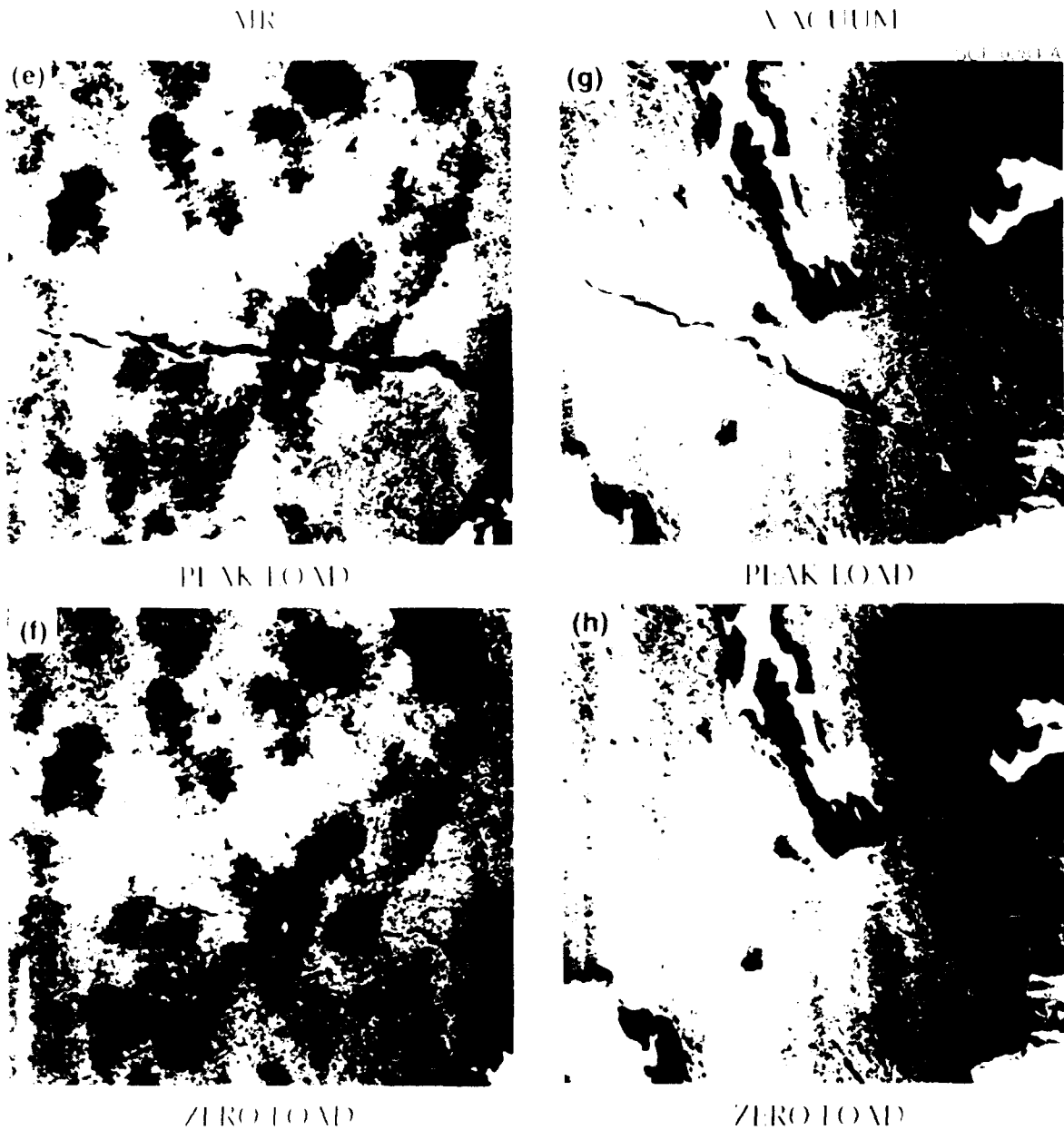


Figure 7 Scanning electron micrographs showing fatigue cracks at maximum and minimum (zero) load.



100 μm

Figure 7 (Continued)

The crack opening displacements near the tip of the crack in the Ag/Ta-containing composite are shown in Figure 10(a) at various stages of growth. A steady decrease in tip opening is evident as the number of cycles increases, corresponding to decreasing crack growth rate. The crack growth rates are plotted as a function of the crack opening at a nominal fixed distance from the tip ($35\text{ }\mu\text{m}$) in Figure 10(b). Since these crack opening displacements scale with the crack tip stress intensity factor ΔK_{tip} , the plot of Figure 10 (b) represents the relative variation of growth rate with ΔK_{tip} .

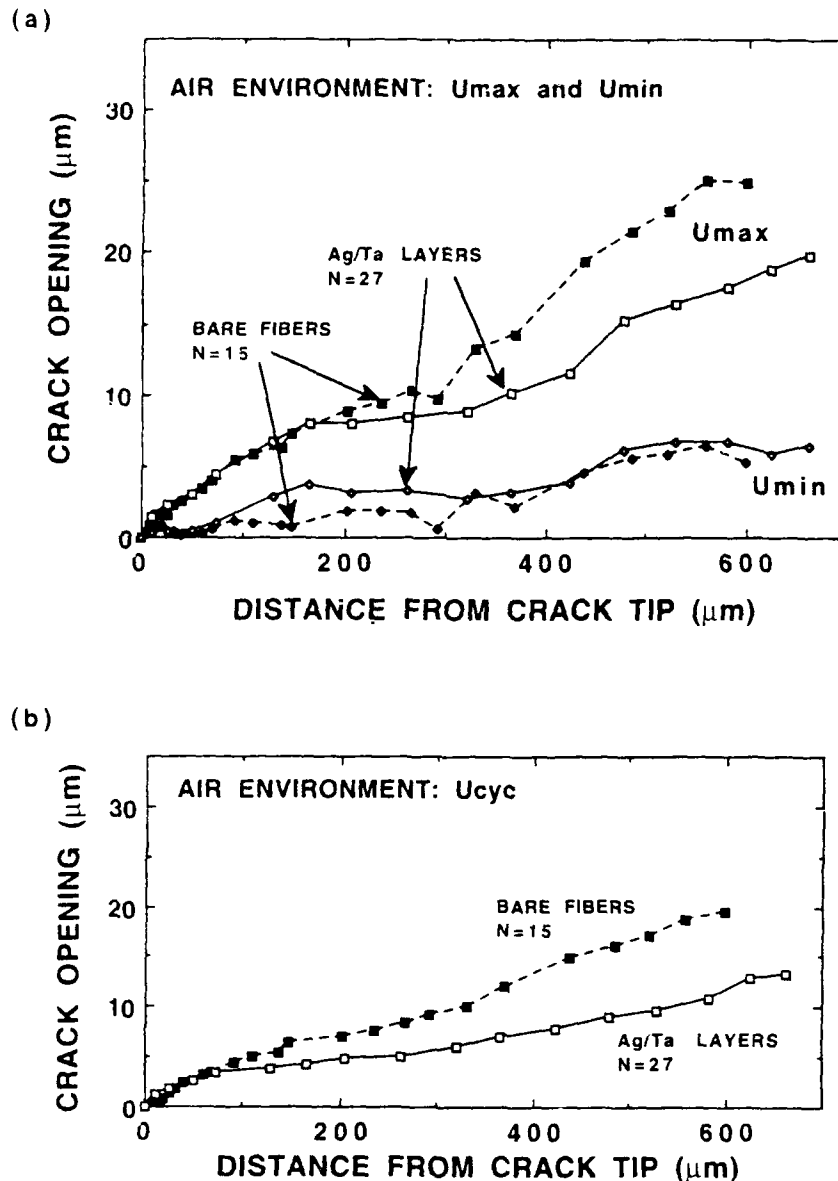
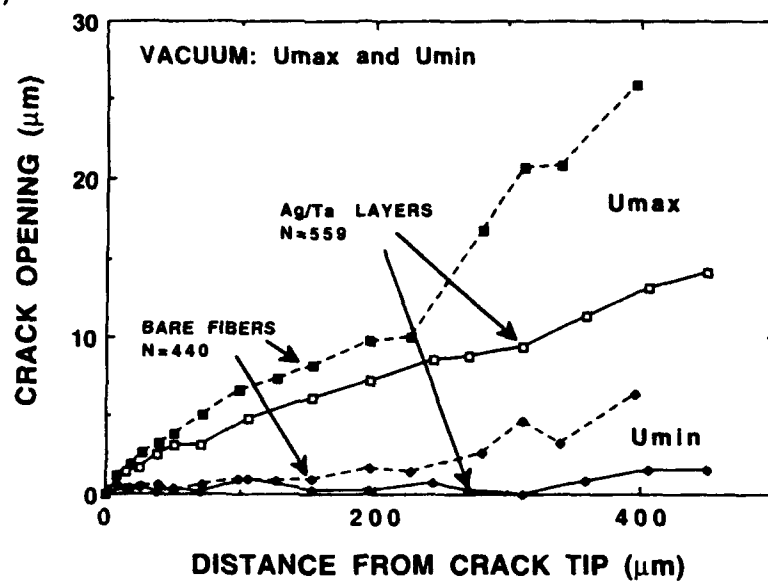


Figure 8 Crack opening displacements at maximum load (u_{max}), minimum (zero) load (u_{min}) and the difference ($u_{cyc} = u_{max} - u_{min}$), for fatigue cracks of approximately the same length in both composites. (a) and (b) air environment; (c) and (d) vacuum environment. N is the number of load cycles applied to the crack.

(c)



(d)

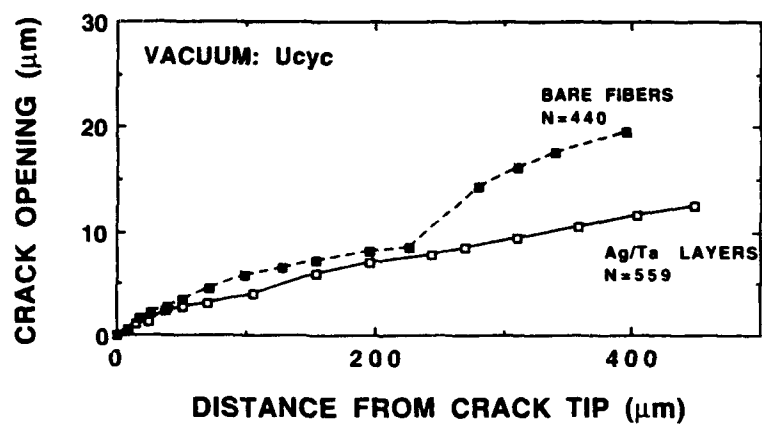


Figure 8 (Continued)

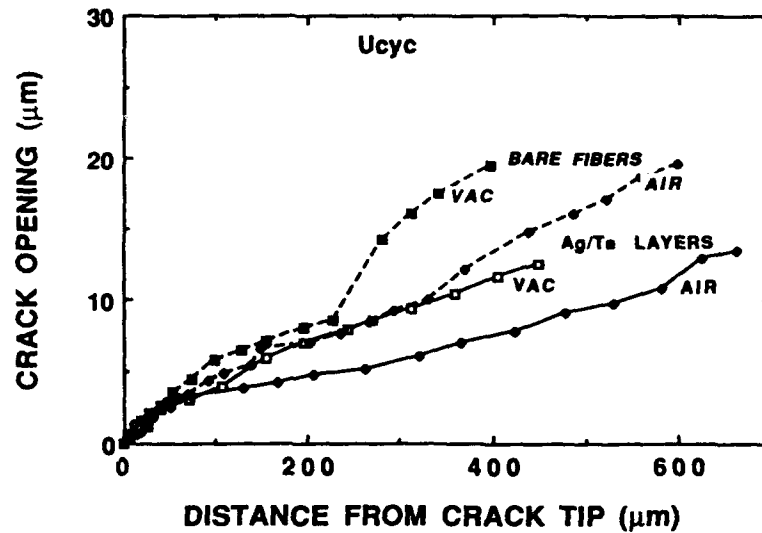


Figure 9 Comparison of cyclic crack opening displacements for cracks of approximately the same length in both composites, in air and vacuum.

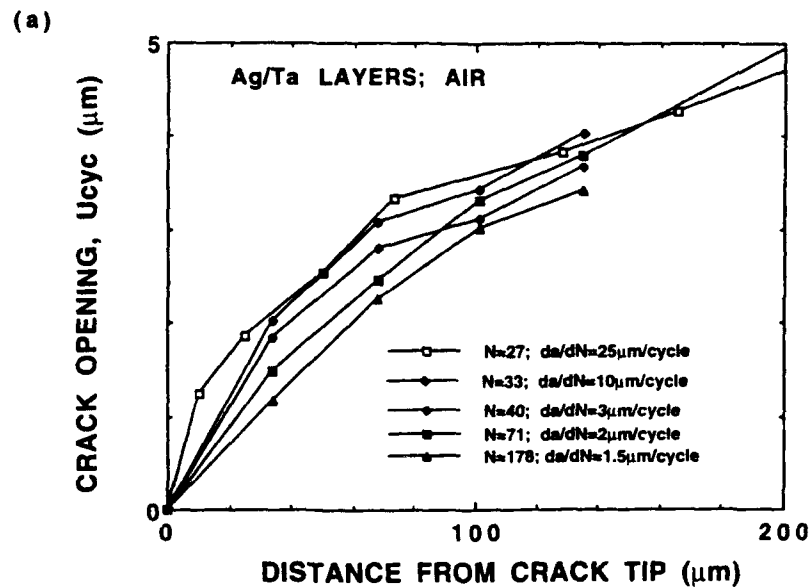


Figure 10 (a) Comparison of crack opening displacements (cyclic) near the tip of a fatigue crack at various stages of growth in air in the composite with Ag/Ta interfacial layers. (b) Variation of crack growth rate with crack opening.

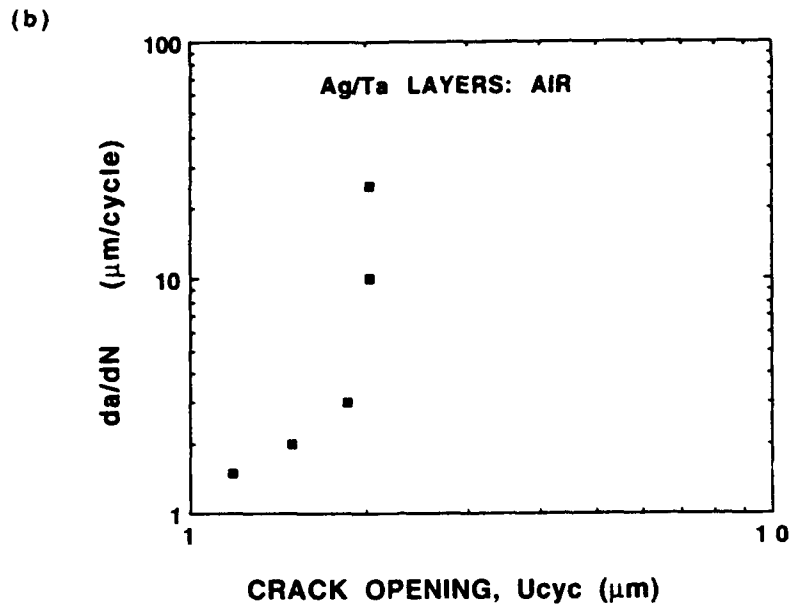


Figure 10 (Continued)

4.3 Discussion and Conclusions

Fatigue crack growth rates in a given environment (air or vacuum) are very similar in the two composites (super- α_2 /SCS-6 with and without Ag/Ta interfacial layers), although the experiments in air suggest that crack bridging by the fibers is slightly more effective in retarding crack growth in the composite with the Ag/Ta layers than in the composite without Ag/Ta (20 percent higher load was needed to obtain equivalent growth rates). The results are consistent with the interfacial property measurements described in Section 3, which indicated that the fiber pullout responses were similar in the two composites. In the single fiber pullout experiments, debonding occurred between the fibers and reaction products, with a frictional sliding resistance (τ) of ~ 65 MPa, in the composite without Ag/Ta layers; whereas in the composite with Ag/Ta layers debonding and sliding occurred between the SCS-6 layers and the fiber, with higher sliding resistance ($\tau \approx 100$ MPa). Thus, while the Ag/Ta layers improved the bonding (or the sliding resistance) between the fibers and matrix, this only removed the weakest of several relatively weak interfacial debonding sites. This results in slightly higher bridging forces but does not have a dramatic effect on growth rates.

A much larger difference was observed between crack growth rates in air and vacuum. The growth rates in both composites were larger in air than in vacuum, by a factor of 10 for initial crack growth at given load, and by a factor of 100 at given crack tip opening displacement after the cracks had grown for ~ 600 μm . Crack opening measurements indicated that the enhanced growth rates in air resulted from an increase in the intrinsic growth rate in the matrix at the crack tip (i.e., increased da/dN at given ΔK_{tip}), rather than from degradation of the bridging effect of the fibers. Nevertheless, the air environment clearly caused an increase in the crack opening displacements at minimum load. However, this effect would tend to reduce ΔK_{tip} and thus lower growth rates. The results are consistent with the enhanced growth rates observed in our other studies of $\text{Ti}_3\text{Al}/\text{SCS-6}$ composites.⁷ They are also consistent with other studies of fatigue crack growth in monolithic Ti alloys (Ti-6Al-4V)^{8,9} which show almost an order of magnitude increase in growth rate in air compared with vacuum at given stress intensity factor range. However, the range of growth rates

in the present study lies at larger values (10^{-7} to 10^{-4} m/cycle) than in the monolithic material studies (10^{-10} to 10^{-6} m/cycle).

A consistent difference was observed in the crack geometry resulting from cyclic tensile loading parallel to the fibers in the two composites. In both air and vacuum the cracks in the composite with Ag/Ta layers grew normal to the fibers, whereas in the composite without Ag/Ta layers the cracks grew at an angle of $\sim 45^\circ$ to the fibers. The reason for this difference is not known.

5.0 INTERFACIAL PROPERTIES OF A SAPPHIRE/Ta/Ti₃Al COMPOSITE

5.1 Materials Fabrication

To allow investigation of interfacial bond strengths higher than those limited by the weak outer layers of the SCS-6 SiC fibers, composites containing sapphire fibers and super- α_2 matrix were fabricated in collaboration with Rick Everett of NRL. Tantalum was chosen as an interfacial coating to prevent reaction between fibers and matrix and to provide a ductile layer at the interface.

The sapphire fibers[†] of diameter 80 μm were wound with uniform spacing on a drum and cut into rectangular racks of fibers $\sim 2'' \times 1''$ held together by thin lines of epoxy glue at their ends. The fibers were then coated with $\sim 1 \mu\text{m}$ of Ta by PVD at NRL. The fibers were then laid up with alternating layers of super- α_2 foil to form a uniaxial composite with four layers of fibers and were consolidated by hot pressing.

5.2 Microstructure

An optical micrograph of a cross section of the composite is shown in Figure 11. Movement of the fibers occurred during consolidation, although most fibers remained well spaced. Most fibers have a rounded hexagonal cross section. Observation of longitudinal sections indicated that fibers were broken during consolidation, mostly into two or three pieces within the 2" lengths of composite. These breaks did not affect the transverse loading experiments described below. The typical transverse test specimen of $\sim 2\text{-mm}$ thickness contained only a few broken fibers, which could be readily identified; and failure was never observed to initiate from the broken fibers. The broken fibers were identified by viewing the surface in reflected polarized light with an analyzing polarizer set at 90° . Fibers that were intact through the entire section appeared black, whereas fibers that contained fractures appeared bright because of internal reflections which changed polarization and allowed light to pass through the analyzer (Figure 12).

The Ta coatings on most fibers were continuous with uniform thicknesses of $\sim 1 \mu\text{m}$ (Figure 13). Surrounding each fiber was a layer of matrix of $\sim 5\text{-}\mu\text{m}$ thickness in which the β phase was depleted. Otherwise, there was no evidence of reaction among the matrix, coating, or fiber. However, there were occasional regions where the coating was missing (Figure 14), typically on several fibers in a cross section containing approximately 400 fibers. In these regions, dissolution of the fiber into the matrix had clearly begun during consolidation. This observation demonstrates the importance of the Ta coatings in protecting the fibers. The small regions of missing coating did not appear to play a role in the transverse tension experiments described below.

The uniformity of the β -depleted zone around each fiber suggests that the β -depletion is associated with the fully coated fiber rather than being due to the occasional small region in which the coating was missing. However, the presence of the β -depleted zone is puzzling, because any diffusion of Ta from the coating would lead to stabilization of the β phase. The only available source of β depletion is oxygen, either from the Ta coating or from the Al_2O_3 fiber via diffusion through the Ta coating. The Ta coating was deposited in a high vacuum ($\sim 10^{-7}$ torr). Therefore, a large amount of oxygen would not be expected in the coating. However, there is insufficient information about the amount of oxygen needed to stabilize the α_2 phase in this region to distinguish these two possibilities.

[†] Saphikon

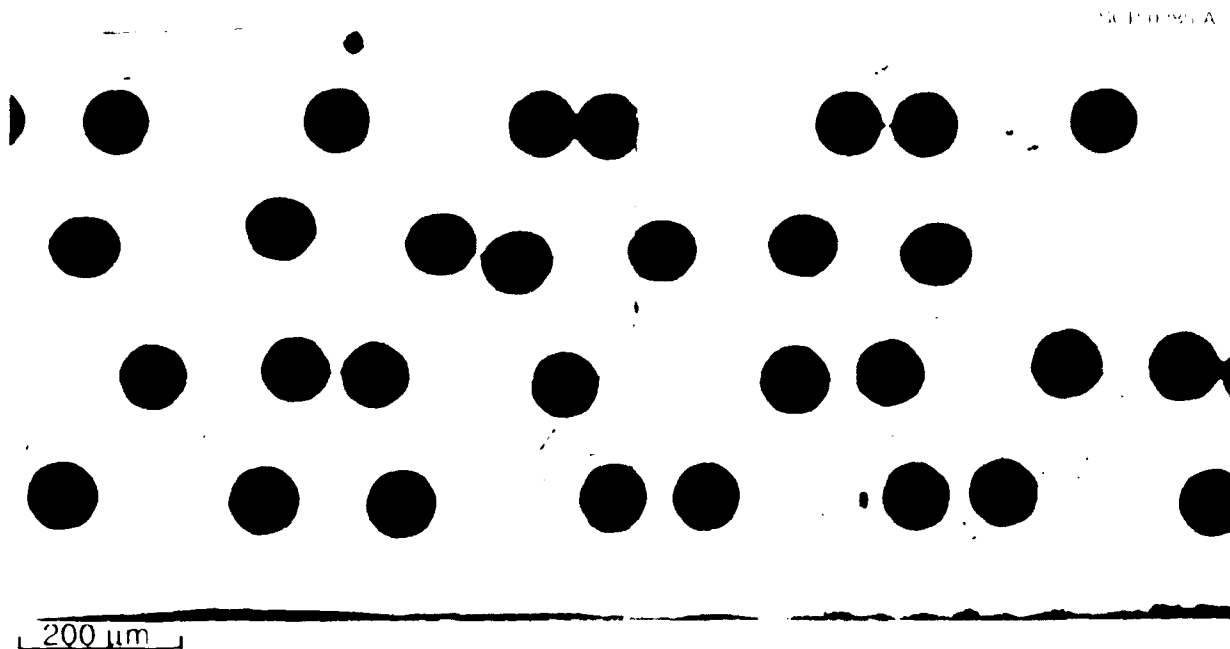


Figure 11 Optical micrograph of cross section of sapphire/Ta/super- α_2 composite. Reflected light with polarizer and analyzer at 89° .

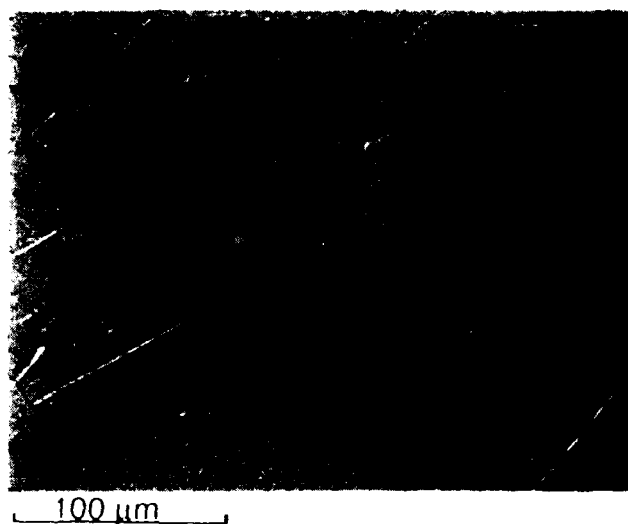


Figure 12 Optical micrograph showing broken (bright) and intact (dark) fibers in sapphire/Ta/super- α_2 tensile test specimen of 2 mm thickness. Reflected light with polarizer and analyzer set at 89° .

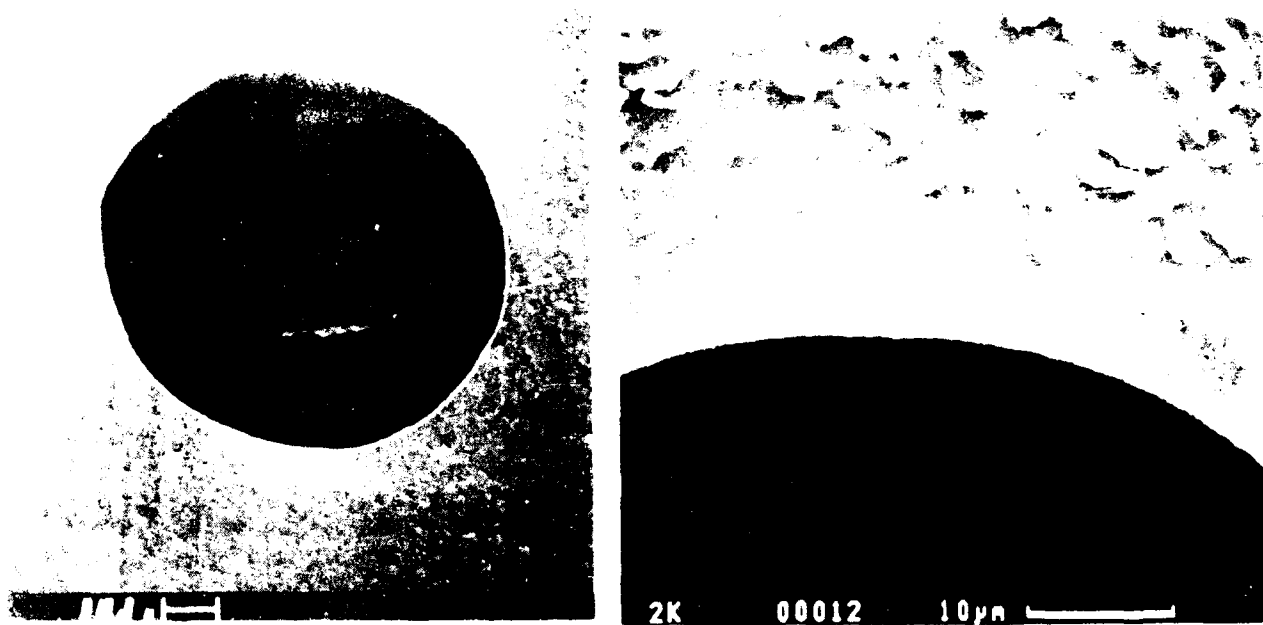


Figure 13. Scanning electron micrographs showing sapphire fiber in super- α_2 matrix. Bright line surrounding fiber is Ta coating. Bright regions of matrix are β phase; dark regions are α_2 phase.



Figure 14. Scanning electron micrograph showing region of fiber-matrix interface in which Ta layer was missing.

5.3 Transverse Property Measurements and Damage Observation

Rectangular specimens ($\sim 50 \times 2$ mm) were cut from the composite panels (thickness ~ 0.8 mm) and tested in transverse tension. The cut faces were polished using $1/4\text{-}\mu\text{m}$ diamond to remove obvious damage caused by cutting. The tensile load was applied using a fixture attached to a stage of an optical microscope, thus allowing in situ observation of damage development prior to failure. The load was monitored using a load cell and the average strain was measured using a strain gage attached to the side of the specimen opposite that being observed.

A typical stress-strain curve is shown in Figure 15. The curve is linear (and elastic as confirmed by unload-reload cycles) at loads up to 90 percent of the failure load. The elastic modulus is 150 GPa, consistent with that expected for a strongly bonded composite.¹⁰ Over the last 10 percent of loading, a small plastic strain ($\sim 10^{-4}$) occurred.

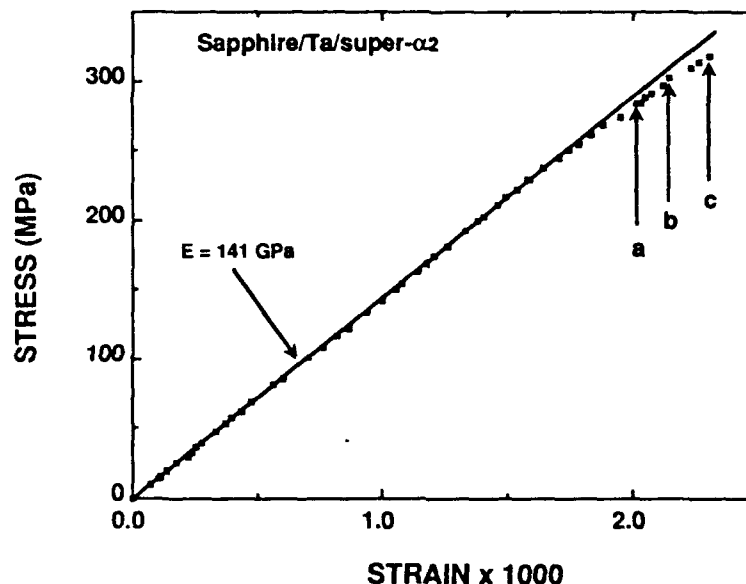


Figure 15 Stress-strain curve for transverse loading of sapphire/Ta/super- α_2 composite. The labels a, b and c indicate the loads at which the in situ micrographs of Figure 16(a,c) were obtained.

The in situ observations revealed the sequence of damage prior to failure as shown in Figure 16. The first damage, which coincided approximately with the onset of nonlinearity of the stress-strain curve, was in the form of cracks in the fibers, oriented normal to the applied load. With continued loading, similar cracks formed in larger numbers of fibers and extended into the matrix. Cracks also formed within the matrix near the edges of the β -depleted zones surrounding the fibers (Figure 16 (b)). Failure resulted from linkage of cracks in and near adjacent fibers, as shown in Figure 16 (c). At the failure point approximately 20 percent of the fibers within the test section contained cracks, and another 20 percent had cracks in the adjacent regions of matrix.

The strength of the fiber/matrix interface is of particular interest in this study. Several observations indicate that the bond strength is high in this composite and that interfacial debonding or plasticity was not a factor in the failure process under tensile transverse loading. The first observation is that the cracks in the fibers penetrated into the matrix without any sign of deflection or offset at the interface, even when the cracks were inclined to the interface (Figure 17). The absence of interaction between the crack and the interface is seen also on the fracture surface

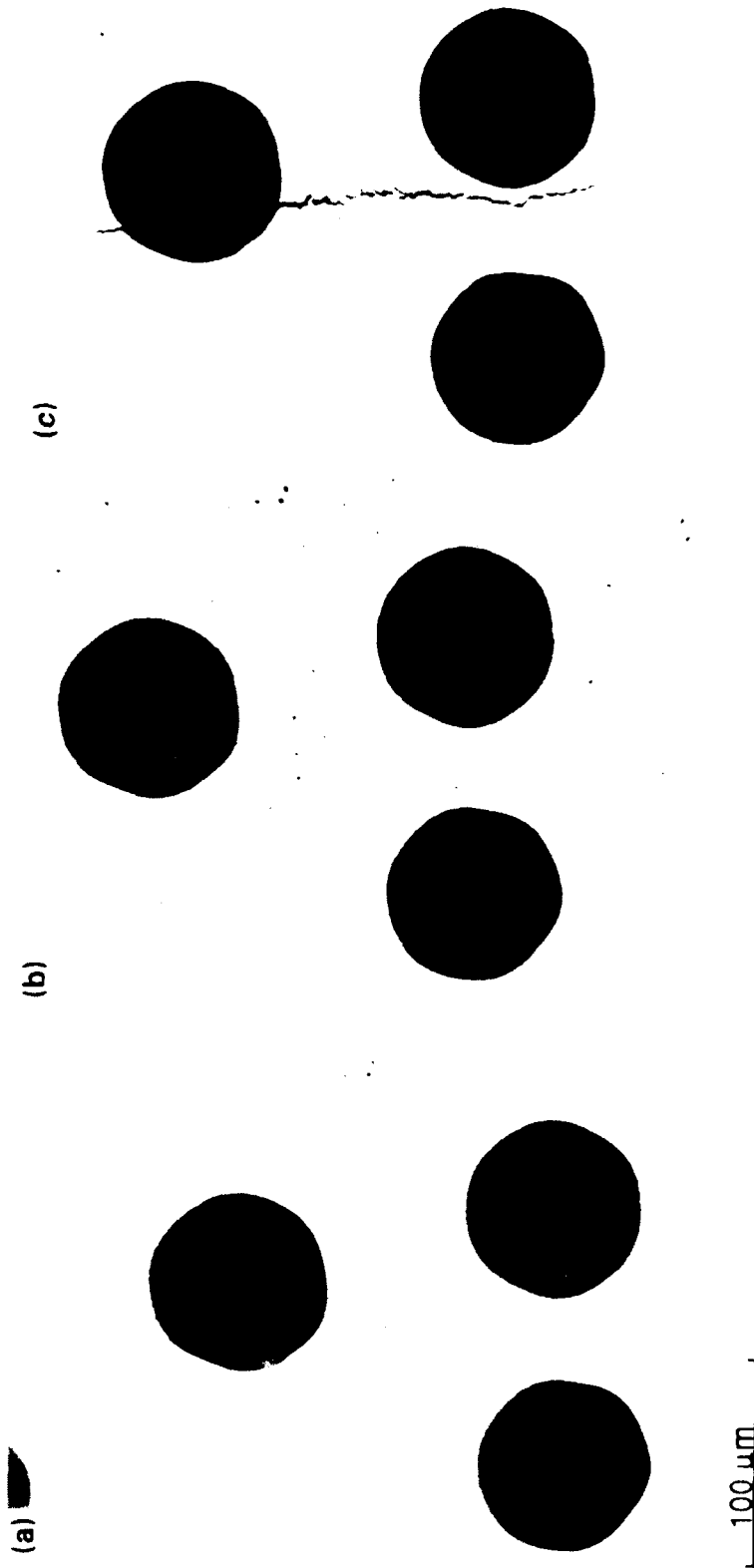


Figure 16 Sequence of in situ optical micrographs taken from one area at loads of (a) 0.9, (b) 0.95, (c) 0.99 of the failure load, corresponding to the positions labeled (a) (b) and (c) in Figure 15. Failure occurred by linking of the cracks in (c). Applied load horizontal.

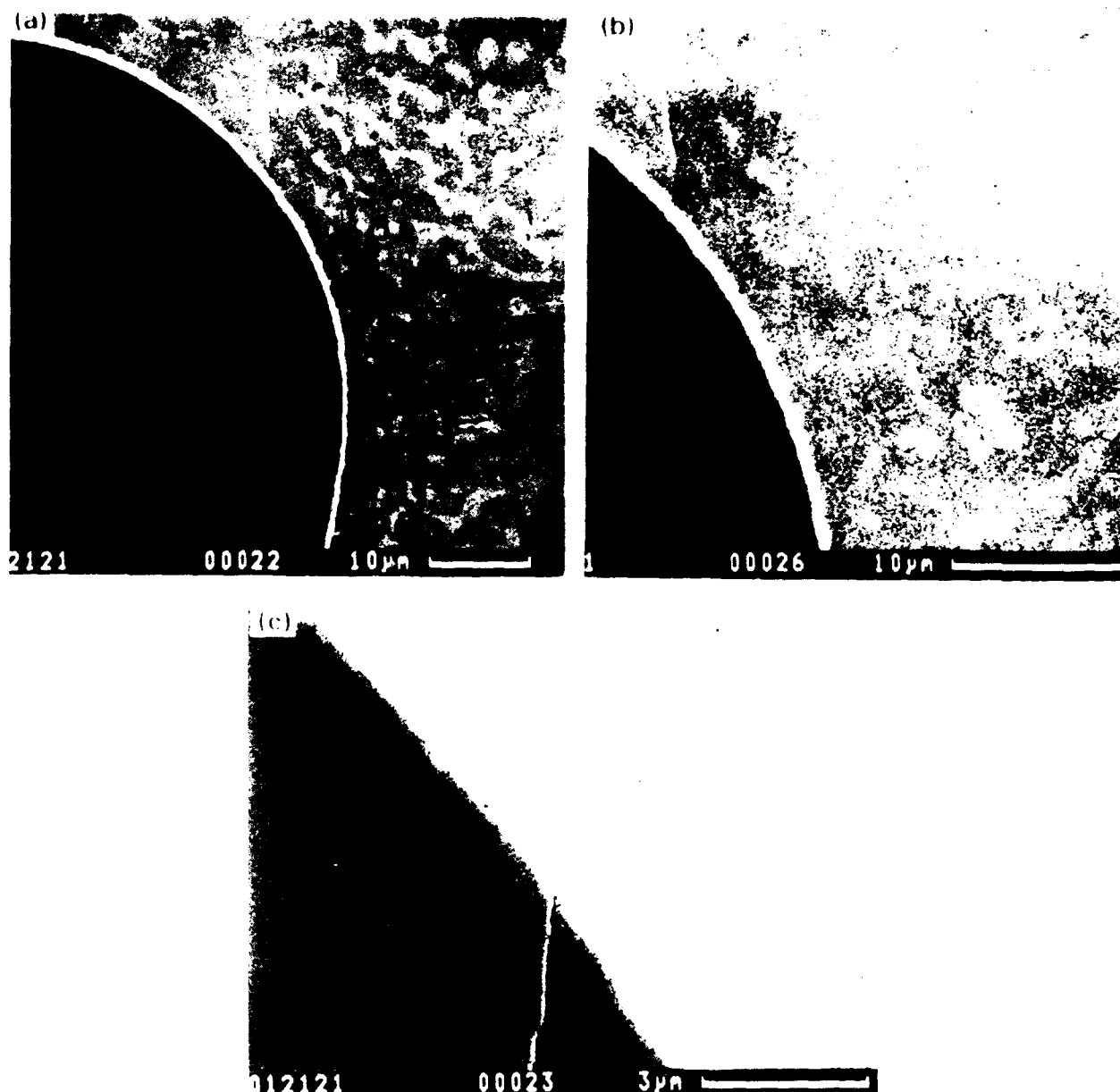


Figure 17 Scanning electron micrograph showing crack path across the fiber matrix interfacial region.

(Figure 18). The second observation is that cracks formed in the matrix parallel to, and about 10 μm from, the interfacial regions that were subject to the maximum tensile stress; while no debonding was observed at the interface. This indicates that the strength of the interface is larger than that of the matrix.

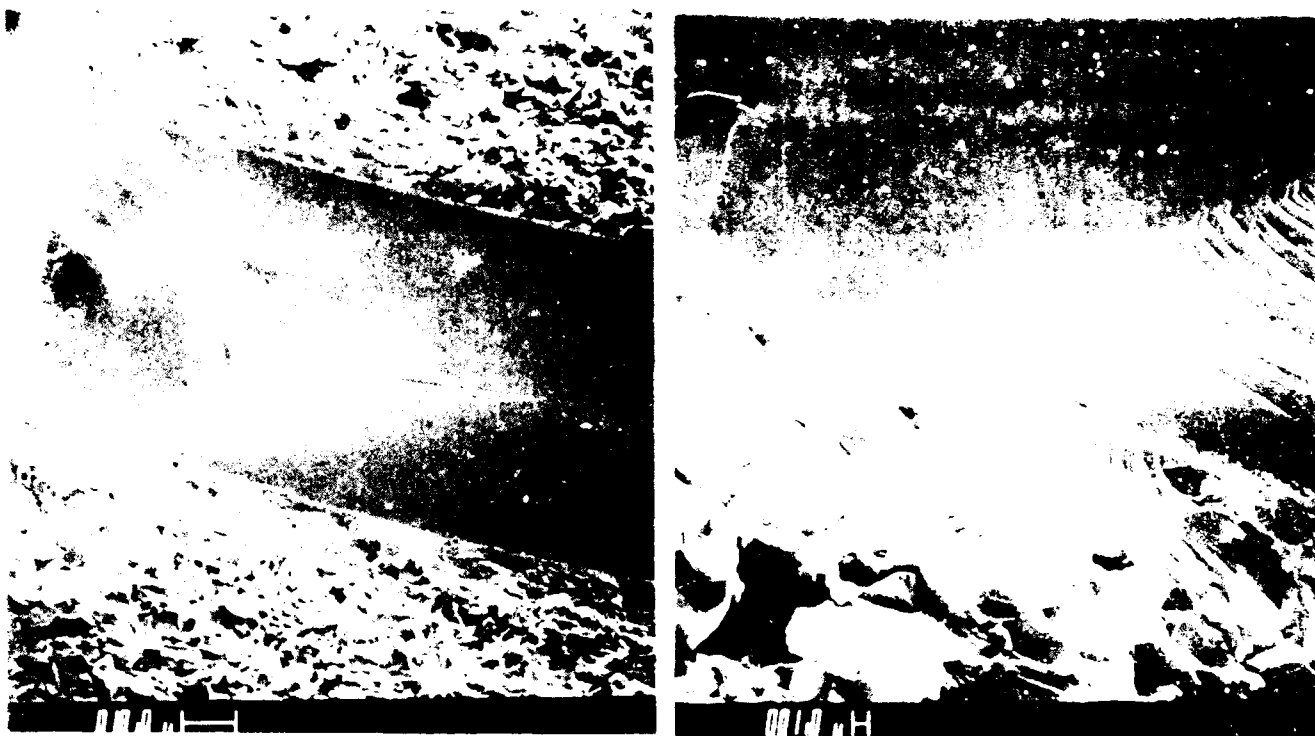


Figure 18. Scanning electron micrograph showing fracture surface resulting from transverse tensile loading of sapphire/Ta super- α_2 composite. Smooth region is axial split with central split; rough region is the super- α_2 matrix.

5.4 Discussion and Conclusions

The damage that led to transverse failure of the sapphire/Ta super- α_2 composite differed from that observed in the SCS-6 containing composites. The various damage modes were observed in all of the composites are summarized schematically in Figure 19. In the SCS-6 super- α_2 composite the sequence of damage prior to failure consisted of formation of longitudinal radial cracks in the matrix, debonding of the interface, and formation of transverse radial cracks in the matrix. Failure occurred by the linking of transverse radial cracks and debonded interfaces of adjacent fibers at an applied stress of ~ 200 MPa. In the SCS-6 Ag/Ta super- α_2 composite, interfacial debonding and longitudinal matrix cracking occurred, but transverse radial cracks did not form prior to failure. The corresponding strength was larger by a factor of 2 and the strain to failure was larger by a factor of 3. The difference between the two composites was attributed to the effect of the Ag/Ta layers in preventing formation of brittle reaction products, which are known initiation sites. In addition, there was a layer of *300 nm* thick matrix adjacent to the fibers in the Ag/Ta containing composite, which further suppressed cracking. In the sapphire/Ta super- α_2 composite, cracking of the fiber and circumferential matrix cracking occurred prior to failure.

The existence of different damage modes in these different composites can be quantified quantitatively by examining the stress field surrounding an isolated fiber under transverse load. The use of elastic analysis is justified for these composites on the basis of their linear load-strain curves (at least up to the initiation of the damage being discussed). More sophisticated calculations accounting for multiple fiber interactions lead to quantitatively similar results. The elastic stresses at the interface and in the surrounding matrix are shown in Figure 20 for a composite with a fully bonded interface and elastic moduli corresponding to the fibers and matrix as

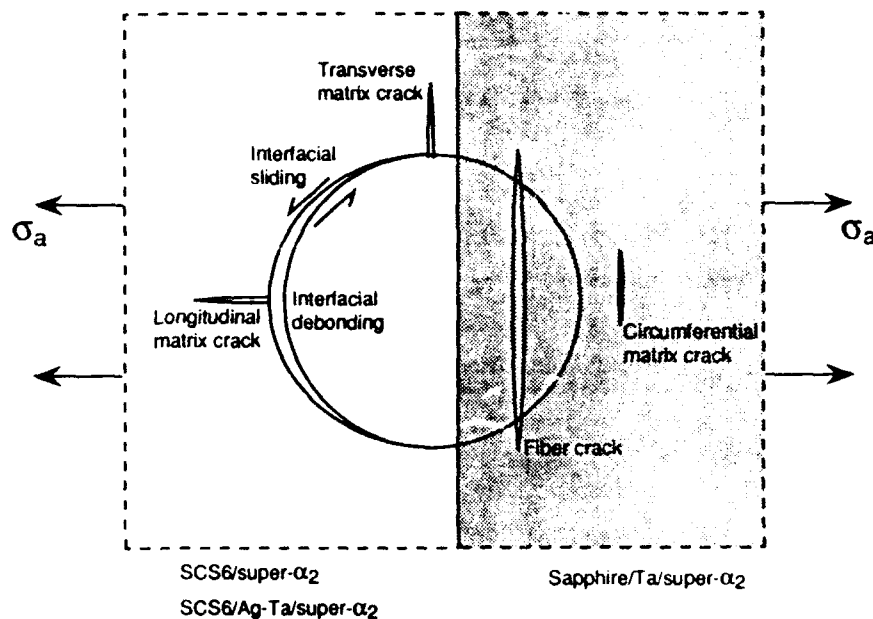


Figure 19 Schematic diagram showing damage mechanisms observed in transverse loading.

of the composites in this study ($E_f \sim 400$ GPa for SiC and sapphire fibers and $E_m = 80$ GPa for the super- α_2 matrix—see Section 3). The largest tensile stress is the radial stress responsible for the circumferential matrix cracking (and the fiber cracking) observed in the sapphire/Ta/super- α_2 composite (Figure 20(a)). Indeed a weak maximum in this stress component occurs at a distance $\sim R/10$ away from the interface in the matrix, coinciding with the observed position of crack initiation. However, crack initiation is also likely to be affected by a variation of material properties with distance from the fiber: the region of matrix around the fiber that is depleted in β phase would be expected to be more brittle than the matrix elsewhere.

Two effects combine to suppress circumferential matrix cracking and instead promote radial matrix cracking in the SCS-6-containing composites. One is the presence of very weak interfacial layers which allow debonding: when debonding occurs the radial stress responsible for circumferential cracking is relieved, leaving the tensile hoop stresses that cause longitudinal and transverse radial cracking. Before debonding occurs, the hoop stress is larger at the location of longitudinal cracking ($\sigma_\theta(0)$) than at the position of transverse cracking ($\sigma_\theta(\pi/2)$), consistent with the observation that longitudinal cracks form first in the SCS-6-containing composites. Debonding causes these relative magnitudes to change ($\sigma_\theta(0)$ decreases and $\sigma_\theta(\pi/2)$ increases) and therefore tends to promote transverse radial cracking, although the changes in the hoop stresses are much smaller than the relaxation of the radial stress. Moreover, the redistribution of hoop stresses occurs gradually during interfacial debonding (because interfacial sliding is restricted by friction¹¹) whereas relaxation of the radial stress responsible for circumferential matrix cracking would be expected to occur as soon as debonding initiates. The other effect that promotes radial cracking in the SCS-6-containing composites is the presence of residual stresses. Since the thermal expansion coefficients of Al_2O_3 and Ti_3Al are similar, residual stresses are expected to be small in the sapphire/Ta/super- α_2 composite. However, in the SCS-6-containing composites the smaller expansion coefficient of SiC causes residual stresses that reduce the radial stress at $\theta = 0$ and increase the hoop tension that is responsible for the observed longitudinal and transverse radial cracking in these composites.

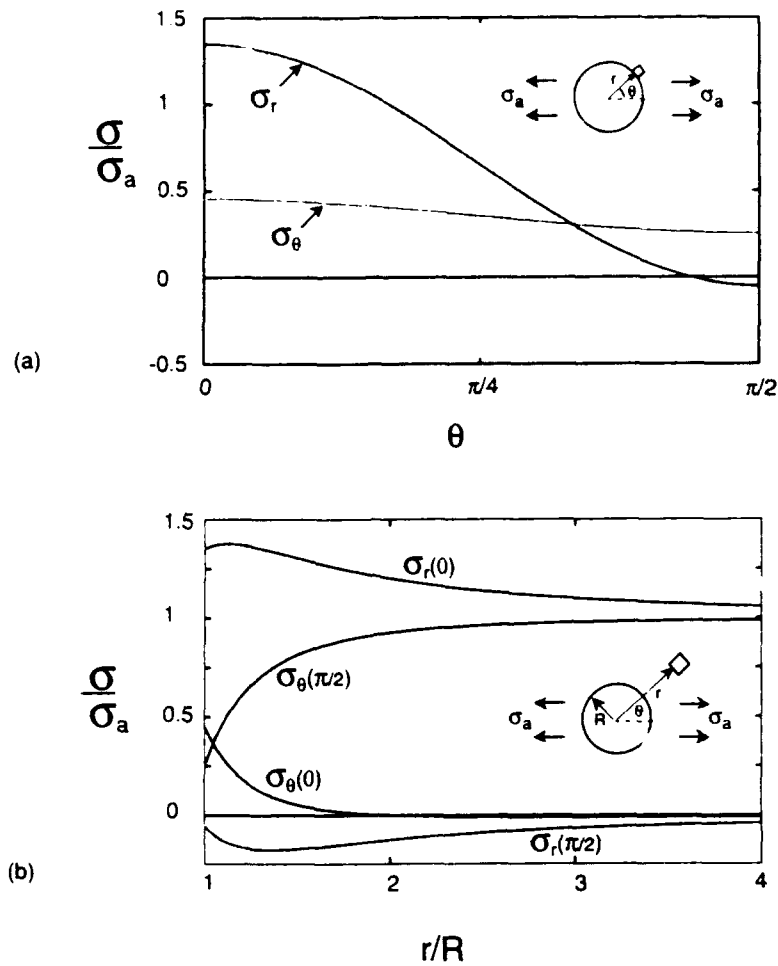


Figure 20 (a) Elastic stresses at interface of strongly bonded isolated fiber subject to transverse loading (ratio of elastic moduli of fiber and matrix = 5). (b) Stresses in matrix adjacent to fiber in (a).

The transverse strength of the sapphire/Ta/super- α_2 composite (300 MPa) was higher than that of the SCS-6/super- α_2 composite (200 MPa), but smaller than that of the SCS-6/Ag-Ta/super- α_2 composite (400 MPa). Therefore the presence of a strongly bonded interface does not guarantee a higher strength than a weakly bonded system. However the potential exists for increasing the strength of the strongly bonded sapphire/Ta/super- α_2 system studied here, for the strength is limited by two effects that could be eliminated. One is damage introduced into the fibers by preparing the transverse cross section. From the calculations in Figure 20, the stress at which cracks formed in the fibers was ~ 450 MPa (700 MPa for a multiple fiber calculation), assuming that residual stresses are negligible. The strengths of undamaged fibers within a composite would be expected to be almost an order of magnitude higher than this. The other strength limiting effect is the presence of a layer of matrix around each fiber that is depleted in β phase and is thus a more brittle site for initiation of circumferential cracks. Presumably this could be avoided by including a barrier layer at the interface to prevent diffusion of oxygen, which is thought to have caused the β -depleted region. Another approach would be to add other β stabilizing elements to the fiber coating, that would diffuse into the surrounding matrix and further inhibit cracking under both monotonic and fatigue loading by locally increasing the ductility in the critical region.

The optimum transverse strength may be achieved with an intermediate mismatch in thermal expansion coefficients of the fibers and matrix. In the absence of residual stress, the maximum tensile stress during transverse loading (for a fully bonded interface and in the absence of plasticity in the matrix) is the radial stress responsible for circumferential cracking of the interface or nearby matrix (Figure 20). As discussed above, the residual stress in a composite with fibers of lower thermal expansion coefficient than that of the matrix would cause the radial stresses to decrease and the hoop stresses to increase uniformly at the interface. Therefore, if transverse failure is dictated by crack initiation at the site of the largest tensile stress, then the optimum residual stress would be that for which the radial stress at $\theta = 0$ and the hoop stress at $\theta = \pi/2$ are equal. More rigorous analysis of this problem, including the effects of plasticity,¹² partial interfacial debonding and sliding, multiple fiber interactions,^{11,13} and modeling of crack initiation would seem to be a fruitful avenue for further defining optimum composite properties.

6.0 REFERENCES

1. D.B. Marshall, B.N. Cox, W.L. Morris and M.C. Shaw, "Mechanical Properties of High Temperature Composites," Proc. 2nd Int. Cong. on Ceramic Science, Orlando, FL (1990).
2. B.N. Cox, M.R. James, D.B. Marshall and R.C. Addison, "Determination of Residual Stresses in Thin Sheet Titanium Aluminide Composites," Met. Trans. **21A**, 2701-07 (1990).
3. B.N. Cox, M.S. Dadkhah, M.R. James, D.B. Marshall, W.L. Morris and M.C. Shaw, "On Determining Temperature Dependent Interfacial Shear Properties and Bulk Residual Stresses in Fibrous Composites," Acta Metall. **38**[2], 2425-33 (1990).
4. C.G. Rhodes, Rockwell Science Center, unpublished work.
5. X.J. Ning and P. Pirouz, "The Microstructure of SCS-6 SiC Fiber," *J. Mat. Res.*, **6**[10], 2234-48 (1991).
6. D.R. Williams, D.L. Davidson and J. Lankford, *Expt. Mech.* **20**, 134-49 (1980).
7. W.L. Morris, M.S. Dadkhah, M.R. James, M.R. Mitchell and S.A. Schroeder, "Micromechanics of Fatigue Crack Growth in Ti-aluminide Composites," p. 511 in *Titanium Aluminide Composites*, Ed. P.R. Smith, S.T. Balsone and T. Nicholas, U.S. Air Force Report WL-TR-91-4020 (1991).
8. D.L. Davidson and J. Lankford, "Fatigue Crack Growth Mechanics for Ti-6Al-4V (RA) in Vacuum and Humid Air," *Met. Trans.* **15A**, 1931-40 (1984).
9. G.T. Gray III and G. Luetjering, "The Effect of Microstructure and Stress Ratio on Fatigue Crack Propagation Behavior of Ti-6Al-4V," p. 2251 in *Titanium Science and Technology*, Ed. G. Luetjering, U. Zuricker, W. Burk, Pub. Deutsche Gesellschaft. fur Metallkunde (1985).
10. Z. Hashin, "Analysis of Properties of Fiber Composites with Anisotropic Constituents," *J. Appl. Mech.* **46**, 543-550 (1979).
11. D. Kouris, "Stress Concentration Due to the Interaction Between Two Imperfectly Bonded Fibers in a Continuous Fiber Composite," *J. Appl. Mech.*, **60**[1], 203-206 (1993).
12. R.P. Nimmer, R.J. Baukert, E.S. Russell, G.A. Smith, and P.K. Wright, "Micromechanical Modeling of Fiber-Matrix Interface Effects in Transversely Loaded SiC/Ti-6-4 Metal Matrix Composites," *ASTM J. Composites Technology and Research*, **13**[1], 3-13 (1991).
13. D. Kouris and E. Tsuchida, "On the Elastic Interaction Between Two Fibers in a Continuous Fiber Composite Under Thermal Loading," *Mechanics of Materials* **12** 131-146 (1991).

APPENDIX A
MEASUREMENT OF INTERFACIAL DEBONDING AND SLIDING
RESISTANCE IN FIBER REINFORCED INTERMETALLICS

Acta. Metall. 40[3], 443-454 (1992)

MEASUREMENT OF INTERFACIAL DEBONDING AND SLIDING RESISTANCE IN FIBER REINFORCED INTERMETALLICS

D. B. MARSHALL, M. C. SHAW and W. L. MORRIS

Rockwell International Science Center, 1049 Camino Dos Rios, Thousand Oaks, CA 91360, U.S.A.

(Received 30 April 1991)

Abstract—A technique is described for measuring fiber debonding and sliding characteristics in intermetallic matrix composites. The method involves pulling a single fiber that protrudes from the composite, while measuring the applied force and relative displacements of the fiber and matrix. High resolution displacement mapping methods are used to obtain data during initial loading, where sliding progresses only partly along the fiber. Measurements from a $\text{Ti}_3\text{Al}/\text{SiC}$ composite are interpreted using the analysis of the companion paper. The results indicate a strong effect of constraint on the sliding response and provide quantitative measurements of sliding resistance, residual stresses, and debond energy. Preliminary measurements of changes in sliding resistance with cyclic loading are presented.

Résumé—On décrit une technique pour mesurer la décohésion des fibres et leur glissement dans des composites à matrice intermétallique. Cette méthode consiste à tirer une seule fibre sort du composite, pendant que l'on mesure la force appliquée et les déplacements relatifs de la fibre et de la matrice. On utilise les méthodes de représentation à haute résolution des déplacements pour obtenir des résultats en début de charge, quand le glissement ne se propage qu'en partie le long de la fibre. On interprète, à partir de l'analyse de l'article précédent, les mesures effectuées sur un composite $\text{Ti}_3\text{Al}/\text{SiC}$. Les résultats montrent que la contrainte a une forte influence sur la réponse en glissement et fournissent des mesures quantitatives de la résistance au glissement, des contraintes résiduelles et de l'énergie de décohésion. On présente aussi des mesures préliminaires de variations de la résistance au glissement avec une charge cyclique.

Zusammenfassung—Ein Verfahren zur Messung der Charakteristika des Ablösens und des Gleitens von Fasern in Verbundwerkstoffen mit intermetallischer Matrix wird beschrieben. Dieses umfaßt das Herausziehen einer einzelnen Faser aus dem Verbundwerkstoff, wobei die angelegte Kraft und die relative Verschiebung zwischen Faser und Matrix gemessen werden. Mittels hochgenauer Aufzeichnung der Verschiebung werden Daten zur anfänglichen Belastung, bei der Gleitung nur teilweise entlang der Faser abläuft, ermittelt. Messungen an dem Verbund $\text{Ti}_3\text{Al}/\text{SiC}$ werden mit der in der begleitenden Arbeit beschriebenen Analyse ausgewertet. Die Ergebnisse weisen auf einen starken Einfluß von Einschränkungen des Gleitverhaltens hin und ergeben quantitative Messungen von Gleitwiderstand, Restspannungen und Ablöseenergie. Vorläufige Messungen von Änderungen im Gleitwiderstand in Abhängigkeit von der zyklischen Belastung werden vorgelegt.

1. INTRODUCTION

There is now convincing evidence that some degree of weakness in the interfacial region between the fibers and matrix of intermetallic composites is essential for the reinforcing fibers to be effective in improving the properties of the composite [1-4]. Such evidence comes from observations during both fatigue and monotonic loading of $\text{Ti}_3\text{Al}/\text{SiC}$ composites. Therefore, experimental methods are needed for measuring the mechanical properties of interfaces in these composites, both as a basis for reliability analysis and as a means of evaluating and understanding processing changes aimed at optimizing interfacial properties. In this paper we describe a technique, based on pulling single fibers out of the composite, which can provide quantitative measurements of the interfacial sliding resistance, interfacial debond energy, and residual stresses that exist as a result of mismatch in fiber and matrix properties.

The technique is related to fiber pushing experiments that have been used to measure interfacial properties in ceramic composites [5-9]. In their simplest form, the pushing experiments involve loading an indenter on the polished end of a fiber within a thin slice of composite and measuring the force needed to cause complete sliding of the fiber through the slice [10-16]. Such experiments have also been used successfully to measure interfacial sliding in $\text{Ti}_3\text{Al}/\text{SiC}$ composites [17, 18]. However, the results of this type of experiment, involving a thin slice of composite, are difficult to interpret in terms of fundamental interfacial properties (debond energy and frictional sliding parameters), because of the complications of end effects and residual stresses, and because, in the absence of independent observations, it is not generally known whether the onset of complete sliding coincides with the initiation of debonding or follows progressive debonding and sliding along the interface. Other studies with ceramic

composites have shown that much more information can be extracted from experiments in which individual fibers in a thick specimen are pushed, and the applied forces and relative displacements of the fibers and matrix are measured continuously as the sliding progresses *partially* along the fiber [5-8]. These experiments require very sensitive displacement measurements, since the displacements result from elastic strains within the sliding portion of the fiber. Displacement sensitivity of several nm was achieved by using an ultra low load indenter to push on the fibers [5-8]. The fiber pulling technique described in this paper is the tensile loading counterpart of this continuous indentation experiment, the requisite sensitivity in displacement measurements being achieved by direct imaging of the fiber and matrix.

Calculation of interfacial properties and residual stresses from these measurements requires the fitting of theoretical predictions derived from micromechanics modeling of the debonding and sliding process to the experimental data. An abundance of such models, with various degrees of approximation, have appeared in the literature recently, following the widespread use of the fiber pushing experiments. For the types of composites of interest here, with weakly bonded (or unbonded) interfaces and low sliding resistance, shear-lag models are appropriate. A recent shear lag analysis by Hutchinson and Jensen [19] accounts for effects of thermal and elastic mismatch of the fibers and matrix as well as interfacial debonding, with sliding over the debonded surfaces governed either by a Coulomb friction law or by a constant sliding stress. This analysis has been cast in a form that is convenient for comparison with the fiber pulling experiments in the accompanying paper [20].

2. EXPERIMENTAL

2.1. Material

A titanium-aluminide/SiC composite, in the form of a thin sheet (0.7 mm thickness) containing three layers of uniaxially aligned fibers,[†] was used for the interfacial sliding measurements. The composition of the α_2 -based matrix was Ti-25Al-10Nb-3Mo-1V (super- α_2). The fibers were CVD SiC of diameter 140 μm , with several carbon-rich outer layers (SCS-6) that provide a weakly bonded sheath on the outside of the fibers [21]. Studies of the microstructure, mechanical properties, and residual stresses in the composite have been published elsewhere [1, 2, 4, 22, 23]. Some reaction between the outer layers of the fiber and the matrix occurred during consolidation, forming a layer of fine-grained silicides and carbides $\sim 2 \mu\text{m}$ thickness around each fiber [23]. Pertinent mechanical properties of the composite are listed in Table 1.

[†]Composite manufactured by Textron Specialty Materials, Waltham, Mass.: super- α_2 Ti/Al matrix with SCS-6 SiC fibers.

Table 1. Properties of Ti/Al SiC composite

Young's modulus of matrix, E_m	80 GPa
Young's modulus of fiber, E_f	414 GPa
Poisson's ratio of matrix, ν_m	0.3
Poisson's ratio of fiber, ν_f	0.3
Volume fraction of fibers, f	0.36
Fiber radius, R_f	70 μm

Residual stresses strongly affect the fiber pulling experiments. Several techniques, described in detail elsewhere, have been used to measure residual stresses in this composite [22]. The axial residual stress in the fibers was found by masking the ends of a rectangular beam and etching away all of the matrix within a long midsection (56 mm length), to leave the two ends joined by bare fibers. The change in length caused by relaxation of residual stress in the fibers was measured by taking optical micrographs of both ends against a fixed reference gage before and after the matrix was removed. The residual strain thus measured was $1.56(\pm 0.02) \times 10^{-3}$, which corresponds (according to a concentric cylinder calculation) to a compressive axial stress of 800 ± 20 MPa in the fiber. The axial residual stress in the matrix was found by analysis of X-ray diffraction peak shifts to be 450 ± 50 MPa. With the measured volume fraction of fibers ($f = 0.36$) these two values satisfy the condition for force balance on a cross section of the composite.

2.2. Sliding measurements

The single fiber pulling experiment is shown schematically in Fig. 1. The ends of the specimen in Fig. 1(a) were glued to a loading fixture on the stage of an optical microscope. As the ends of the specimen were pulled apart, with the force being measured continuously by a load cell, high magnification micrographs were obtained from the region where the fiber exited the matrix as in Fig. 1(b). From these micrographs accurate measurements of the distance that the fiber pulled out of the matrix were obtained.

The specimens were prepared from beams ($\sim 40 \text{ mm} \times 3 \text{ mm} \times 0.7 \text{ mm}$) of the composite which contained fibers aligned uniaxially along the beams. The matrix and all but one of the fibers were removed from the central section ($\sim 4 \text{ mm}$ length) of the beam by a combination of diamond cutting and chemical etching. First, most of the material within the central section was removed by grinding, leaving several fibers and the surrounding matrix. Then, the remaining matrix was removed by etching, while protecting the ends with a mask. The fibers that were not to be tested were then individually removed by cutting with a diamond saw operated under a microscope. A saw cut was also made through the top layer of fibers at a predetermined distance from the central section (1.5 mm in the present experiments), in order to allow data to be collected during complete sliding of the fiber [Fig. 1(c)], as well as from the initial loading region where partial sliding occurred [Fig. 1(b)].

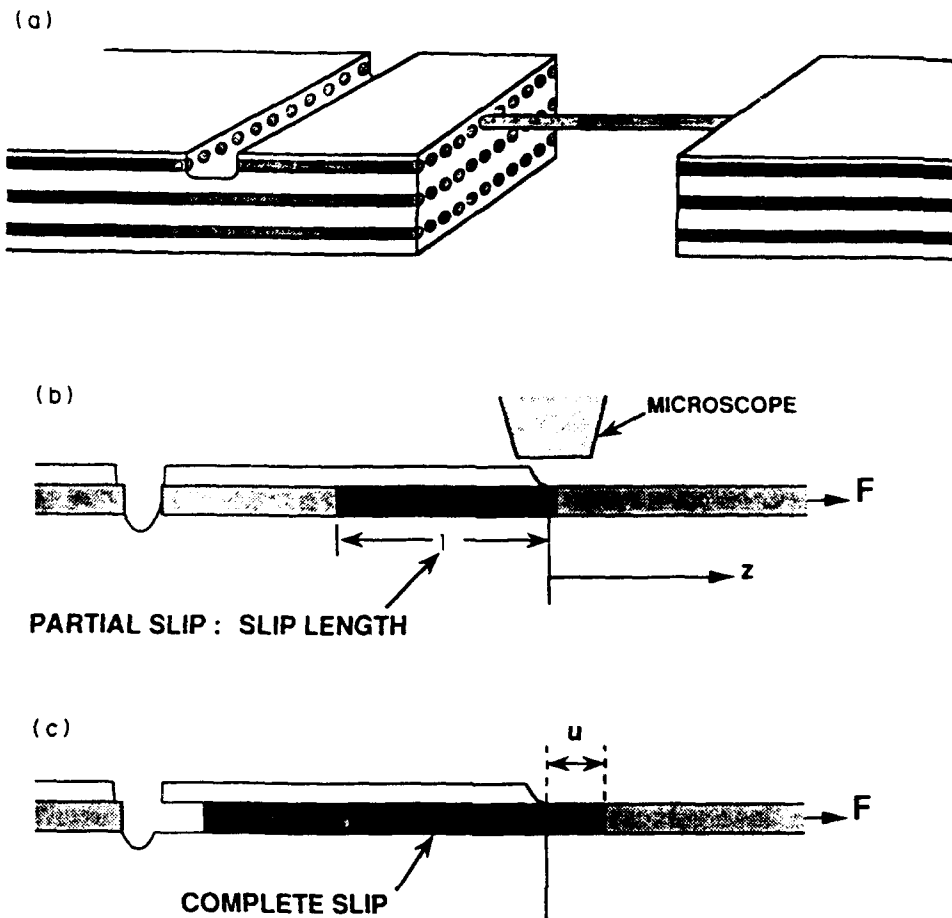


Fig. 1. Schematic diagram of fiber pulling experiment. (a) Test specimen; (b) Initial loading where sliding occurs partially along the embedded length of fiber; (c) Pullout where entire embedded length of fiber slides.

The relative displacements of the fiber and matrix were found by measuring changes in separation of corresponding image features (from the matrix and fibers) in pairs of micrographs, one obtained before load was applied to the specimen and the other during loading. For the data reported here, this differential measurement was obtained by stereo viewing of pairs of micrographs [24], although the measurement can also be done by computerized digital image correlation [25]. Both methods yield *relative* displacement resolution of ~ 10 nm from optical micrographs (substantially smaller than the point-to-point resolution of the individual micrographs), provided the imaging conditions for both micrographs are identical (illumination and collection optics, focus, specimen orientation and position).

Typical micrographs, taken at three stages of the experiment, are shown in Fig. 2. The surface of the fiber is in focus along a line at the top of the fiber. As a result of the etching, the surface of the matrix from which the fiber protruded was at an angle of approximately 50° to the plane of the micrographs, so that the matrix is in focus only along a line perpendicular to the fiber. The image features along this line

were compared with those along the top of the fiber to obtain the displacement measurements. The micrograph of Fig. 2(a) was obtained before loading. Fig. 2(b) during initial loading (just before sliding reached the saw cut, relative displacement $\approx 9.8 \mu\text{m}$), and Fig. 2(c) immediately after complete sliding had begun (relative displacement $39 \mu\text{m}$).

Measurements were obtained during both monotonic and cyclic loading experiments. All measurements required the load to be held constant during exposure of the micrographs. The "monotonic" loading experiments included a single unload/reload cycle during the initial loading phase, where only partial sliding occurred, in order to provide additional data that is useful for distinguishing effects of residual stresses. This single cycle did not significantly affect the remainder of the force-displacement relation. Multiple cyclic loading experiments were done (on another specimen) at various stages of pullout as a preliminary investigation of fatigue of the interfacial properties. Within the initial loading region, the load was cycled repeatedly between a fixed maximum value and zero. Cycling in the pullout region involved reversing the load so as to push the fiber and cause



Fig. 2. Examples of optical micrographs from which measurements were obtained. (a) Zero load; (b) during initial loading (partial slip), load 50 N; (c) after complete sliding began, load 34 N.

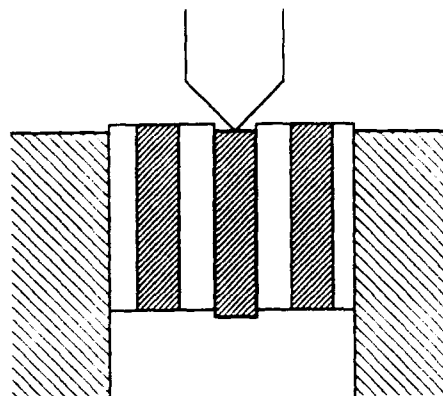


Fig. 3. Schematic diagram of fiber pushout test.

complete sliding in the opposite direction for a distance of 100 μm , then pulling it back to the original position.

2.3. Comparison with fiber pushing experiments

Some simple fiber pushout measurements were done in order to provide a comparison with the fiber pulling results. In these experiments a thin polished slice of the composite (with fibers oriented normal to the slice) was glued into a fixture as shown in Fig. 3, and the ends of the fibers were pushed using a Vickers indenter. The specimen mounting method illustrated in Fig. 3 avoids extraneous bending stresses that might arise if the specimen was simply supported on a base plate containing a hole. The indentation load was measured continuously using a load cell, although in these experiments the displacement was not measured.

3. RESULTS

The relative displacements of the fiber and matrix at various stages of a fiber pulling experiment are shown in Fig. 4. The data to the left of the peak in Fig. 4(a) correspond to initial loading, where sliding between fiber and matrix occurs only over a limited distance along the fiber, whereas data to the right of the peak correspond to complete sliding of the entire

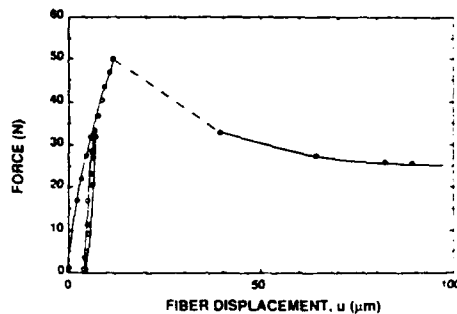


Fig. 4. Force and displacement measurements from fiber pulling experiment. $\text{Ti}_3\text{Al-SiC}$ composite with embedded fiber length 1.5 mm.

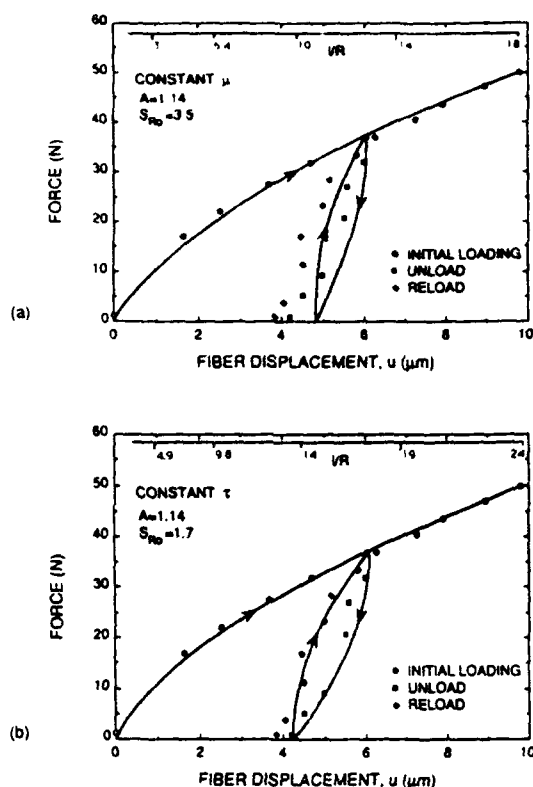


Fig. 5. Data from initial loading region of Fig. 4. Continuous curves for initial loading are best fit of equation (1) in (a) and equation (2) in (b), both with $\Gamma' = 0$. Curves for unload/reload cycles predicted from equations (3) to (6) using values of S_{R0} and δ^* or δ calibrated from curve fit to initial loading.

embedded length of fiber (1.5 mm). The initial loading included a single unload/reload cycle between loads of 37 N (corresponding to an axial stress of 2.4 GPa on the end of the fiber) and zero; the data from the initial loading region are shown with an expanded displacement scale in Fig. 5 (the curves in this figure are fitted according to two interface models discussed in Section 4). The partial recovery of the displacement during the unloading half-cycle (approx. 30%) and the hysteresis between unloading and reloading are characteristic of frictional sliding between the matrix and fiber. After reloading to 37 N the displacement was almost the same as before unloading, indicating that the sliding resistance of the interface had not degraded significantly during the unload/reload cycle.

When, during continued loading, the sliding distance reached the end of the fiber (at a load of 50 N, corresponding to stress 3.25 GPa in the fiber) the transition to complete sliding was accompanied by a discontinuous load drop and increase in displacement. Subsequent pullout involved stick-slip motion, with amplitude initially ~ 1 N (smaller than the symbols in Fig. 4), but decaying to < 0.1 N after 200 μm of movement. The displacements during the entire pullout phase are shown in Fig. 6. After approxi-

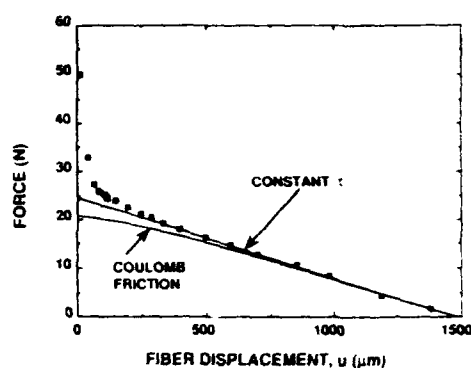


Fig. 6. Data from pullout region of Fig. 4 with predicted curves for constant friction and Coulomb friction models.

mately 200 μm of the fiber had pulled out, the load decreased linearly with pullout distance, corresponding to a constant frictional sliding resistance.

Examination by scanning electron microscopy of both the fiber after it was pulled completely out of the matrix and the remaining hole after sectioning indicated that separation occurred between the outer (SCS-6) coating of the fiber and the reaction layer that existed between the fiber and matrix (Fig. 7). This was confirmed by EDAX analysis of the fiber surface: within the region that was exposed by the etchant there were traces of Al, Ti, Mo and Nb remaining from the matrix and/or reaction layer, whereas over the surface that was exposed by sliding there was no sign of these elements (the only signal detected being Si from the fiber). These results also provide good evidence that the interface was not preferentially attacked by the etchant during specimen preparation. Over most of the sliding surface there was no apparent damage to the outer coating of the fiber, although near the end of the fiber the coating was cracked.

Results of a cyclic loading experiment are shown in Fig. 8. Cycling the load between 20 N and zero 150 times [Fig. 8(a)] during the initial loading phase (partial slip) had only a minor effect on the sliding resistance; the displacement during subsequent loading above 20 N was increased slightly ($\approx 10\%$). At the peak load of 28 N the entire fiber began sliding: this load is lower than that in Fig. 4 because in this specimen the embedded length was smaller (0.78 mm). The fiber was pulled out 170 μm , then the load was reversed until the entire fiber moved in the opposite direction for a distance of 100 μm , then the load was reversed again to pull the fiber back out to 170 μm . This cycle was repeated 20 times [Fig. 8(b)]. During each load reversal there were small displacements [~ 2 μm , see inset of Fig. 8(b)] corresponding to the progression of reverse slip partly along the interface. After 20 cycles, the force needed to make the entire fiber move had decreased by $\sim 25\%$ as shown in Fig. 8(c).

Examination of the fiber surface after pulling the fiber completely out of the matrix indicated that separation had taken place between the outer coating



Fig. 7. Scanning electron micrographs showing fiber from experiment of Fig. 4 after being pulled out of the matrix.

of the fiber and the reaction product layer in the matrix, as in monotonic loading. However, the SCS-6 layers on the fiber were severely cracked (Fig. 9). It is not known whether the cracking occurred while the fiber was within the matrix, or whether it was caused by relief of residual stresses (built up by deformation occurring during the repeated sliding) after removing the fiber.

In the fiber pushing experiments the applied load was increased continuously until complete sliding of the fiber began, whereupon the load decreased abruptly. From 10 tests in the slice of thickness 0.75 mm, the peak load was 47 ± 7 N. In most cases sliding occurred at the same location as in the pulling experiments (i.e. between the outer layer of the fiber and the reaction product layer in the matrix (Fig. 10).

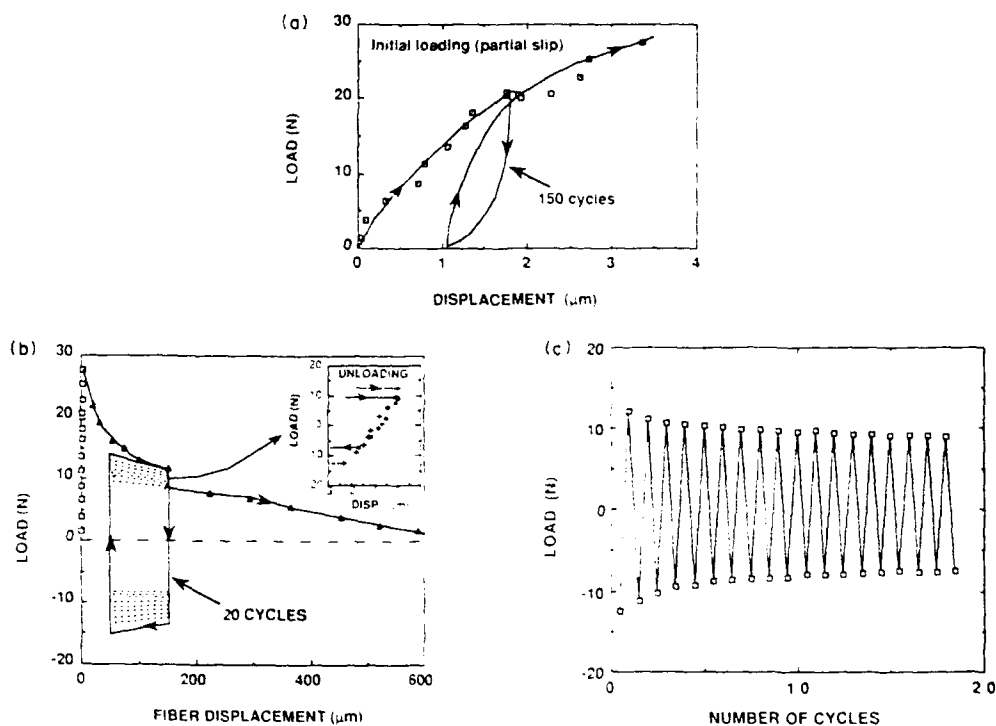


Fig. 8. Force-displacement measurements during cyclic loading: (a) load cycled between 20 N and zero during initial loading; (b) load cycled in tension-compression so as to cause sliding of the entire embedded length of fiber back and forth; (c) variation of load needed in (b) to cause complete sliding with number of cycles.



Fig. 9. Scanning electron micrograph of fiber from experiment of Fig. 8 after pullout from matrix.



Fig. 10. Scanning electron micrograph of fiber after indentation pushout.

although for several fibers sliding occurred between the fiber and the SC S-6 layers.

4. ANALYSIS OF RESULTS

4.1. Initial loading (partial sliding)

Expressions relating the applied forces and sliding displacements appropriate to the initial loading data are derived in the accompanying paper [20]. The analysis is based on the model of Hutchinson and Jensen [19], which considers pullout by stable interfacial debonding, with sliding over the debonded surface governed by either a Coulomb friction law or

a constant sliding resistance. The composite is treated as a composite cylinder with shear lag conditions, but full account is taken of effects of residual axial and transverse stresses, Poisson's strains, differing elastic properties of the fibers and matrix, and anisotropy of both the elastic properties of the fibers and the elastic mismatch strain. The analysis requires that the length, L , of the debond be more than 2–3 times the fiber radius and that the interfacial sliding resistance be small compared with the applied axial stress in the fiber. The displacements, δ , during initial loading can be expressed most conveniently as follows, in terms of normalized parameters defined in Table 2.

Table 2. Definitions of parameters in equations (1)–(6).

σ_f	Applied stress in fiber
σ_{f0}	Peak value of σ_f
σ_r	Residual axial stress in fiber
τ	Interfacial sliding resistance for constant friction model
μ	Friction coefficient for Coulomb friction model
G	Mode II fracture energy at debond tip
	Difference in axial fiber stress immediately behind and far ahead of the debond tip
S_0	τ_0/σ_{f0}
γ_0	$\frac{\sigma_{f0} - \sigma_r}{\sigma_{f0} + (1 - \mu)\sigma_{f0}}$
L	$\frac{L}{R} \frac{\sigma_{f0} + \sigma_r}{\tau_0 + \sigma_r}$
β	$\frac{4E_m G}{(1 - \mu)R\sigma_{f0}}$
Λ	$\left\{ \frac{1 - (1 - \mu)^2}{4\mu} \right\}$
γ^*	$\frac{\sigma_r R}{2\sigma_{f0} L}$
δ	$\frac{\sigma_r R}{4\sigma_{f0} L}$

Equations evaluated from Ref. [20] with $\nu = 0$ for single fiber pulling wherever it appears explicitly in the equations of Ref. [20] and for evaluation of β parameters, but with ν equal to the actual volume fraction of fibers in the composite for evaluation of the parameters L and γ_0 . Parameters μ and τ are dimensionless functions of elastic properties and anisotropy of the mismatch strain defined in Hutchinson and Jensen [19].

$$\delta \cdot \delta^* = -AS_{R0} \ln \left[\frac{S_{R0} - S_a}{S_{R0} - \Gamma'} \right] + \Gamma' - S_a \quad (\Gamma' > 0) \quad (1)$$

for Coulomb friction at the sliding interface, and

$$\frac{\delta}{\delta'} = S_a^2 + 2S_a S_{R0}(A - 1) - \Gamma'^2 - 2\Gamma' S_{R0}(A - 1) \quad (\Gamma' > 0) \quad (2)$$

for interfacial sliding governed by a constant sliding resistance τ .

The normalized parameters S_a , S_{R0} and Γ' represent the applied load, the residual stress, and the debond energy; δ^* and δ' are displacement scaling parameters which are dependent on the interfacial sliding properties; and A is a dimensionless parameter that is dependent upon the elastic properties and thermal anisotropy of the fibers and matrix. Debonding of the interface initiates at the normalized applied load $S_a = \Gamma'$. Therefore equations (1) and (2) require that S_a be larger than Γ' . If Γ' is negative, spontaneous debonding and sliding between the fiber and matrix occurs during sectioning of the composite (note, from Table 2, that since Γ' is the sum of two terms, one proportional to the debond energy and the other the residual stress, the condition $\Gamma' = 0$ corresponds to finite debond energy). In that case the displacements are given by equations (1) and (2) with $\Gamma' = 0$ (i.e. the displacements are independent of the debond energy). The equations are also restricted to applied loads $S_a < S_{R0}$; if $S_a > S_{R0}$ the normal stress at the interface becomes tensile.

The changes in displacement during unloading and reloading are given, for the Coulomb friction model, by

$$\frac{\delta_p - \delta}{\delta^*} = (S_{R0} - S_a) \times \left[1 - \sqrt{\frac{S_{R0} - 1}{S_{R0} - S_a}} \right] \quad (\text{unloading}) \quad (3)$$

and

$$\frac{\delta - \delta_0}{\delta'} = (S_{R0} - S_a) \times \left[1 - \sqrt{\frac{S_{R0}}{S_{R0} - S_a}} \right] \quad (\text{reloading}) \quad (4)$$

where δ_p is the displacement at the peak load, given by equation (1) with $S_a = 1$, and δ_0 is the displacement after unloading, given by equation (3) with $S_a = 0$. The corresponding displacements for the constant friction model are

$$\frac{\delta_p - \delta}{\delta'} = \frac{1}{2}(1 - S_a)^2 \quad (\text{unloading}) \quad (5)$$

and

$$\frac{\delta - \delta_0}{\delta'} = \frac{1}{2}S_a^2 \quad (\text{reloading}) \quad (6)$$

Data from the fiber pulling experiments indicate that the parameter Γ' is close to, or less than zero. Relative sliding between the fibers and matrix has been observed at applied loads as low as 3 N, a detection limit which is imposed by the accuracy of the displacement measurements. With this limit on the stress, σ_a , needed to initiate debonding, the equations of Table 2 provide an upper bound for the intrinsic debond energy of the interface, G_c :

$$G_c \leq \frac{(\sigma_a - \sigma_{f0})^2 b_2 R_f}{4E_m} \quad (7)$$

With the values of σ_{f0} , E_m , R_f , and b_2 from Tables 1 and 3, and $\sigma_a < 200$ MPa (corresponding to 3 N load), this upper bound becomes 41 J/m². Although the use of this equation with data corresponding to small loads (and hence small sliding distances) is questionable, the conclusion (that $\Gamma' \leq 0$) is also consistent with analysis of the data at higher loads where the sliding distances are large enough to satisfy the requirements of the shear lag models. In this case, we will see that unless $\Gamma' \approx 0$ neither analysis can be fitted to the data using parameters consistent with independent measurements. For $\Gamma' \leq 0$ (i.e. $\sigma_a = 0$), the upper-bound debond energy is reduced to 26 J/m².

The data from Fig. 5 were analyzed in terms of the two models by first fitting equations (1) and (2), with $\Gamma' = 0$, to the data for initial loading, within the load range zero to 50 N, excluding the data from the unload/reload cycle. The value of A was calculated from the elastic properties listed in Tables 1 and 3, assuming initially that both the elastic misfit strain and the elastic properties of the fibers are isotropic. These assumptions are uncertain because direct measurements of transverse properties of the fibers do not exist and because plastic yielding of the matrix during cooling from the fabrication temperature could have introduced anisotropy in the elastic misfit strain. The influence of strain anisotropy, characterized by the parameter $\lambda = \epsilon_r^T / \epsilon_z^T$, where ϵ_r^T and ϵ_z^T are the misfit strains in the radial and axial directions, will be examined below. The values of δ^* and δ' were adjusted, for various values of S_{R0} , to fit the measured displacement at the peak load ($S_a = 1$), and the values of S_{R0} that gave the best fits to the remainder of the data were selected (Fig. 11). These values of S_{R0} and δ^* or δ' are listed in Table 4, along with the corresponding values of the residual stress, σ_{f0} , and

Table 3. Dimensionless elastic parameters⁽¹⁾ (assuming isotropic fibers)

a_2	1.64
a_4	0.536
b_1	0.400
b_2	0.188
$A = \left(1 - \frac{a_2 b_1}{a_4}\right)^{-1}$	1.14

⁽¹⁾ Evaluated from Ref. [19], with the elastic properties listed in Table 1 and $\lambda = 1$

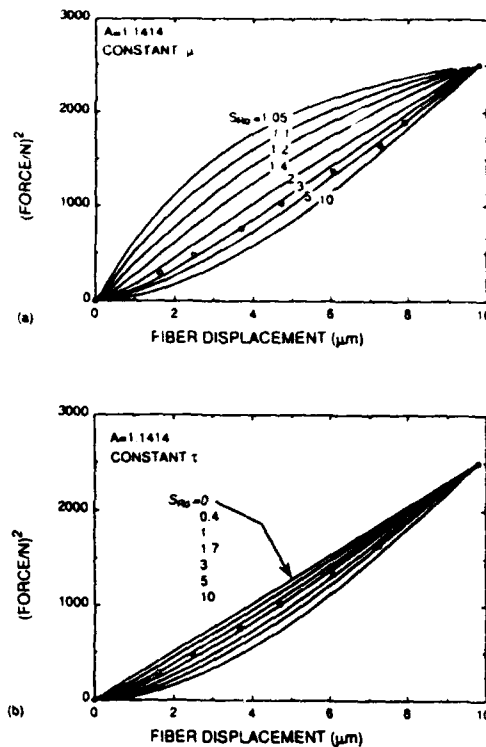


Fig. 11. Comparisons of equations (1) and (2) with data from Fig. 5. (a) Coulomb friction model [equation (1)] for various values of S_{R0} with δ^* obtained by fitting to measured peak load and displacement; (b) constant friction model [equation (2)] with δ' obtained by fitting to measured peak load and displacement.

frictional property (μ for the Coulomb model and τ for the constant friction model) calculated from these fitted parameters using the equations of Table 2.

The fitted values of δ^* , δ' and S_{R0} were then used to generate *predicted* curves for the unload/reload cycle, using equations (3)–(6). These predicted curves and the fitted initial loading curves are compared with the data in Fig. 5. The initial loading curves for both models show reasonable agreement with the data (perhaps slightly better for the constant friction model), a result that is not surprising since there are two adjustable parameters for each. However, the *predicted* unload/reload curves for the Coulomb fric-

tion model show significant discrepancy with the data, whereas those for the constant friction model show good agreement.

Failure of the Coulomb friction model is also evident in the value of residual axial stress in the fiber that was evaluated from the curve fit to the initial loading data (Table 4), this value was $\sigma_{f0} = -1600$ MPa, which is double the value measured independently (-800 MPa, Section 2). This discrepancy is much larger than experimental errors. On the other hand, the value obtained from the constant frictional stress model, $\sigma_{f0} = -780$ MPa, was in agreement with the independent measurement.

To check whether anisotropy of the misfit strain would have a significant effect on the comparison of the Coulomb model with the data, the curve fitting was repeated for various values of $\lambda = \epsilon_1^T/\epsilon_2^T$. The anisotropy enters the analysis via the influence of λ on the parameters a_2 and a_4 , which affect the parameter A (and hence S_{R0}) in equations (1), (3) and (4). Note that, for a given residual axial stress σ_{f0} in the fibers, λ does not affect the curves for the constant friction model, since the only appearance of A and S_{R0} in equations (2), (5) and (6) is in the term $S_{R0}(A - 1)$ in equation (2), which can be written as $\sigma_{f0} \sigma_p$ (Table 1). The curves from the Coulomb friction model with $\lambda = 4$ that best fit the initial loading data are shown, along with the predicted unload/reload curves, in Fig. 12(a); the corresponding values of σ_{f0} and the other parameters are listed in Table 4 for $\lambda = 2, 4$ and 10. Both the predicted unload/reload curves and the calibrated values of σ_{f0} agree more closely with the data and independent residual stress measurement as the value of λ increases. This trend is to be expected, since with increasing λ the normal interfacial residual stress becomes larger for a given residual axial stress in the fiber. Consequently the *relative* changes in normal interfacial stress over the region of sliding become smaller (the *absolute* change in normal stress is determined by the stress applied to the end of the fiber), resulting in a smaller relative change in interfacial sliding resistance. For the case of $\lambda = 10$, the normal interfacial stress at the peak applied load of 50 N would vary between 1050 MPa at the end of the sliding region to 918 MPa at the surface where the fiber exits the matrix, with corresponding frictional

Table 4. Parameters evaluated by curve fitting to initial loading data

	$\Gamma = 0$				$\Gamma = 0.1$
	$\lambda = 1$	$\lambda = 2$	$\lambda = 4$	$\lambda = 10$	$\lambda = 1$
Coulomb model					
A	1.14	1.087	1.057	1.038	1.14
δ^*	28	45	66	89	38
S_{R0}	3.5	5	6.5	8	5
μ	0.23	0.14	0.10	0.074	0.17
σ_{f0} (MPa)	-1600	-1400	-1200	-990	-2300
Constant friction model					
A	1.14				1.14
δ' (μm)	6.6				5.5
S_{R0}	1.7				3
τ (MPa)	66				78
σ_{f0} (MPa)	-780				-1380

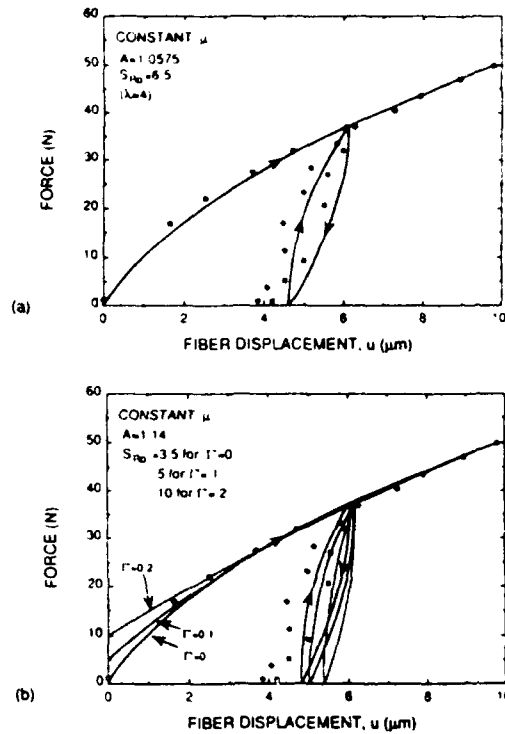


Fig. 12. Effect of (a) anisotropy in misfit strain ($\lambda = \epsilon_1^T / \epsilon_2^T$) and (b) positive values of Γ' on curve fitting with Coulomb friction model. Data from Fig. 5.

stresses of 77 and 67 MPa. Therefore the response is indeed close to that of a constant frictional stress. However, such a large anisotropy in misfit strain is not likely to be realistic, suggesting that another physical phenomenon must be responsible for the constant friction behavior.

To confirm the validity of using $\Gamma' \leq 0$ in the analysis, the curve fitting was repeated with several positive values of Γ' . The curves corresponding to debond initiation loads of 5 and 10 N ($\Gamma' = 0.1$ and 0.2) for the Coulomb friction model are shown in Fig. 12(b), and corresponding values of σ_{R0}^* and the other parameters are listed in Table 4. Both of the discrepancies noted above, in the degree of recovery during unloading and in the magnitude of the residual axial stress in the fiber, become larger as the value of Γ' is increased. A similar trend is evident for positive values of Γ' for the constant friction model (Table 4). Therefore, the constant friction model with $\Gamma' \leq 0$ is the only combination that is consistent with the measurements.

As a final check that the sliding conditions satisfy the assumptions of the analysis, the debond lengths, l , were evaluated at various stages of loading, using the calibrated parameters from Table 4 and the following expressions [20]

$$l R_l = - \left(\frac{1}{2\mu} \right) \ln \left[\frac{S_l - S_{R0}}{\Gamma' - S_{R0}} \right] \quad (8)$$

for Coulomb friction, and

$$l R_l = \left(\frac{\sigma_c^2}{2\tau} \right) [S_l - \Gamma'] \quad (9)$$

for the constant friction model. The results are indicated by the upper scales in Fig. 5(a) and (b). For both models, the calculated slip lengths satisfy the condition $l R > 2$ (a requirement of the debond analysis of Ref. [19]) over the entire range of data. Moreover, the corresponding applied loads satisfy the shear-lag requirement $\sigma_s \gg \tau$.

4.2. Pullout (sliding over entire embedded length of fiber)

A constant interfacial sliding resistance would result in a linear decrease in the applied force with pullout distance, when sliding occurs over the entire embedded length of fiber. At pullout distances larger than $200 \mu\text{m}$ this is the case for the data in Fig. 6. However, at smaller pullout distances the forces are larger than the extrapolation from the linear region, a trend that is contrary to the response that would result from Coulomb friction, for which the force would fall below the linear extrapolation [26]. The results indicate that the magnitude of the average sliding resistance along the embedded length of fiber decreased as the fiber was pulled out for the first $200 \mu\text{m}$, from an initial value of $\sim 66 \text{ MPa}$ to a steady state value of $\sim 40 \text{ MPa}$ (Fig. 13).

4.3. Pushout

The force required to cause complete sliding in the fiber pushout experiments ($47 \pm 7 \text{ N}$) was substantially larger than in fiber pulling experiments with fibers of similar embedded length [Fig. 8(b), peak force 27 N]. Such a difference is expected in the presence of residual axial compressive stress in the fiber and a finite debond energy [20]. For a given embedded length, the critical applied stresses in pulling (σ_p^*) and pushing (σ_s^*) are related approximately by (for $\Gamma' \leq 0$) [20]

$$|\sigma_s^*| - |\sigma_p^*| \approx 2|\tau|. \quad (10)$$

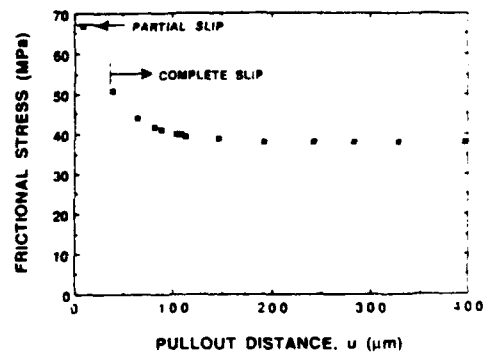


Fig. 13. Average frictional stress during fiber pullout, calculated from data of Fig. 6.

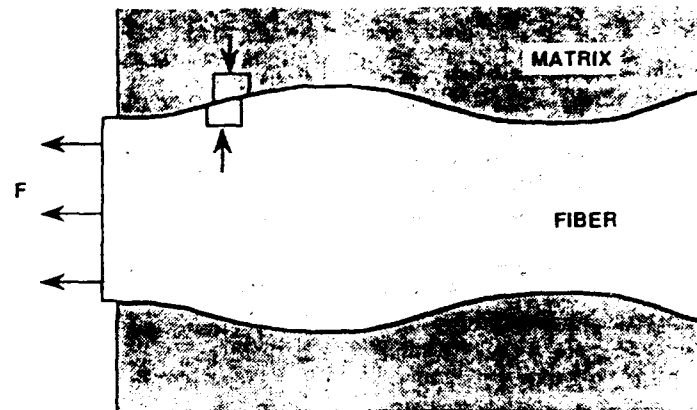


Fig. 14. Increased radial misfit strain due to surface roughness in constrained fiber sliding

With the measured difference in forces required for complete initial sliding in the pulling and pushing experiments, equation (10) gives γ in the range 360–800 MPa. The upper end of this range is equal to the measured magnitude of σ_{m} , and therefore corresponds to $\Gamma' = 0$ and $G_c = 26 \text{ J m}^{-2}$, whereas the lower end corresponds to $G_c = 5 \text{ J m}^{-2}$.

5. DISCUSSION

Analysis of the experimental data from the region of initial loading indicated that the resistance to sliding between the fiber and matrix was constant (within $<10\%$) along the debonded region of the interface. The results differ significantly from the response predicted from a smooth fiber–matrix interface with sliding governed by a Coulomb friction law; the observed behavior could result from such an interface only if the anisotropy in the elastic misfit strain between the fiber and matrix is unreasonably large (more than a factor of 10), so that changes in normal stress due to Poisson's contraction along the region of sliding are small compared with the initial residual stress.

Recent experiments by Jero and Kerans [16] and Fuller *et al.* [27, 28] have demonstrated an important effect of interface morphology on the constrained sliding of fibers in glass matrix composites in which residual compressive stresses existed normal to the interface. Fibers were pushed and pulled out of thin slices of composite (i.e. complete sliding) while the loads required to move the fibers were measured. When the direction of sliding was reversed, significant load drops were observed as the fibers returned to their original positions, whereas the load increased as the fibers moved past these positions. The distance over which the sliding load was reduced was approximately $10 \mu\text{m}$, similar to the period of surface roughness on the fibers, and similar also to the range of displacements in Fig. 5. These results suggest that sliding of surface irregularities over each other causes increased sliding resistance.

A constant sliding resistance along the debonded interface, as indicated by the results in Fig. 5, could be consistent with a Coulomb friction law governing local interfacial sliding if the effect of Poisson's contraction is exactly cancelled by the increased sliding resistance due to surface roughness. The surface roughness causes an increased radial misfit strain between the fibers and matrix as illustrated in Fig. 14, which tends to oppose the decrease in misfit strain due to Poisson's contraction. The misfit due to surface roughness increases continuously with the magnitude of the local relative sliding displacement of the fiber and matrix, as long as the sliding displacement is smaller than the period of the roughness. At a given applied load, the local sliding displacements are maximum near the surface of the test specimen (equal to the measured displacement) and decrease to zero at the end of the sliding region. The Poisson's contraction, which is proportional to the change in axial strain in the fiber, decreases similarly over the sliding region. Therefore there is a tendency for the roughness and Poisson's effects to cancel locally over the entire sliding region, if the displacements are smaller than the period of the roughness. This condition is satisfied for all of the data in Fig. 5, since at the peak load (50 N) the measured displacement is $\sim 10 \mu\text{m}$, which is similar to the period of the surface roughness on the fiber (Figs 7 and 10). At this peak applied load, the difference in axial strains in the fiber at the surface of the matrix and in the bulk of the composite is ~ 0.01 , which leads to a radial contraction of $\sim 0.2 \mu\text{m}$. This is similar to the amplitude of the roughness of the fiber.

6. CONCLUSIONS

Measurements of single fiber sliding in a $\text{Ti}_3\text{Al-SiC}$ composite have been obtained with sufficient accuracy to permit detailed comparison with the predictions of several micromechanical models, and thereby allow measurement of interfacial properties. The results differ significantly from the response expected

of a smooth interface governed by a Coulomb friction law; instead the interfacial sliding resistance is constant along the debonded region of interface (shear stress of 66 MPa). These results and other observations in the literature lead us to suggest that the combination of surface roughness and the constrained geometry of the sliding test tend to cancel the effect of Poisson's contraction when fibers are loaded in tension.

When sliding displacements were small ($< 10 \mu\text{m}$, corresponding to partial debonding and sliding) the sliding resistance remained constant during both monotonic and cyclic loading. However, substantial degradation of the sliding resistance was observed when the sliding displacements were large, corresponding to pullout with complete debonding and sliding.

Acknowledgements—The research described here was supported by the U.S. Air Force, Contract F33615-90-C-5928 (the cyclic loading experiments) and by Rockwell International Science Center Independent Research and Development funding (initial development of the fiber pulling technique).

REFERENCES

1. B. N. Cox, M. R. James, D. B. Marshall, W. L. Morris and M. C. Shaw, *Proc. 10th Int. SAMPE Conf.*, Birmingham, England (1989).
2. B. N. Cox and D. B. Marshall, in *Proc. Fatigue '90, 4th Int. Conf. on Fatigue and Fatigue Thresholds* (edited by H. Kitagawa and T. Tahaka), MCE, Birmingham (1990).
3. R. A. Naik and W. S. Johnson, NASA Technical Memorandum 101688 (1989).
4. D. B. Marshall, B. N. Cox, W. L. Morris and M. C. Shaw, in *Proc. Symp. on Composites, 2nd Int. Ceramic Science & Technology Congress*, Am. Ceram. Soc. (1990). In press.
5. D. B. Marshall and W. C. Oliver, *J. Am. Ceram. Soc.* **70**, 542 (1987).
6. D. B. Marshall and W. C. Oliver, *J. Mater. Sci. Engng* **A126**, 95 (1990).
7. T. P. Weihs and W. D. Nix, *J. Am. Ceram. Soc.* **74**, 524 (1991).
8. T. P. Weihs, C. M. Dick and W. D. Nix, in *MRS Symp. Proc. 120* (edited by F. D. Lemkey, S. G. Fishman, A. G. Evans and J. R. Striffe) (1988).
9. D. B. Marshall, *J. Am. Ceram. Soc.* **67**, 259 (1984).
10. M. K. Brun and R. N. Singh, *Adv. Ceram. Mater.* **3**, 506 (1988).
11. R. J. Kerans, R. S. Hay, N. J. Pagano and T. A. Parthasarathy, *Am. Ceram. Bull.* **68**, 429 (1989).
12. G. Morscher, P. Pirouz and A. H. Heuer, *J. Am. Ceram. Soc.* **73**, 713 (1990).
13. J. W. Laughner and R. T. Bhatt, *J. Am. Ceram. Soc.* **72**, 2017 (1989).
14. T. P. Weihs and W. D. Nix, *Scripta metall.* **22**, 271 (1988).
15. J. D. Bright, D. K. Shetty, C. W. Griffin and S. Y. Limaye, *J. Am. Ceram. Soc.* **72**, 1891 (1989).
16. P. D. Jero and R. J. Kerans, *Scripta metall.* **24**, 2315 (1990).
17. J. I. Eldridge and P. K. Brindley, *J. Mater. Sci. Lett.* **8**, 1451 (1989).
18. C. J. Yang, S. M. Jeng and J.-M. Yang, *Scripta metall.* **24**, 469 (1990).
19. J. W. Hutchinson and H. M. Jensen, *Mech. Mater.* **9**, 139 (1990).
20. D. B. Marshall, *Acta metall. mater.* **40**, 427 (1992).
21. X. J. Ning, P. Pirouz, K. P. D. Lagerlof and J. DiCarlo, *J. Mater. Res.* **5**, 2865 (1990).
22. B. N. Cox, M. R. James, D. B. Marshall and R. C. Addison Jr., *Metall. Trans.* **21A**, 2701 (1990).
23. C. G. Rhodes, Rockwell International Science Center, unpublished work.
24. D. R. Williams, D. L. Davidson and J. Lankford, *Exp. Mech.* **20**, 134 (1980).
25. M. R. James, W. L. Morris and B. N. Cox, *Exp. Mech.* **30**, 60-68 (1990).
26. L. B. Freund, *Eur. J. Mech. A*, In press.
27. E. R. Fuller Jr, E. P. Butler and W. C. Carter, in *Proc. NATO Advanced Research Workshop on Toughening Mechanisms in Quasi Brittle Materials*, Northwestern University (1990).
28. W. C. Carter, E. P. Butler and E. R. Fuller Jr, *Scripta metall.* In press.

APPENDIX B
ANALYSIS OF FIBER DEBONDING AND SLIDING EXPERIMENTS IN
BRITTLE MATRIX COMPOSITES

Acta. Metall. 40[3], 427-441 (1992)

ANALYSIS OF FIBER DEBONDING AND SLIDING EXPERIMENTS IN BRITTLE MATRIX COMPOSITES

D. B. MARSHALL

Rockwell International Science Center, 1049 Camino Dos Rios, Thousand Oaks,
CA 91360, U.S.A.

(Received 30 April 1991; in revised form 20 August 1991)

Abstract—The use of a recent analysis of fiber debonding and sliding in brittle matrix composites to interpret the results of fiber pulling and pushing experiments is examined. The stress-displacement relations are expressed in normalized forms that are convenient for curve fitting to experimental measurements and the analysis is extended to provide stress-displacement relations for cyclic loading in addition to monotonic loading. The ranges of some of the important elastic parameters and their influence on the stress-displacement relations are examined. Differences between single and multiple fiber pulling and between pushing and pulling experiments are assessed.

Résumé—On examine l'usage d'une analyse récente de la décohésion et du glissement des fibres dans des composites à matrice fragile afin d'interpréter les résultats d'expériences de traction-compression sur les fibres. Les relations contrainte-déplacement sont exprimées sous des formes normalisées qui conviennent pour faire coïncider les courbes et les mesures expérimentales, et cette analyse est étendue pour obtenir des relations contrainte-déplacement dans le cas d'une charge cyclique ajoutée à la charge monotone. On étudie le domaine de variation de quelques paramètres élastiques importants, et leur influence sur les relations contrainte-déplacement. On met en évidence des différences entre les expériences de traction sur une ou plusieurs fibres, et entre les expériences de compression et de traction.

Zusammenfassung—Es wird untersucht, inwieweit eine kürzlich entwickelte Analyse der Ablösung und des Gleitens von Fasern in Verbundwerkstoffen mit spröder Matrix auf Ergebnisse von Experimenten des Faserausziehens und -einstoßens angewendet werden kann. Die Spannungs-Dehnungsbeziehungen werden in normalisierter Form dargestellt, weil diese günstig für die Kurvenanpassung der experimentellen Messungen sind. Die Analyse wird erweitert, um zusätzlich zu den Spannungs-Dehnungsbeziehungen für monotone Belastung solche für zyklische Belastung zu erhalten. Der Bereich einiger wichtiger elastischer Parameter und deren Einfluß auf die Spannungs-Dehnungsbeziehungen werden untersucht. Die Unterschiede zwischen Einzelfaser- und Vielfachfaserausziehen und zwischen Zug- und Druckexperimenten werden behandelt.

1. INTRODUCTION

Techniques based on the pushing and pulling of fibers have been developed recently for measuring mechanical properties of interfaces in ceramic and inter-metallic matrix composites [1-18]. A wide variety of specimen and loading configurations have been used, including single or multiple fibers and very thick or thin specimens. The most sensitive of these experiments provide continuous measurements of the applied force and the relative sliding displacements of the fiber and matrix, as debonding and sliding progress stably along the fiber [2-7]. Calculation of interfacial properties, such as debond energy and frictional sliding resistance, from these measurements relies on curve fitting with theoretical predictions derived from micromechanics modeling of the debonding and sliding process.

Most analyses of fiber sliding have been based on shear-lag models with various degrees of approximation. The simplest models assume that sliding along a debonded interface is resisted by a constant shear stress τ , an approximation that turns out to be

remarkably good for many experiments [2-7]. This model has also been extended to account for the effects of Mode II fracture energy associated with the tip of the debond crack and axial residual stress in the fiber [6]. Other models have been suggested based on a Coulomb friction law governing the sliding resistance, but not accounting for the influence of axial residual stress in the fibers (which we shall show later has a dominant effect on the response) [19, 20]. Three recent analyses have accounted for both axial and radial residual stresses with a Coulomb friction law, one by Hutchinson and Jensen [21] for mechanically loaded fibers, another by Cox [22] for thermally loaded fibers (i.e. sliding that occurs near a free surface during thermal cycling, as a result of a mismatch in thermal expansion coefficients of the fibers and matrix) and the third by Kerans and Parthasarathy [23] for the special case of a single isotropic, mechanically loaded fiber in an infinite matrix.

Exact numerical results, based on a full elasticity solution for the matrix, have been obtained recently by Freund [24] for the problem of complete sliding of

a finite, unbonded fiber along a cylindrical hole in an infinite matrix. Direct comparison of stress distributions in the fiber with those of the Lamé solution used by Hutchinson and Jensen [21] indicated good agreement over a wide range of relative elastic stiffness values. Numerical solutions and approximate analytical results have also been given by Sigl and Evans [25] for partial debonding and sliding. Another analytical approach, which is approximate and which also requires numerical solutions to obtain slip lengths and displacements, has been used by McCartney [26] to analyze a variety of fiber sliding problems. However, for comparison with fiber sliding experiments, the explicit analytical results of Hutchinson and Jensen [21] are especially convenient, as well as being more general than most prior work in the treatment of boundary conditions, debonding, and anisotropy.

The purpose of this paper is to examine the use of Hutchinson and Jensen's analysis to deduce interfacial properties from experimental measurements of fiber sliding. Their analysis provides explicit relations for the relative sliding displacements as a function of monotonically increasing applied load. The model will be extended to provide similar relations for displacements during an unload/reload cycle. Such measurements provide valuable additional information for deducing interfacial properties, since the displacements are independent of the debond energy and the initial axial residual stress in the fibers.

Although the analysis of Hutchinson and Jensen provides concise and convenient expressions for stresses, strains, and debond energies, the displacement equations contain a large number of parameters which characterize the elastic properties of the fibers and matrix, residual misfit strains, anisotropy of the fibers, volume fraction of fibers, friction coefficient (or, in the case of constant sliding resistance, a frictional stress) and interfacial debond energy. The equations will be expressed in a normalized form that reduces the number of explicit parameters to three, in addition to load and displacement. One of these parameters is a combination of elastic constants; another, S_{R0} , characterizes the initial residual stresses; and the third parameter, Γ , characterizes the Mode II debond energy at the crack tip (S_{R0} and Γ are also dependent on elastic constants). The influence of each of these parameters on the load-displacement curves will be examined. The ranges of some of the important elastic parameters in typical composites will be explored, and differences between single fiber and multiple fiber pulling will be assessed.

†For a transversely isotropic material loaded in the axial or transverse directions there are three Poisson's ratios, ν_{ij} , ν_{ii} , and ν_{jj} , where ν_{ij} refers to strain in direction i due to stress in direction j . However, since ν_{ii} and ν_{jj} are related by $\nu_{ii} = \nu_{jj} E_j / E_i$, only two of the Poisson's ratios, $\nu_{ij} \equiv \nu_i$ and $\nu_{jj} \equiv \nu_j$, in addition to the Young's moduli E_i and E_j , are needed to specify the elastic response.

2. REVIEW OF MODEL OF HUTCHINSON AND JENSEN

The concentric cylinder model depicted in Fig. 1(a) is taken to represent a composite reinforced with a volume fraction $f = R_f/R$ of aligned continuous fibers. The analysis is restricted to composites with a residual compressive stress acting across the fiber-matrix interface, as is usually the case with intermetallic matrix composites and sometimes the case with ceramic matrix composites. Pulling (or pushing) on the fiber at the end of the cylinder (which corresponds to a sectioned surface or a crack surface of the composite) causes a debond crack to grow along the fiber-matrix interface. The length of the debond is dictated by a Mode II fracture energy, G_c , at the crack tip and frictional sliding over the debonded surfaces. Two types of sliding resistance will be considered; (1) a constant frictional stress, τ_0 , between the fibers and matrix over all regions where sliding occurs, and (2) Coulomb friction, with the frictional stress being proportional to the normal stress, σ_r , (which is negative) across the sliding interface

$$\tau = \mu \sigma_r \quad (1)$$

where the friction coefficient, μ , is taken as constant.

The frictional sliding causes relative displacements of the fiber and matrix at the end of the cylinder ($z = l$). These displacements are measured in push/pull experiments and are related to the opening displacements of a bridged crack in the composite. The displacements are given by integrals of the axial strains in the fiber and matrix. The analysis of Hutchinson and Jensen [21] provides solutions for the axial strains in terms of frictional properties, debond energy and other relevant parameters. Most of the discussion here will refer explicitly to fiber pulling, although the analysis applies also to pushing, and specific relations for pushing will be presented in Section 6.

The notation of Hutchinson and Jensen [21] will be used as far as possible, although some new normalizing parameters will be defined in later sections. The matrix is taken as elastic and isotropic, with Young's modulus E_m and Poisson's ratio ν_m . The fiber is taken to be transversely isotropic, with Young's moduli E_r and E_t , in the axial and transverse directions, and Poisson's ratios ν_r and ν_t governing transverse Poisson's strains due to axial and transverse loading respectively.† The properties ν_r and E_r enter the analysis via the parameter $\zeta_f \equiv (1 - \nu_r)E_r/E_t$. Here we define $\zeta_f \equiv \zeta_f/(1 - \nu_r)$, so that for isotropic fibers $\zeta_f = 1$. To maintain analytical tractability, the analysis of unload/reload cycles will be restricted to cases with either $\nu_t = \nu_m$ or $f = 0$. The elastic misfit strains between the fiber and matrix are ϵ_r^T and ϵ_t^T in the radial and axial directions, characterized in Ref. [21] by $\epsilon^T \equiv \epsilon_r^T$ and $\lambda \equiv \epsilon_t^T/\epsilon_r^T$. As discussed in Ref. [21], the misfit could arise from mismatch of thermal

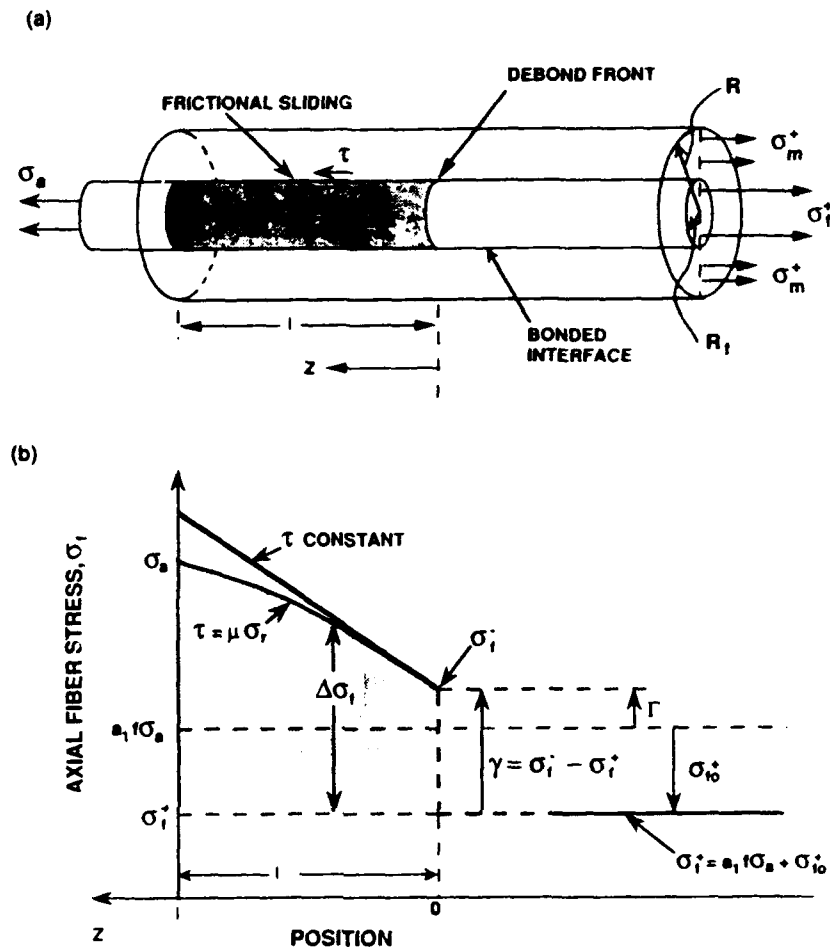


Fig. 1. (a) Composite cylinder model used for analysis. (b) Axial stresses in fiber during initial loading

expansion coefficients, or from irregularities of the fiber surface. For the former, ϵ^T and λ are constant under isothermal conditions, whereas the misfit due to nonuniformity would be dependent upon the amount of sliding, and thus the applied load and position along the fiber. Preliminary analyses of misfit strains due to nonuniformity have been done recently by several authors [23, 27] and could possibly be incorporated in the present analysis. However, this was not attempted here. If the residual stresses cause yielding of the matrix during cooling from the fabrication temperature, both ϵ^T and λ may differ from values calculated for a purely elastic response during cooling.

Stresses and strains in any section transverse to the z axis were evaluated on the basis of the Lamé solution, an approximation that is valid if the axial stresses vary slowly over distances comparable to the fiber radius. This condition is satisfied if τ is small compared with the axial stress in the fiber, σ_f . Two types of boundary conditions on the outer cylindrical

surface were considered. Type I has zero normal and shear tractions, $w = 0$. Type II also has zero shear tractions, but has radial displacement, u_r , constrained to be the same as its value far ahead of the debond crack. Type I conditions are appropriate for single fiber pulling or pushing experiments and in general at positions well ahead of the debond crack. Type II conditions are appropriate over the debonded region of a composite in which all fibers are pulled equally (such as bridging fibers within a crack), provided the slip length is small compared with the specimen width. Type II conditions were also used by Cox [22] in analyzing sliding of fibers near a free surface during thermal cycling, whereas earlier analyses used only Type I boundary conditions. We will see later that large differences in load-displacement relations can result from these different boundary conditions.

The axial stresses, σ_f , in the fiber during initial loading are shown schematically in Fig. 1(b). Well ahead of the debonded region the stresses and strains

are constant and given by the Lamé problem with Type I boundary conditions, as well as the conditions that the axial strains ϵ_f and ϵ_m in the fiber and matrix be equal and the normal stresses and displacements at the fiber-matrix interface be continuous. With the superscript (+) denoting positions well ahead of the debond, the subscript r denoting radial stresses, strains and displacements at the interface, and the subscripts f and m denoting axial quantities in the fiber and matrix, the stresses and strains† are given by

$$\sigma_r^+ = a_1 f \sigma_a - a_2 E_m \epsilon^T \quad (2a)$$

$$\sigma_r^+ = a_3 f \sigma_a - a_4 E_m \epsilon^T \quad (2b)$$

$$\epsilon_f^+ = \epsilon_m^+ = a_5 f \sigma_a / E_m + a_6 \epsilon^T \quad (2c)$$

where the a 's are nondimensional functions of f , E_f/E_m , ν_f , ν_m/ν_f , ξ_f , and λ , given in Ref. [21], and σ_a is the axial stress in the loaded end of the fiber (for convenience in later analysis of single fiber loading, corresponding to $f=0$, this definition of loading parameter differs slightly from that in Ref. [21], where the average stress $\bar{\sigma} = f \sigma_a$ is used). Behind the debond crack tip the changes in stresses and strains relative to their values far ahead of the crack (i.e. $\Delta \sigma_r = \sigma_r - \sigma_r^+$, $\Delta \epsilon_f = \epsilon_f - \epsilon_f^+$, etc.) are given by the Lamé problem without mismatch strain and, since there is relative sliding, with $\Delta \epsilon_f \neq \Delta \epsilon_m$. With continuity of $\Delta \sigma_r$ and Δu_r across the interface, and the equilibrium requirement $f \Delta \sigma_r + (1-f) \Delta \sigma_m = 0$, the stresses and strains may be written as

$$\Delta \sigma_m = \left(\frac{f}{1-f} \right) \Delta \sigma_r \quad (3a)$$

$$\Delta \sigma_r = b_1 \Delta \sigma_f \quad (3b)$$

$$\Delta \epsilon_f = b_2 \Delta \sigma_f / E_m \quad (3c)$$

$$\Delta \epsilon_m = -b_3 \Delta \sigma_f / E_m \quad (3d)$$

where the b 's are another set of nondimensional functions of the same parameters as the a 's (with the exception of λ) given in Ref. [21]. There are two sets of b 's corresponding to Type I and Type II boundary conditions.

There is a jump in the fiber stress from just behind to well ahead of the debond crack tip, which is dependent upon the Mode II fracture energy, G_c . This relation is given approximately by [21]

$$\gamma \equiv \sigma_f^+ - \sigma_f^- = \frac{(1-f)}{f c_1 c_3} \left(\frac{E_m G_c}{R_f} \right)^{1/2} \quad (4)$$

where

$$c_1 = (1-f a_1)(b_2 + b_3)^{1/2} / (2f) \quad (5a)$$

$$c_3 = (1-f) / (1-f a_1) \quad (5b)$$

and the superscript (-) denotes quantities just behind the crack tip. Comparison with full numer-

ical solutions in Ref. [21] shows that equation (4) is a good approximation if the sliding distance exceeds 2-3 times the fiber radius. The error is shown to be $\sim \tau/\sigma_f$, and thus becomes less significant as the applied load increases.

The axial stresses in the fiber over the debonded region are governed by the equilibrium condition

$$\frac{d\sigma_r}{dz} = \frac{-2\tau}{R_f} \quad (6)$$

and the boundary conditions at $z=0$ and l . For constant frictional stress, σ_r increases linearly as shown in Fig. 1(b), whereas for Coulomb friction the increase is nonlinear. The curvature is determined by the parameter b_1 in equation (3), which relates changes in normal interfacial stress to changes in axial stress. Hutchinson and Jensen [21] pointed out that b_1 can be either positive or negative. For Type I boundary conditions b_1 is always positive, so that the compressive interfacial stress decreases in magnitude as σ_r increases, corresponding to the commonly perceived effect of Poisson's contraction, and leading to the curvature shown in Fig. 1(b). However, for Type II boundary conditions, b_1 can be negative for certain combinations of elastic properties. Physically this difference arises because under Type I conditions the relaxation of axial tension in the matrix during sliding causes transverse expansion of the outer boundary of the cylinder, so that in order to impose Type II conditions with $u_r = 0$ at the outer boundary, compressive normal tractions must be applied to the outer boundary. If the stress at the fiber-matrix interface due to the tractions exceeds the reduction in stress due to Poisson's contraction of the fiber, then b_1 is negative. In this case the curvature of the relation $\sigma_r(z)$ is opposite to that shown in Fig. 1(b) (i.e. increasing slope with increasing z).

To illustrate the range of composite properties for which b_1 is negative under Type II boundary conditions, the expression given by Hutchinson and Jensen [21] is plotted in Fig. 2 as a function of E_f/E_m for selected values of the other parameters (f , ν_f , ν_m/ν_f , and ξ_f ; note that b_1 is independent of λ). It is clear that large values of f , E_f/E_m , ν_f , and ν_m/ν_f tend to make b_1 negative. Moreover, for most composites of practical interest, b_1 is in fact negative.

Two displacements are of interest in the following sections. The relative displacement of the fiber and matrix at $z=l$ (which corresponds to the measurements obtained in fiber pulling/pushing experiments) is given by

$$\delta = \int_0^l (\epsilon_f - \epsilon_m) dz = \frac{b_2 + b_3}{E_m} \int_0^l \Delta \sigma_r dz \quad (7)$$

and is, therefore, proportional to the shaded area in Fig. 1(b). The displacement that is used as the crack opening in continuum models of crack bridging is the

†Strains in both the fibers, ϵ_f^+ , and matrix, ϵ_m^+ are measured relative to the unstressed state of the matrix.

additional fiber displacement due directly to debonding and sliding [28-30] given by

$$\Delta = \int_0^l (\epsilon_f - \epsilon_f^*) dz = \frac{b_2}{E_m} \int_0^l \Delta \sigma_f dz \quad (8a)$$

Therefore, the displacements δ and Δ are related simply by

$$\Delta = \left(\frac{b_2}{b_2 + b_3} \right) \delta \quad (8b)$$

Equation (8b) relates the displacements measured in a multiple fiber pulling experiment directly to the crack opening in bridging models for given fiber stress, σ_a . However, the relation is less direct for single fiber pulling experiments, because in that case δ is evaluated using Type I boundary conditions whereas δ for the multiple fiber pulling (and crack opening) is evaluated with Type II boundary conditions over the debonded region.

3. DISPLACEMENTS DURING FIBER PULLING: COULOMB FRICTION

In this section the relative displacements, δ , of the fiber and matrix at $z = l$ are evaluated as the stress σ_a applied to the end of the fiber is increased continuously from zero to a peak value σ_p (initial loading), decreased to zero, and then increased again to σ_p . During initial loading, debonding and sliding progress stably along the fiber/matrix interface, whereas during unloading reverse sliding occurs. The unload/reload cycle exhibits hysteresis due to the frictional response of the interface. The fiber strength is assumed to be larger than σ_p so that failure of the fiber does not occur. The peak stress is also restricted to be smaller than the limiting value at which the normal interfacial stress decreases to zero; at this limit the debond extends along the entire fiber, with a constant length zone of contact behind the debond tip, as discussed by Hutchinson and Jensen [21].

3.1. Initial loading

The displacement, δ , during initial loading is obtained by integration of equation (7), after first evaluating the axial stresses in the fiber over the debonded region by integration of equation (6), with τ given by equations (1), (2b) and (3b), and the boundary conditions $\sigma_f = \sigma_f^*$ at $z = 0$ and $\sigma_f = \sigma_a$ at $z = l$. Details are given in the Appendix. The displacement and the corresponding debond length can be conveniently expressed as follows, in terms of dimensionless parameters normalized by the peak value of the applied stress, σ_p

$$\delta/\delta^* = -A S_{R0} \ln \left[\frac{S_{R0} - S_a}{S_{R0} - \Gamma'} \right] + \Gamma' - S_a \quad (9)$$

and

$$l/R_f = \left(\frac{1}{2\mu} \right) \ln \left[\frac{S_{R0} - S_a}{S_{R0} - \Gamma'} \right] \quad (10)$$

where

$$S_a = \sigma_a/\sigma_p \quad (11a)$$

$$S_{R0} = -\frac{\sigma_{R0}}{(1 - a_1 f)\sigma_p} \quad (11b)$$

$$\Gamma' = \frac{\Gamma}{(1 - a_1 f)\sigma_p}, \Gamma = \gamma + \sigma_{f0}^* \quad (11c)$$

$$\delta^* = \left[\frac{(b_2 + b_3)(1 - a_1 f)}{2b_1} \right] \left(\frac{\sigma_p R_f}{\mu E_m} \right) \quad (11d)$$

$$A = \left(1 - \frac{a_2 b_1}{a_4} \right)^{-1} \quad (11e)$$

$$\sigma_{R0} = \left(\frac{a_4}{a_2 b_1} - 1 \right) \sigma_{f0}^* = \sigma_{f0}^*/(A - 1) \quad (11f)$$

$$\sigma_{f0}^* = -a_2 E_m \epsilon^T \quad (11g)$$

Thus equation (9) provides a relation between displacement δ and applied load, S_a , with four other parameters which characterize the frictional properties of the interface (δ^*), the residual stresses (S_{R0}), the interfacial debond energy (Γ'), and the elastic properties and misfit strain anisotropy of the fiber and matrix (A). Equation (9) requires $(a_1 f/b_1) = 0$. This condition is satisfied for single fiber pulling experiments (i.e. $f = 0$), or for $v_f = v_m$ (for which $a_3 = 0$) with Type I boundary conditions (for which b_1 is always finite). However, for multiple fiber pulling with Type II boundary conditions, certain combinations of elastic properties give $b_1 = 0$ (see Fig. 2), for which $(a_1 f/b_1)$ is singular. This limit results in a constant frictional stress along the debonded interface (see Section 4). For values of v_f/v_m close to unity, the transition between very small values of $(a_1 f/b_1)$ and the singular values occurs over small ranges of the other elastic parameters. Therefore attention hereunder will be restricted to the case $(a_1 f/b_1) \approx 0$. The full expression for non-zero values of this parameter, given in equation (A7), is equivalent to equations (47) and (49) of Ref. [21]. For the special case $f = 0$ with an isotropic fiber and isotropic misfit strains, equation (9) is equivalent to the expression derived by Kerans and Parthasarathy [23].

The dependence of the parameter A on E_f/E_m for various values of λ , f , and v is shown in Fig. 3 for both multiple fiber pulling or pushing (Type II boundary conditions) and for single fiber experiments in which one fiber is pulled or pushed from a composite containing many fibers (in this case $f = 0$ for evaluation of b_1 , but $f \neq 0$ for evaluation of a_2 and a_4). Since

$$\left| \frac{a_2 b_1}{a_4} \right| < 1$$

for all reasonable composite properties, positive values of b_1 give $A > 1$ and negative values of b_1 give $0 < A < 1$.

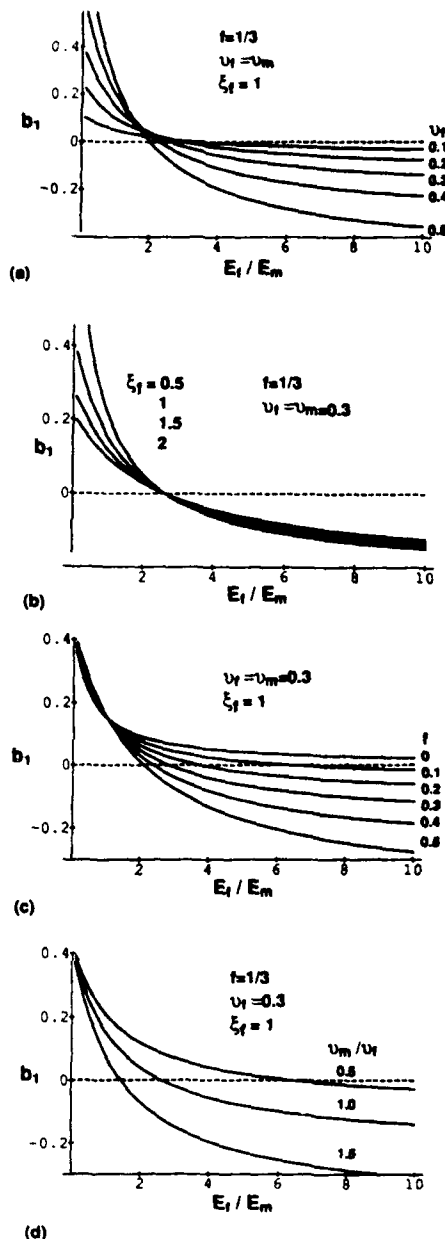


Fig. 2. Dependence of the parameter b_1 on properties of fiber and matrix, for Type II boundary conditions.

The other parameters may be interpreted physically as follows. The stress σ_{r0}^* is the residual axial stress in the fiber in the absence of applied load and debonding, as indicated in Fig. 1(b). The residual stress parameter σ_{r0} , while related to σ_{r0}^* by equation (11f), can also be written as $\sigma_{r0} = \sigma_{r0}^*/b_1$, where σ_{r0} is the normal interfacial stress when the axial stress in the fiber is zero. Note that, since σ_{r0} must be negative, σ_{r0} is positive for $b_1 < 0$ and negative for $b_1 > 0$. The axial and radial residual stresses could be treated as independent parameters, their relative

values being defined by the mismatch strain anisotropy, λ , through its influence on the parameter A . Then the dimensionless parameter S_{r0} represents the radial residual stress and $S_{t0} = (A - 1)S_{r0}$ represents the axial residual stress. The parameter Γ' relates directly to the applied stress required for initiation of debonding. To cause debonding, the applied stress must exceed the axial stress ahead of the debond, i.e. $\sigma_a > \sigma_r' + \gamma$, or with, equations (2a) and (11c), $\sigma_a(1 - a_1 f) > \Gamma'$. Therefore, the condition for debonding becomes $S_a = \Gamma'$.

Spontaneous debonding and sliding (i.e. at $\sigma_a = 0$) can occur during formation of the free surface at $z = l$ if $\Gamma' \leq 0$. For the modeling of bridged cracks, the displacement due to this spontaneous debonding becomes part of the crack opening displacement and equation (9) is not affected. However, in fiber pulling and pushing experiments, the displacements are measured relative to the spontaneously debonded condition, whereupon the displacement is reduced by an amount $\delta(0)$ given by equation (9) at $\sigma_a = 0$. Therefore the measured

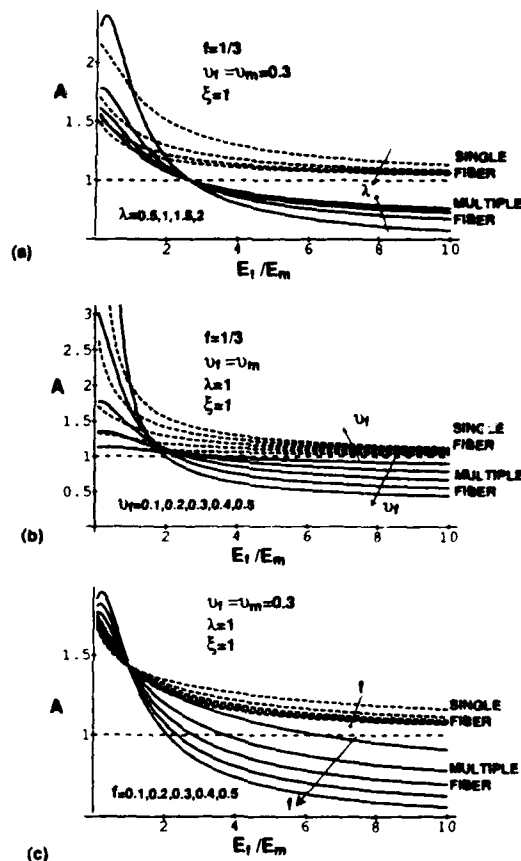


Fig. 3. Dependence of the parameter A on properties of fiber and matrix. Multiple fiber pulling or pushing corresponds to Type II boundary conditions on outer surface of cylinder. Single fiber results correspond to one fiber being pulled or pushed from a composite.

displacement is

$$\frac{\delta - \delta(0)}{\delta^*} = -A S_{R0} \ln \left[\frac{S_{R0} - S_a}{S_{R0}} \right] - S_a, \quad (\Gamma' < 0). \quad (12)$$

In this case there is no effect of the debond energy G_c on the stress-displacement measurements; conversely, under this condition such measurements cannot be used to evaluate G_c , although they do provide an upper bound for the debond energy, defined by the condition $\Gamma' < 0$, i.e. $\gamma < |\sigma_{i0}^*|$.

The range of applied loads for which the preceding relations hold is limited by the requirement that the normal interfacial stress be compressive. This condition is violated for tensile applied loads above a critical value when b_1 is positive, and for compressive loads above critical value for negative values of b_1 . At these critical loads the debond extends along the entire length of the fiber with a constant limited zone of contact behind the debond tip [21, 26]. Equation (9) approaches this limit asymptotically at $S_a = S_{R0}$. For a given peak load, the interfacial stress is smallest at $z = l$, and can be written

$$\sigma_n = b_1 \sigma_p (1 - a_1 f) (1 - S_{R0}). \quad (13)$$

If the product $(b_1 \sigma_p)$ is positive (i.e. fiber pulling with $b_1 > 0$ or fiber pushing with $b_1 < 0$), S_{R0} is positive (S_{R0} can be written as $S_{R0} = -\sigma_{i0}/[(1 - a_1 f)b_1 \sigma_p]$). Therefore, σ_n is compressive only for $S_{R0} > 1$. For negative values of $(b_1 \sigma_p)$, S_{R0} is negative and σ_n is always compressive.

For the purpose of curve fitting to experimental push/pull experiments, and for comparison with unload/reload cycles, it is convenient to refer the displacements to the peak load displacement, δ_p , given by equation (9) at $S_a = \sigma_p$ (i.e. $S_a = 1$)

$$\frac{\delta_p - \delta}{\delta^*} = -A S_{R0} \ln \left[\frac{S_{R0} - 1}{S_{R0} - S_a} \right] + S_a - 1. \quad (14)$$

In this form a single curve can be plotted, as shown in Fig. 4, for all values of Γ' and given A , S_{R0} and δ^* , with Γ' simply affecting the position of the displacement origin, corresponding to debond initiation at $S_a = \Gamma'$. Moreover, with Γ' evaluated from the intercept at $\delta = 0$, S_{R0} can be determined from a single-parameter curve fit to the measured stresses and displacements, normalized to their maximum values, provided the value of A is known independently. An example of a set of curves for $\Gamma' \leq 0$ and $A = 1.14$ (corresponding to the properties of a $\text{Ti}_3\text{Al}/\text{SiC}$ composite studied in Ref. [7]) and various values of S_{R0} is shown in Fig. 5.

3.2. Unload/reload cycle

The axial fiber stresses during unloading, after loading initially to a peak load σ_p , are shown schematically in Fig. 6(a). Reverse sliding occurs

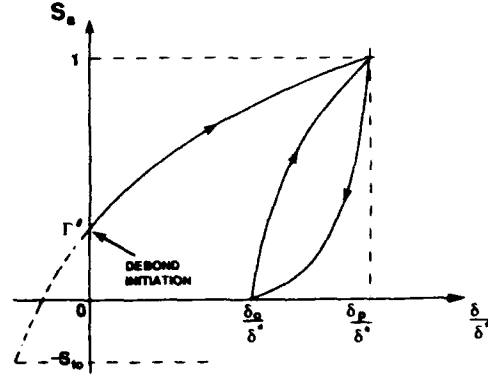


Fig. 4. Schematic representation of stress-displacement relation during initial loading, unloading and reloading

within a distance s of the end of the cylinder and the recovery in displacement is given by

$$\delta_p - \delta = \frac{b_2 + b_1}{E_m} \int_0^s (\Delta \sigma_{ip} - \Delta \sigma_i) dz \quad (15)$$

where the subscript p is used to denote quantities evaluated at the maximum load of the initial loading segment.

Following an analysis similar to that of the initial loading (see Appendix), the displacement becomes

$$\frac{\delta_p - \delta}{\delta^*} = (S_{R0} - S_a) \left[1 - \sqrt{\frac{S_{R0} - 1}{S_{R0} - S_a}} \right] \quad (16)$$

Equation (16) requires $(a_2 a_3 f / a_4) \ll 1$. This parameter is zero for either $v_i = v_m$ or $f = 0$, and is very small for all other likely composite properties (see Appendix). Also, equation (16) holds only for $s < l_p$. If Γ' is larger than a critical value defined in Fig. A1 (approximately $\Gamma' \geq 0.5$), the reverse slip region reaches the end of the debond before unloading is complete. The displacements under this condition are evaluated in the Appendix. However, this complication can be avoided in principle by the choice of a sufficiently large maximum load for the initial loading cycle.

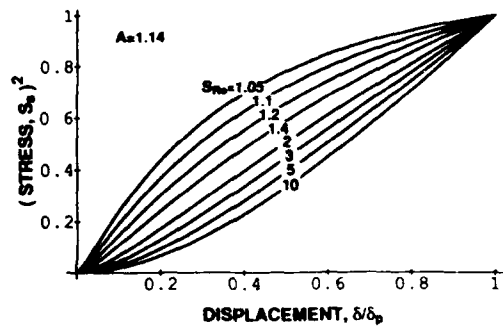


Fig. 5. Stress-displacement relation during initial loading for $A = 1.14$ and various values of residual stress parameter S_{R0} . Coulomb friction model.

The axial fiber stresses during reloading back to $\sigma_a = \sigma_p$ are shown schematically in Fig. 6(b). The displacements are given by

$$\delta - \delta_0 = \frac{b_2 + b_1}{E_m} \int_{l-l}^l (\Delta\sigma_l - \Delta\sigma_{l0}) dz \quad (17)$$

where the subscript 0 denotes quantities evaluated at the end of the previous unloading half cycle. The displacement, expressed relative to the peak load displacement, becomes (Appendix)

$$\frac{\delta_p - \delta}{\delta^*} = \frac{\delta_p - \delta_0}{\delta^*} - (S_{R0} - S_s) \left[1 - \sqrt{\frac{S_{R0}}{S_{R0} - S_s}} \right]^2 \quad (18)$$

These relations between the normalized displacements and stresses during unloading and reloading contain only one other parameter, S_{R0} , which, as mentioned earlier, characterizes the residual stress normal to the interface. Therefore the data from unload-reload cycles are useful supplements to the initial loading data for evaluating parameters. The

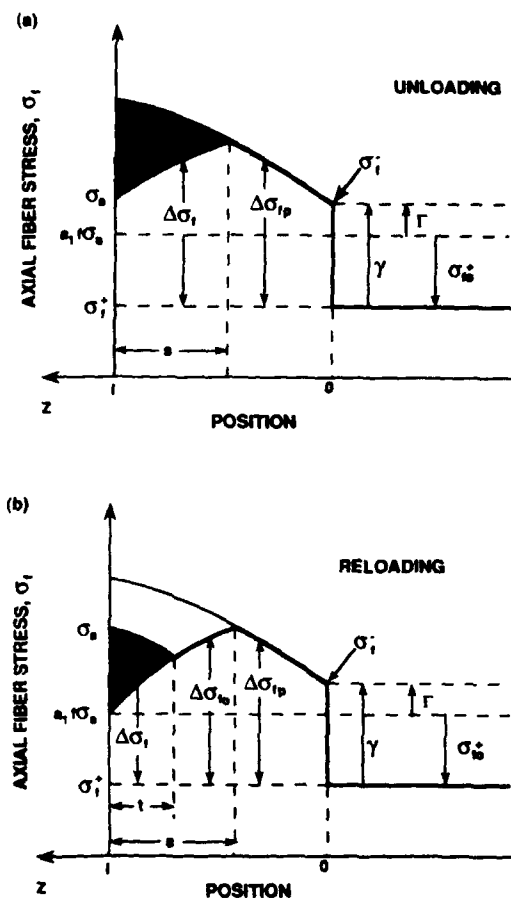


Fig. 6. Axial stresses in fiber during (a) unloading and (b) reloading, after loading initially to a peak stress σ_p . Change in displacement is proportional to area of shaded region. Coulomb friction model.

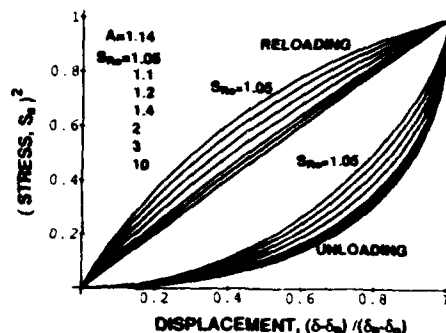


Fig. 7. Stress-displacement relation during an unload/reload cycle for $A = 1.14$ and various values of residual stress parameter, S_{R0} . Coulomb friction model.

unload-reload curves are plotted in Fig. 7 for various values of S_{R0} .

It is useful to identify two distinct effects of residual stresses on the changes in axial fiber stress during sliding and hence on the displacements. One enters via the normal interfacial stress, which determines the slope of $\Delta\sigma_l(z)$ (Figs 1 and 6). The other is the direct influence of the residual axial stress in the fiber, σ_{i0}^* , which adds a constant value to $\Delta\sigma_l(z)$ and affects the debond length, l , during initial sliding. During unloading and reloading, the changes in displacement are determined exclusively by the first of these effects, whereas the displacements during initial loading are affected most strongly by the influence of σ_{i0}^* . Consequently, the ratio of displacements δ_p and $(\delta_p - \delta_0)$ resulting from initial loading and complete unloading provides a sensitive measure of the magnitude of the residual stress parameter S_{R0} , as shown in Fig. 8. Moreover, the role of the axial component of residual stress can be seen from Fig. 8 by recognizing that the curve for $A = 1$ corresponds to zero axial residual stress [$a_2 = 0$ in equation (2a) and equation (11e)]. Since $(\delta_p - \delta_0)$ is independent of A , the curves for various values of A in Fig. 8 provide a direct comparison of the relative displacements during initial loading with and without axial residual stress. We note also that the result of Gao *et al.* [19] (their equation (2.28)), who analyzed initial fiber sliding with Type I boundary conditions and without axial residual stress

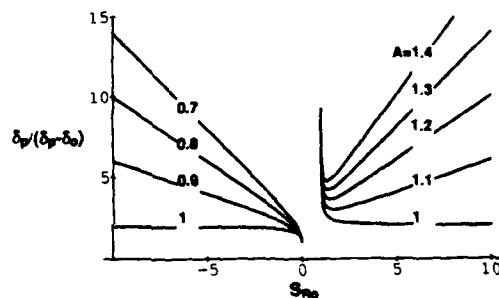


Fig. 8. Ratio of the displacement δ_p caused by initial loading to stress σ_p , to the displacement $(\delta_p - \delta_0)$ recovered during complete unloading. Coulomb friction model.

in the fiber, is equivalent, with $v_f = v_m$ or $f = 0$, to equation (9) with $A = 1$.

4. DISPLACEMENTS DURING FIBER PULLING: CONSTANT FRICTION

With the frictional stress taken as a constant, τ_0 , the change in axial fiber stress, $\Delta\sigma_f(z)$, during initial monotonic loading increases linearly along the sliding region as shown in Fig. 1. The displacement, δ , from equation (7) can be written immediately [from inspection of the areas in Fig. 1, with equation (6)] as

$$\delta = \frac{(b_2 + b_3)R_f}{4\tau_0 E_m} [(\sigma_a - \sigma_f')^2 - \gamma^2] \quad (19)$$

which is equivalent to equation (37) of Ref. [21]. Equation (19) is also obtained from the Coulomb friction result, equation (A7), in the limit $b_1 \rightarrow 0$, which corresponds to the normal interfacial stress being independent of changes in axial stress. With the definitions of equation (11), equation (19) can be written in terms of the same normalized parameters used for the Coulomb friction model

$$\delta/\delta^* = S_a^2 + 2(A-1)S_{R0}S_a - \Gamma'^2 - 2(A-1)S_{R0}\Gamma' \quad (20)$$

where

$$\delta^* = \left[\frac{(b_2 + b_3)(1 - a_1 f)^2}{4} \right] \left[\frac{R_f \sigma_p^2}{\tau_0 E_m} \right] \quad (21)$$

The parameter δ^* is related to the corresponding parameter, δ^* , that normalizes the displacements in the Coulomb friction model by

$$\delta^*/\delta^* = \frac{\mu b_1 (1 - a_1 f) \sigma_p}{2\tau_0} \quad (22)$$

As in the case of the Coulomb friction model, spontaneous debonding and sliding occur at a free surface if $\Gamma' \leq 0$. Then the displacement measured in a fiber pulling or pushing experiment becomes

$$\frac{\delta - \delta(0)}{\delta^*} \approx S_a^2 + 2(A-1)S_{R0}S_a \quad (23)$$

In this case the debond energy cannot be evaluated from the displacement measurements. The displacement measured relative to the peak load displacement, δ_p , is

$$\frac{\delta_p - \delta}{\delta^*} = 1 + 2(A-1)S_{R0} - S_a^2 - 2(A-1)S_{R0}S_a \quad (24)$$

During unloading from a peak load σ_p , the recovery in displacement is given by equation (15), which becomes [see Fig. 9(a)]

$$\delta_p - \delta = \left[\frac{(b_2 + b_3)(1 - a_1 f)^2 R_f}{8\tau_0 E_m} \right] [\sigma_p - \sigma_a]^2 \quad (25)$$

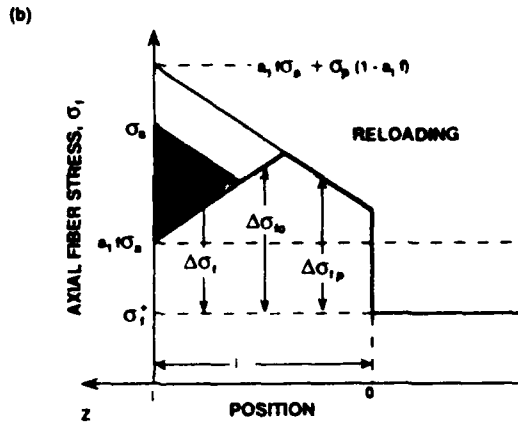
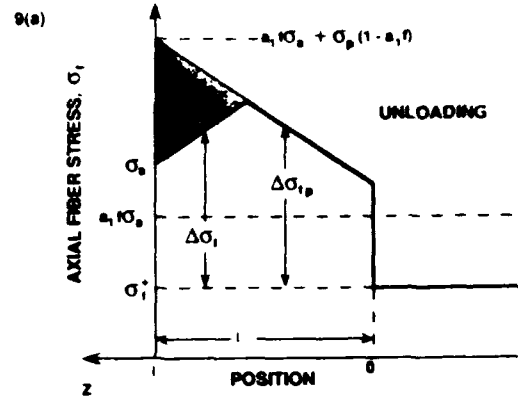


Fig. 9. Axial stresses in fiber during (a) unloading and (b) reloading after loading initially to peak stress σ_p . Change in displacement is proportional to area of the shaded region. Constant friction model

or, in terms of the previously defined normalized parameters

$$\frac{\delta_p - \delta}{\delta^*} = (1/2)[1 - S_a]^2 \quad (26)$$

Equations (25) and (26) are restricted to situations where σ_p is sufficiently large that the region of reverse slip does not reach the end of the debond before unloading is complete, as discussed in the previous section. For the constant friction model this condition requires $(1 - a_1 f)\sigma_m \geq 2\Gamma$, i.e. $\Gamma' < 1/2$. The corresponding displacement equations for smaller values of σ_m can be derived straightforwardly following the above procedure.

The displacements during reloading [equations (17) and Fig. 9(b)] are given by

$$\delta - \delta_0 = \left[\frac{(b_2 + b_3)(1 - a_1 f)^2 R_f}{8\tau_0 E_m} \right] \sigma_a^2 \quad (27)$$

where δ_0 is the displacement at the end of the previous unloading half-cycle. In terms of the normalized parameters, equation (27) becomes

$$\frac{\delta_p - \delta}{\delta^*} = \frac{\delta_p - \delta_0}{\delta^*} - S_a^2/2 \quad (28)$$

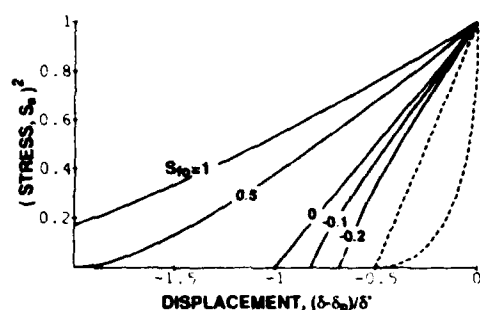


Fig. 10. Stress-displacement relation for constant friction model during load/unload/reload cycle for various values of the residual stress parameter $S_{R0} = S_{R0}(A-1)$. Full curves initial loading [equation (24)] broken curves unloading [equation (26)] and reloading [equation (28)].

The number of independent parameters in the normalized equations (20), (26) and (28) is one fewer than in their counterparts for Coulomb friction, since A and S_{R0} appear only in equation (20) in the combination $(A-1)S_{R0}$, which is just the normalized axial residual stress, S_{R0} . These equations are plotted in Fig. 10 for several values of S_{R0} .

It is instructive to compare the results of this section with an approximate constant τ analysis [6], used previously to model single fiber pushing experiments. In that analysis, elastic interactions of the fiber and matrix via Poisson's effects were neglected, but effects of debonding and residual axial fiber stresses were included. In the notation of this paper, the initial loading equation from Ref. [6] for pulling a fiber with compressive residual axial stress (equivalent to pushing a fiber with residual tensile axial stress) becomes

$$\delta = \frac{R_f}{4\tau_0 E_f} [(\sigma_a - \sigma_{i0}^*)^2 - 4G_c E_f / R_f]. \quad (29)$$

The corresponding result from equation (19) (with $f=0$ for single fiber pulling) can be written

$$\delta = \frac{b_2 R}{4\tau_0 E_m} \left[(\sigma_a - \sigma_{i0}^*)^2 - \frac{4E_m G_c}{b_2 R_f} \right] \quad (30)$$

where we have used equations (4) and (5) to substitute for γ , and the fact that $b_1 = 0$ for $f=0$. These two relations differ only by the substitution of E_f for E_m/b_2 . A similar correspondence is also obtained for the unloading and reloading equations and

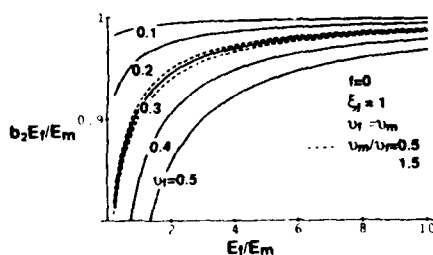


Fig. 11. Variation of $E_f/(E_m b_2)$ at $f=0$ with other matrix and fiber properties.

for residual stresses of opposite sign. The ratio $E_f/(E_m/b_2)$ with $f=0$ is shown in Fig. 11 for various values of E_f/E_m , ν_f/ν_m , and ν_f (b_2 is independent of λ). For values of these parameters typical of ceramic and intermetallic composites ($E_f/E_m > 2$ with ν_f and $\nu_m < 0.3$), this ratio differs from unity by less than 5%. Therefore the analysis of Ref. [6] is a close approximation to the constant τ analysis for single fiber experiments in such materials.

5. RELATIONS BETWEEN CRACK OPENING DISPLACEMENTS AND SINGLE AND MULTIPLE FIBER DISPLACEMENTS

Crack bridging laws can be deduced directly from single fiber pushing or pulling experiments. Two steps are involved; one is to relate the crack opening used in continuum bridging models to the displacements measured in multiple fiber experiments [equation (8b)] and the other is to relate the displacements measured in single and multiple fiber experiments by evaluating these displacements under appropriate boundary conditions. For multiple fiber measurements, Type II boundary conditions are used to evaluate the b parameters in equation (3). For single fiber measurements, several test configurations are possible. If a single fiber within a composite is tested, the b parameters are evaluated using $f=0$ (for which Type I and II boundary conditions are the same), whereas the a parameters of equation (2) are evaluated using the actual value of f for the composite. However, there is some uncertainty in the choice of matrix elastic properties for the evaluation of the b 's in this case, since in the near field there is all matrix, whereas in the far field the average composite properties would be more appropriate. Since strain gradients are highest in the near-field region, the matrix properties E_m and ν_m are used in the following calculations. For a model test specimen comprising a single fiber in a cylinder of matrix, a single value of f would be used for evaluation of all parameters, but this value may differ from that in a composite.

The displacements measured in single and multiple fiber experiments and the crack opening displacements can differ substantially. As an illustration, stress-displacement relations are plotted in Fig. 12 using the following properties typical of intermetallic composites [7]: $f=0.36$, $E_f/E_m=5.1$, $\lambda=1$, $E_f=E_c$, and $\nu_f=\nu_c=\nu_m=0.3$ (other relevant parameters calculated from these properties are listed in Table 1). The parameter S_{R0} depends on the ratio of the peak applied stress, σ_p , to the residual axial stress, σ_{i0}^* , in the fibers; for this example, the value $\sigma_p/\sigma_{i0}^*=3.0$ was chosen, as this corresponds to an experiment reported in Ref. [7]. The displacement scaling parameters δ^* and δ' for the Coulomb and constant friction models are defined in equations (11d) and (21); the values of the terms in square brackets in these equations

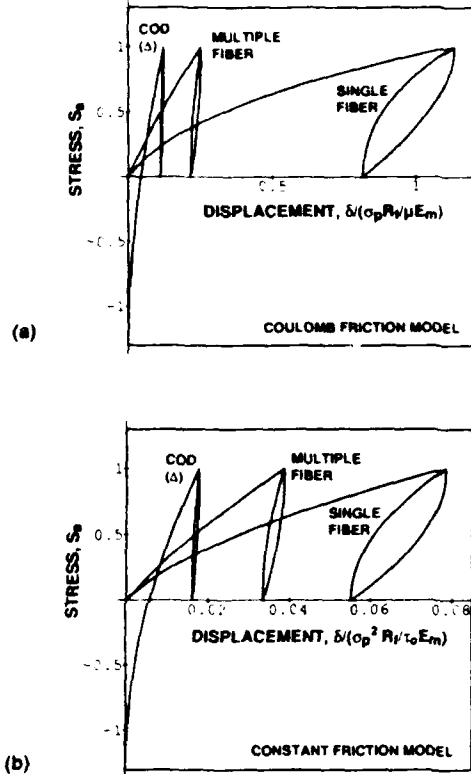


Fig. 12 Comparison of stress displacement relations for crack bridging (COD) and for single and multiple fiber pulling experiments for a composite with properties given in Table 1.

are listed in Table 1. The displacements for single and multiple fiber pulling are plotted in Fig. 12 in the form $\delta / [(\sigma_p R_f) / (\mu E_m)]$ for the Coulomb friction model and $\delta / [(\sigma_p^2 R_f) / (\tau_0 E_m)]$ for the constant friction model. The crack opening displacements are expressed in terms of Δ , given for this composite by $\Delta = 0.31\delta$ [equation (8b)]. The curves for single and multiple

Table 1 Composite properties used for Fig. 12

	Single fiber pull	Multiple fiber pull
E_f/E_m	5.1	
$\nu_f = \nu_m = \nu$	0.3	
f	0.36	
λ	1	
$A = \left(1 - \frac{a_1 b_1}{a_4}\right)^{-1}$	1.14	0.768
b_1		0.31
$b_2 + b_3$		0.31
$\frac{(b_2 + b_3)(1 + a_1 f)}{2b_1}$	2.33	-0.855
$(1 + b_3)(1 - a_1 f)^2/4$	0.047	0.011
$S_{R0} = \frac{\sigma_{f0} \sigma_f}{(A - 1)(1 - a_1 f)}$	2.36*	-5.6*

*These values correspond to $\sigma_f/\sigma_{f0} = 3.0$, corresponding the experiment in Ref. [7] with initial axial residual stress $\sigma_{f0} = 800$ MPa and peak stress $\sigma_f = 2.4$ GPa.

fiber pulling hold for $F < 0$, whereas the crack opening displacement curves apply only for $G_c = 0$ (i.e. $F = -S_{R0}$). For other values of F , the curves shift along the displacement axes, as discussed in Sections 3 and 4. For given applied stress, the displacements in single fiber pulling are larger than in multiple fiber pulling. Moreover, the fraction of the initial displacement that is recovered during unloading is larger for single, than for multiple fibers.

The negative crack bridging stresses at small displacements in Fig. 12 represent crack-opening pressure, and reflect the fact that compressive applied load would be needed to keep a matrix crack fully closed in this composite [31] (because of residual tensile stress in the matrix). The displacements in this region correspond to the spontaneous debonding and sliding discussed with reference to fiber pulling experiments in Section 3.

6. DISPLACEMENTS DURING FIBER PUSHING EXPERIMENTS

The axial fiber stresses during initial monotonic compressive loading are shown schematically in Fig. 13(a). In this case, the direction of sliding over the debonded interface and the sign of the stress jump

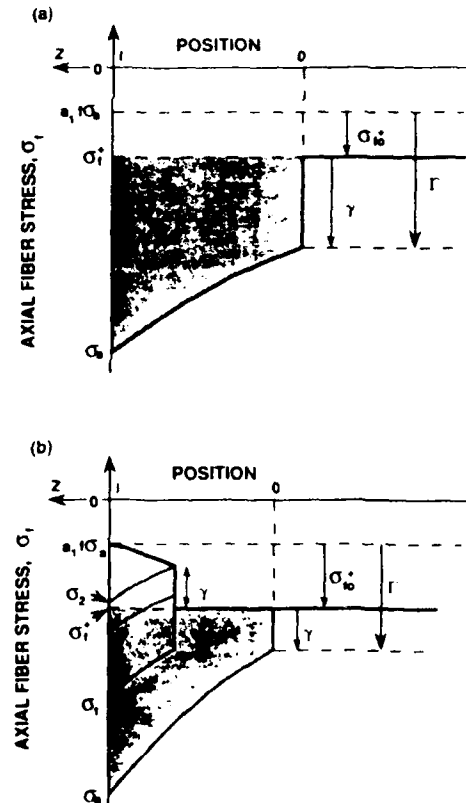


Fig. 13. Axial stresses in fiber during initial loading in fiber pushing test: (a) no spontaneous debonding; (b) with spontaneous debonding.

at the debond tip are reversed. With the change in sliding direction, the frictional stress, τ , becomes positive, a change which may be accomplished by defining the friction coefficient, μ , in equation (1) to be negative. The change in sign of the stress jump causes γ to become negative, and equation (4) to be redefined as

$$\gamma \equiv \sigma_f' - \sigma_f'' = \frac{-(1-f)}{f c_1 c_2} \left(\frac{E_m G_c}{R} \right)^{1/2} \quad (31)$$

The equations of Sections 3 and 4 are unaltered provided spontaneous debonding does not occur, although σ_a is negative, leading to changes in sign of many of the other parameters, and negative displacements. In addition, with the sign change in the relation between γ and the debond energy, G_c , the parameters Γ and Γ' , which are dependent on γ , take different values in fiber pushing experiments; in pulling experiments, Γ is equal to the difference between the magnitudes of γ and the residual axial fiber stress, σ_{f0} , [equation (11c)], whereas in pushing experiments, Γ is negative, with magnitude equal to the sum of the magnitudes of γ and σ_{f0} .

If spontaneous debonding occurs, the axial fiber stresses during initial loading are altered as shown in Fig. 13(b). For applied loads larger in magnitude than σ_1 in Fig. 13(b), the changes in displacement are still given by the expressions in Sections 3 and 4. However, for smaller applied loads the displacements are altered. For applied loads smaller than σ_2 in Fig. 13(b) the displacements are given by the expressions for reloading after unloading [the second term of equation (18) for Coulomb friction and equation (28) for constant friction], whereas for loads in the range σ_1 to σ_2 the displacements are equivalent to those occurring between σ_1 and σ_2 in Fig. A2(b) [equation (A16) with σ_p replaced by σ_1].

7. THE ONSET OF COMPLETE SLIDING IN A THIN SLICE OF COMPOSITE

Calculation of the load needed to cause complete sliding of a fiber within a specimen of finite thickness would require analysis of the interaction of the stress field ahead of the debond crack with the back surface of the specimen, as the debond approaches the back surface. Moreover, the boundary condition depicted in Fig. 1 far ahead of the debond tip must be disturbed in order to allow the back surface to be stress-free. The true boundary condition would become sensitive to details of the gripping arrangement. Nevertheless, some qualitative insight into the problem of the onset of complete sliding (and most likely on upper bound for the critical load) may be obtained by ignoring these effects and setting the debond length in the present analysis [equation (10)] equal to the specimen thickness.

In general, the critical loads needed to cause complete sliding in pulling and pushing experiments would be expected to differ. If we assume that the

effect of the back surface on the debond crack as it approaches the surface is similar in both experiments (i.e. that the debond breaks through when it approaches a critical distance from the surface [23]) and that the gripping arrangements are the same, the analysis of the previous sections can be used to compare the critical loads in pulling and pushing, by evaluating σ_a for both cases at a fixed value of l (without having to specify l). For the Coulomb friction model, this is done by evaluating equation (10) for pushing and pulling, using the results noted in Section 6. The axial stresses in the fiber are shown schematically in Fig. 14. Two effects contribute to the applied stresses in pulling, σ_a' , and pushing, σ_a'' , being different; one is the opposite signs of Poisson's strains in the two experiments, which causes the magnitude of $\Delta\sigma_a$ to be larger in pushing (for b_1 positive), and the other is the offset along the stress axis due to the fact that $\Delta\sigma_a$ is measured relative to the residual axial stress in the fiber (σ_{f0}). For the constant friction model, only the latter effect contributes. In this case, the applied stresses at a given slip length are related by

$$|\sigma_a''| - |\sigma_a'| = 2|\sigma_{f0}| \quad (32)$$

When the debonds reach the ends of the fibers in the cases depicted in Fig. 14(a) (i.e.) with $\Gamma' > 0$, the

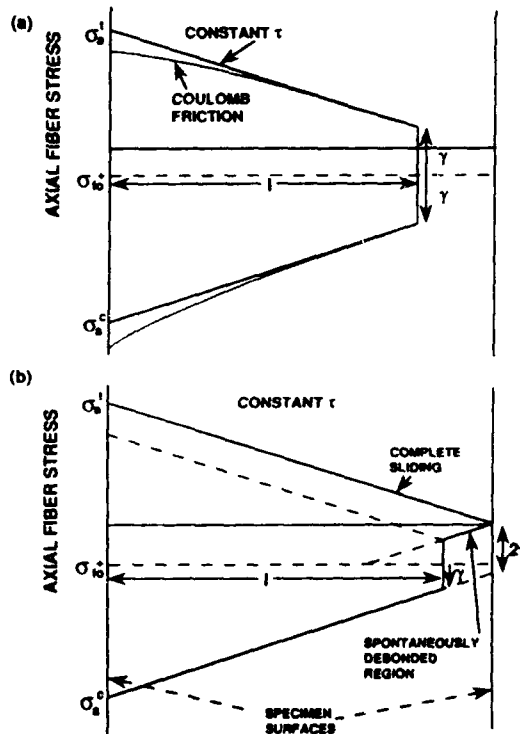


Fig. 14. (a) Comparisons of axial fiber stresses in pushing and pulling experiments for given debond length. (b) Axial fiber stresses for constant friction model with $|\gamma| < |\sigma_{f0}|$ as debond approaches back surface of a specimen of finite thickness.

applied loads for both pulling and pushing are larger than those which can be supported by frictional resistance, so that sudden load drops occur. Therefore, the peak loads are related by equation (32).

A different response is expected if $\Gamma' < 0$. In this case, spontaneous debonding occurs at the back surface before the push or pull test begins [Fig. 14(b)]. When the debond that is driven by pushing the fiber approaches the spontaneously debonded region near the back surface, a sudden load drop again occurs. However, when the debond that is driven by pulling the fiber reaches the same location, the applied load is smaller than that needed to cause complete sliding. The load must be further increased to reverse the direction of sliding over the spontaneously debonded region, as indicated in Fig. 14(b). Therefore, a sudden load drop does not occur. In this case, the peak loads in the pushing and pulling experiments are related by

$$|\sigma_s^+| - |\sigma_s^-| \approx 2|\gamma| \quad (\Gamma' < 0). \quad (33)$$

It is emphasized that these relations are approximate and may be strongly affected by different gripping arrangements in pulling and pushing tests.

Acknowledgements—This work was supported by Rockwell International Independent Research and Development Funds and by the U.S. Air Force under Contract No. F33615-90-C-5928. The author is grateful to Dr. B. N. Cox and Professor J. W. Hutchinson for helpful discussions.

REFERENCES

1. D. B. Marshall, *J. Am. Ceram. Soc.* **67**, C259 (1984).
2. D. B. Marshall and W. C. Oliver, *J. Am. Ceram. Soc.* **70**, 542 (1987).
3. T. P. Weihs and W. D. Nix, *Scripta metall.* **22**, 271 (1988).
4. T. P. Weihs and W. D. Nix, *J. Am. Ceram. Soc.* **74**, 524 (1991).
5. T. P. Weihs, C. M. Dick and W. D. Nix, in *MRS Symp. Proc.* **120** (edited by E. D. Lemkey, S. G. Fishman, A. G. Evans and J. R. Striffe) (1988).
6. D. B. Marshall and W. C. Oliver, *J. Mater. Sci. Engng A126*, 95 (1990).
7. D. B. Marshall, M. C. Shaw and W. L. Morris, *Acta metall. mater.* **40**, 443 (1992).
8. J. D. Bright, D. K. Shetty, C. W. Griffin and S. Y. Limaye, *J. Am. Ceram. Soc.* **72**, 1891 (1989).
9. P. D. Jero and R. J. Kerans, *Scripta metall.* **24**, 2315 (1990).
10. M. K. Brun and R. N. Singh, *Adv. Ceram. Mater.* **3**, 506 (1988).
11. J. W. Laughner and R. T. Bhatt, *J. Am. Ceram. Soc.* **72**, 2017 (1989).
12. G. Morsher, P. Pirouz and A. H. Heuer, *J. Am. Ceram. Soc.* **73**, 713 (1990).
13. R. J. Kerans, R. S. Hay, N. J. Pagano and T. A. Parthasarathy, *Am. Ceram. Bull.* **68**, 429 (1989).
14. J. I. Eldridge and P. K. Brindley, *J. Mater. Sci. Lett.* **8**, 1451 (1989).
15. C. J. Yang, S. M. Jeng and J.-M. Yang, *Scripta metall.* **24**, 469 (1990).
16. K. Kendall, *J. Mater. Sci.* **10**, 1011 (1975).
17. E. P. Butler, E. R. Fuller Jr and H. Chan, *MRS Symp. Proc. Tailored Interfaces in Composites Materials*, V 170 (1990).
18. E. P. Butler, E. R. Fuller Jr, T. R. Palamides and H. M. Chan, *Proc. Int. Symp. on Advances in Processing of Ceramic and Metal Matrix Composites* (edited by H. Mostaghacci) Pergamon Press, Oxford (1990).
19. Y.-C. Gao, Y.-M. Mai and B. Cottrill, *J. appl. Math. Phys.* **39**, 550 (1988).
20. D. K. Shetty, *J. Am. Ceram. Soc.* **71**, C107 (1988).
21. J. W. Hutchinson and H. M. Jensen, *Mech. Mater.* **9**, 139 (1990).
22. B. N. Cox, *Acta metall. mater.* **38**, 2411 (1990).
23. R. J. Kerans and T. A. Parthasarathy, *J. Am. Ceram. Soc.* **74**, 1585 (1991).
24. L. B. Freund, *Eur. J. Mech.* In press.
25. L. S. Sigl and A. G. Evans, *Mech. Mater.* **8**, 1 (1989).
26. L. N. McCartney, *Proc. R. Soc. A425*, 215 (1989).
27. E. R. Fuller Jr, E. P. Butler and W. C. Carter, in *Proc. Nato Advanced Research Workshop on Toughening Mechanisms in Quasi Brittle Materials*, Northwestern University (1990).
28. L. N. McCartney, *Proc. R. Soc. A409*, 329 (1987).
29. B. Budiansky and J. C. Amazigo, *J. Mech. Phys. Solids* **37**, 93 (1989).
30. D. B. Marshall and B. N. Cox, *Mech. Mater.* **7**, 127 (1988).
31. D. B. Marshall and A. G. Evans, *Materials Forum* **11**, 304 (1988).

APPENDIX A

Initial Loading

The axial fiber stresses during initial monotonic loading are obtained by integration of equation (6), with τ given by equations (1), (2b) and (3b), and the condition $\sigma_r = \sigma_s^-$ at $z = 0$. The result can be expressed as

$$\Delta\sigma_r = \gamma - \alpha(1 - e^{-\eta z}) \quad (A1)$$

where

$$\eta = 2\mu b_1/R_1 \quad (A2)$$

$$\alpha = \sigma_s^-/b_1 \quad (A3)$$

and γ is defined in equation (4). Equation (A1) is equivalent to equation (44) of Ref. [21]. The length, l , over which debonding and sliding occur is given by setting $\sigma_r = \sigma_s$ at $z = l$

$$\eta l = -\ln \left[\frac{\sigma_s - \sigma_s^- + \alpha - \gamma}{\alpha} \right] \quad (A4)$$

The displacement δ , obtained from equations (7), (A1) and (A4) is

$$\delta = \frac{b_2 + b_3}{\eta E_m} \left[(\alpha - \gamma) \ln \left(\frac{\sigma_s - \sigma_s^- + \alpha - \gamma}{\alpha} \right) + \gamma - (\sigma_s - \sigma_s^-) \right] \quad (A5)$$

which can be shown to be equivalent to equations (47) and (49) in Ref. [21].

It is convenient at this stage to expand the terms within the square bracket of equation (A5) and regroup them into parameters that characterize the applied loading, the residual stresses, and the debond energy. After some manipulation with equations (2)-(4) and (A3), these terms can be expressed as

$$\alpha - \gamma = \left(\frac{a_3 f}{b_1} \right) \sigma_s + A \sigma_{R0} \quad (A6a)$$

$$\alpha - \gamma - \sigma_s^- + \sigma_s = \left(1 - a_1 f + \frac{a_3 f}{b_1} \right) \sigma_s + \sigma_{R0} \quad (A6b)$$

$$\gamma - (\sigma_s - \sigma_s^-) = -(1 - a_1 f) \sigma_s + \Gamma \quad (A6c)$$

$$\alpha = \left(\frac{a_3 f}{b_1} \right) \sigma_s + \sigma_{R0} + \Gamma \quad (A6d)$$

where the parameters A , σ_{R0} , Γ , and σ_{f0}^* are defined in equation 11(c) to (g) of the text. With these relations, equation (A5) becomes

$$\delta = \frac{b_2 + b_3}{\eta E_m} \left\{ \left(\left(\frac{a_3 f}{b_1} \right) \sigma_s + A \sigma_{R0} \right) \times \ln \left[\frac{\left(1 - a_1 f + \frac{a_1 f}{b_1} \right) \sigma_s + \sigma_{R0}}{\left(\frac{a_1 f}{b_1} \right) \sigma_s + \Gamma + \sigma_{R0}} \right] - (1 - a_1 f) \sigma_s + \Gamma \right\} \quad (A7)$$

Further simplification of equation (A7), for $(a_1 f/b_1) = 0$, can be achieved by normalizing the parameters by the peak value of applied stress, σ_p , to give equation (9) in the text. Similarly, equation (10) of the text follows from equation (A4).

Unload Reload

Using the same procedure as for the initial loading, $\Delta\sigma_f$ during unloading can be evaluated as

$$\Delta\sigma_f = -(\alpha - \gamma) + (\alpha - \gamma + \sigma_s - \sigma_f^*) e^{-\alpha(z-l)} \quad (A8)$$

where l_p is given by equation (A4) at $\sigma_s = \sigma_p$. The reverse slip length, s , is obtained by setting $\Delta\sigma_f$ equal to $\Delta\sigma_{fp}$ at $z = l - s$

$$2\eta s = \ln \left[\frac{\alpha - \gamma + \sigma_s - \sigma_f^*}{\alpha - \gamma + \sigma_p - \sigma_{fp}^*} \right] \quad (A9)$$

Equation (A9) requires that α be independent of σ_s . With some manipulation of equations (A6), (11f) and (11c), this condition becomes $(a_2 a_3 f/a_4) \ll 1$. This parameter is zero for either $f = 0$ or $v_f = v_m$, and is very small for all other likely composite properties; $(a_2 a_3 f/a_4) < 0.06$ for all values of E_m/E_f and ξ_f with $0.5 < (v_m/v_f) < 1.5$, $v_f < 0.5$, $f < 0.5$, and $\lambda < 2$. Therefore, since the exact expression for s with nonzero values of $(a_2 a_3 f/a_4)$ is very lengthy, it is not pursued here. The displacement evaluated from equations (A5), (A8), and (A9) in terms of the normalized parameters defined previously is given in equation (16) of the text.

The fiber stress $\Delta\sigma_f$ during reloading can be evaluated as

$$\Delta\sigma_f = -(\alpha - \gamma) + (\alpha - \gamma + \sigma_s - \sigma_f^*) e^{-\alpha(z-l)} \quad (A10)$$

The new slip length, t , is obtained by setting $\Delta\sigma_f$ equal to $\Delta\sigma_{f0}$ at $z = l - t$

$$2\eta t = \ln \left[\frac{\alpha - \gamma + \sigma_{f0}^*}{\alpha - \gamma + \sigma_s - \sigma_f^*} \right] \quad (A11)$$

As with the corresponding expression for unloading, this expression requires $(a_2 a_3 f/a_4) \ll 1$. The displacement evaluated from equations (17), (A10) and (A11), expressed relative to the peak load displacement and in terms of the normalized parameters defined previously, is given in equation (18) of the text.

Unload/Reload Relations for Small Loads

If the peak stress during the initial loading is smaller than a critical value, reverse slip during unloading can reach the end of the debonded region before unloading is complete. The condition to avoid this is $s < l$ at complete unload, with l given by equation (A4) at $\sigma_s = \sigma_p$, and s given by equation (A9) at $\sigma_s = 0$. In terms of the normalized parameters

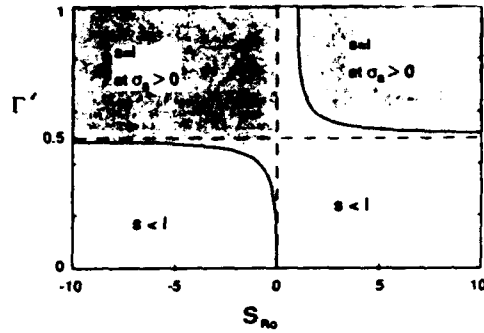


Fig. A1. Condition for region of reverse slip (length, s) to reach end of initial debond (length, l) before complete unloading. Coulomb friction model.

defined in equations (11) this condition can be written as

$$\Gamma'^2 - 2S_{R0}\Gamma' + S_{R0} > 0 \quad (A12)$$

Equation (A12) is plotted in Fig. A1. For $|S_{R0}| \geq 2$, the condition $s < l$ is satisfied for $\Gamma' \leq 0.5$.

For larger values of Γ' the axial fiber stresses at several stages of unloading are shown schematically in Fig. A2(a). For the first part of the unloading (i.e. for $\sigma_s < \sigma_s < \sigma_p$), s is smaller than l_p , so the displacements are given by

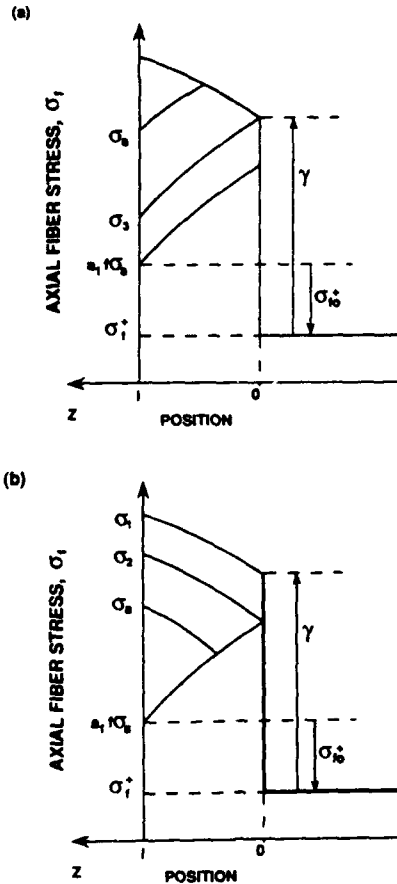


Fig. A2. Axial fiber stresses at several stages during unloading (a) and reloading (b) under conditions where reverse slip reaches the end of the initial debond before unloading is complete.

equation (16). The stress, σ_1 , at which $s = l_p$ is given by equations (A4) and (A9), with $\sigma_s = \sigma_p$ in equation (A4) and $\sigma_s = \sigma_1$ in equation (A9). In terms of the normalized parameters, the result is

$$S_1 = S_{R0} - (S_{R0} - \Gamma')^2 / (S_{R0} - 1). \quad (A13)$$

For continued unloading below S_1 , the sliding distance is fixed at $s = l_p$, and the lower limit of integration for equation (15) becomes zero. The displacement in this load range becomes

$$\frac{\delta_p - \delta}{\delta^*} = \frac{(1 - \Gamma')(\Gamma' - S_s)}{(S_{R0} - \Gamma')} \quad (S_s < S_1). \quad (A14)$$

The axial stresses during reloading are shown schematically in Fig. A2(b). For $\sigma_s < \sigma_2$ the displacements are given by equation (18), but with $(\delta_p - \delta_0)/\delta^*$ given by equation (A14) at $S_s = 0$. The stress, σ_2 , at which the new slip length, l , equals l_p is given by equations (A4) and (A11)

$$S_2 = S_{R0} - (S_{R0} - 1)^2 S_{R0} / (S_{R0} - \Gamma')^2. \quad (A15)$$

For $\sigma_s > \sigma_2$, the slip length is fixed at $l = l_p$ and the lower limit of integration for equation (17) becomes zero. In this case the displacement becomes

$$\frac{\delta - \delta_0}{\delta^*} = (1 - \Gamma') \left[\frac{S_{R0}}{S_{R0} - \Gamma'} - \left(\frac{S_{R0} - S_s}{S_{R0} - 1} \right) \right] \quad (S_s > S_2). \quad (A16)$$

APPENDIX B

Nomenclature

a_i, b_i = dimensionless functions of elastic properties, f , and λ defined in Ref. [21]

$$A = \left[1 - \frac{a_i b_i}{a_s} \right]^{-1}$$

E = Young's modulus

f = volume fraction of fibers

G_C = Mode II fracture energy at debond tip

R_f = fiber radius

ν = Poisson's ratio

$\xi_f = (1 - \nu_f)E_f/(1 - \nu_f)E$

ϵ^T = misfit strain

$\lambda = \epsilon^T/\epsilon^T$, anisotropy of misfit strain

σ_s = stress applied to end of fiber

σ_f = axial stress in fiber

δ, Δ = displacements [equations (7) and (8)]

l = debond length

τ = frictional stress

μ = coefficient of friction

γ = normalized debond energy [equation (4)]

S_s = normalized applied stress, σ_s/σ_p

S_{R0} = normalized residual stress [equation (11b)]

Γ = normalized debond energy [equation (11c)]

δ^*, δ' = normalizing parameters for displacement [equations (11d) and (21)]

σ_{R0} = residual stress parameter [equation (11f)]

σ_{f0}^* = residual axial stress in fiber [equation (11g)]

Subscripts

r = radial

f = fiber, axial

m = matrix, axial

p = peak load

o = unload

Superscripts

$+$ = position well ahead of debond

$-$ = position just behind debond tip